Study of ultra-compact Compton camera based on 3-D position sensitive scintillator for environmental and medical gamma-ray imaging

February 2017

Aya KISHIMOTO

Study of ultra-compact Compton camera based on 3-D position sensitive scintillator for environmental and medical gamma-ray imaging

Waseda University
Graduate School of Advanced Science and Engineering
Department of Pure and Applied Physics
Research on radiological physics and technology

Aya KISHIMOTO

February 2017

Abstract

Recently, the demand for visualizing radiation distribution has been growing in various fields. A Compton camera, which is one of the gamma-ray imaging device, features large energy range from a few hundreds keV to several MeV. In this study, we have developed two types of Compton camera aiming at applications for environmental measurement and nuclear medicine.

Since the nuclear disaster in Fukushima Daiichi nuclear power plant, the radiation hotspots in environment have been a serious problem. In order to obtain the radiation distribution in wide-area effectively, we developed the handheld Compton camera for environmental gamma-ray measurement. The camera consists of Ce-doped $Gd_3Al_2Ga_3O_{12}$ (Ce:GAGG) scintillator and multi-pixel photon counter (MPPC) arrays and features high sensitivity even for high energy gamma ray such as 662 keV from ^{137}Cs. By utilizing newly developed depth of interaction (DOI) identification technique in the scintillator block, we successfully improved the angular resolution. The angular resolution and the intrinsic efficiency of the handheld Compton camera for 662 keV were around 8° (FWHM) and 0.43%, respectively. Through several imaging tests using point sources, we evaluated the imaging capability of the camera for not only ^{137}Cs source but various other gamma-ray emitting sources. Based on these results, we have conducted field tests in Namie, Fukushima with the handheld Compton camera. As a result, we have confirmed that the camera can localize hotspots in a short time typically within 10 min.

On the other hand, we also applied a Compton camera to the field of molecular imaging in nuclear medicine. The purpose of the development is to replace current modalities such as SPECT and PET by extending energy range over 1 MeV, which may realize more precise diagnostic imaging with reduced costs in the near feature. For this purpose, we have also developed the medical Compton camera which focuses on improvement of the angular and spatial resolutions. One of the key feature of the medical Compton camera was its compactness of $5 \times 6 \times 11\,\mathrm{cm}^3$, which enables flexible measurement depending on demand for various situations. The typical angular resolution and intrinsic efficiency of the medical Compton camera for 662 keV gamma rays were 4.2° (FWHM), that is equal to the spatial resolution of around 3 mm at a distance of 4 cm from the detector, and 0.06%, respectively. In this study, the 3-D image reconstruction method based on maximum likelihood expectation maximization (MLEM) algorithm was also developed. By adopting multi-angle data acquisition method, we showed that imaging performance of the camera is significantly improved, such that angular resolution and sensitivity becomes 3-dimensionally uniform over the region of interest (ROI). By using the medical Compton

camera, various 3-D imaging tests were conducted. In the uniform plane source imaging of ^{137}Cs under the data-acquisition condition of 12-angles, the configuration of the square source was reconstructed 3-dimensionally and the uniformity of the reconstructed image became around $\pm 10\%$. Moreover, by using multiple energy and extended gamma-ray sources, we confirmed the capability of 3-D imaging both through the experiment and simulation for quantitative evaluation. Finally, as pre-clinical evaluation the first imaging test with a living mouse by the medical Compton camera using multiple tracers was conducted. The three different tracers of ^{131}I (364 keV), ^{85}Sr (514 keV), and ^{65}Zn (1116 keV) were injected into an 8-weeks-old mouse and the data was taken from 12-angles. With the total integration time of 2 hours, we confirmed that each tracer was accumulated correctly as expected on the target organs, such as thyroid (^{131}I), bone (^{85}Sr), and liver (^{65}Zn) based on 3-D image. The result indicates the achievement of 3-D multi-color imaging and the feasibility of newly in vivo imaging by Compton camera.

Contents

1 Introduction **9**

2 Radiology Imaging **12**

2.1 Environmental imaging 12

2.1.1 Mechanical collimation method 12

2.1.2 Compton camera in environmental measurement 15

2.2 Medical imaging 17

2.2.1 Single photon emission computed tomography (SPECT) 18

2.2.2 Position emission tomography (PET) 18

2.2.3 Compton camera in medical field 20

3 Principle of Compton camera **23**

3.1 Basic physics 23

3.1.1 Interaction of photons in materials 23

3.1.2 Compton kinematics 24

3.2 Factors governing Compton Camera performance 26

3.2.1 Angular resolution 27

3.2.2 Detection efficiency 35

3.3 Hit patterns of gamma ray in Compton camera 36

3.4 Image reconstruction 37

3.4.1 Simple back projection (SBP) 37

3.4.2 Maximum Likelihood Expectation Maximization (MLEM) 37

4 Compton camera for environmental measurement **41**

4.1 Introduction 41

4.2 Materials 41

4.2.1 Scintillator 41

4.2.2 Multi-pixel photon counter (MPPC) 42

4.3 Depth of interaction (DOI) 43

4.3.1 non-DOI Compton camera 43

4.3.2 DOI technique for the handheld Compton camera 44
4.4 Geometric configuration 46
4.5 Readout system 47
4.6 Data analysis for event selection 49
4.7 Simulator of the DOI Compton camera 50
4.8 Image reconstruction 53
4.8.1 Image projection methods 53
4.8.2 MLEM algorithm for the DOI Compton camera 53
4.9 Detector performance 54
4.9.1 Position response of the scintillator 54
4.9.2 Energy response 58
4.9.3 Signal to noise ratio 58
4.9.4 Counting rate performance 60
4.9.5 Angular resolution for various directions 62
4.9.6 Detection efficiency 65
4.10 Imaging performance 65
4.11 Field tests in Fukushima 67
4.12 Discussion 67
4.13 Chapter summary 72

5 Three-dimensional image reconstruction 74
5.1 Extending MLEM algorithm to 3-D imaging 74
5.2 Data acquisition method 76
5.3 Imaging performance 78
5.3.1 Simulation 78
5.3.2 Experiment 84

6 Compton camera for medical imaging 87
6.1 Introduction 87
6.2 Development of medical Compton camera 88
6.2.1 Study for improving the angular resolution 88
6.2.2 Design of medical Compton camera 88
6.3 Detector performance 91
6.3.1 Position response of the scintillator 91
6.3.2 Energy response 91
6.3.3 Evaluation of image resolution 97
6.3.4 Detection efficiency 97
6.4 Optimization of image reconstruction for the medical Compton camera . . . 102
6.4.1 Dependence on the number of data acquisition angle 102

6.4.2 Positional dependence of spatial resolution and intensity in 12-angles data acquisition . . . 105
6.4.3 Uniformity for multi-energy imaging . . . 109
6.5 Imaging performance . . . 109
6.5.1 Double source imaging . . . 109
6.5.2 Imaging of uniform line source . . . 110
6.5.3 Imaging of a uniform plane source . . . 113
6.5.4 Multi-color imaging . . . 115
6.5.5 Quantitative estimation for multi-color imaging . . . 121
6.6 Small-animal imaging . . . 126
6.7 Discussion . . . 132

7 Conclusion **134**

A Energy and temperature calibration **136**

B Position calibration **138**

List of Figures

1.1 Outlook of the COMPTEL onboard Compton Gamma-ray Observatory . . 10
1.2 Sensitivities of the hard-X and Gamma-ray detectors 10

2.1 Dose rates map around the Fukushima Daiichi Nuclear Plant 14
2.2 Schematic view of collimators 15
2.3 Photograph and field performance of ASTROCAM 17
2.4 Schematic diagram of PET 19
2.5 Spatial resolution across SPECT and PET 20
2.6 Multi-color mouse imaging using GREI 21

3.1 Dominant interaction process of photons 24
3.2 Diagram of Compton scattering 25
3.3 The angular distribution of Compton scattering 25
3.4 Basic concept of Compton camera 26
3.5 Relationship between Compton scattering angle θ and E_1 27
3.6 Parameter definition in calculating position uncertainty 28
3.7 Contribution of the geometrical uncertainty 30
3.8 Contribution of the energy uncertainty 32
3.9 Doppler broadening effects as a function of proton number 33
3.10 Doppler broadening effect in GAGG scintillator for 200 keV and 662 keV gamma rays 34
3.11 Contribution of the Doppler broadening effect in GAGG 35
3.12 Hit patterns in Compton camera 36
3.13 MLEM reconstruction images 39
3.14 Intensity of reconstructed image 40

4.1 Photograph of 8×8 MPPC array 43
4.2 Resistive charge division network 44
4.3 Schematic view of of the DOI method 46
4.4 Photographs of the DOI Compton camera. 47
4.5 Photograph of Ce:GAGG array 48

4.6 Read-out diagram of the DOI Compton camera 49
4.7 Flow chart of event selection 51
4.8 2-D energy spectrum 52
4.9 Scintillator configuration in Geant4 simulation 52
4.10 Equisolid angle and stereographic projection image 54
4.11 The position response of the scintillators in the scatterer 55
4.12 The position response of the scintillators in the absorber 56
4.13 The number of hit events by each layer 57
4.14 1-D energy spectra of the scatterer 58
4.15 ARM distribution w/ and w/o back-scatter events 60
4.16 Hit pattern of multiple-scattering event 61
4.17 ARM distribution w/ and w/o multiple-scattering events 61
4.18 Counting rate performance 63
4.19 Comparison of ARM between DOI and non-DOI Compton cameras 64
4.20 Intrinsic efficiency of the DOI Compton camera 65
4.21 Experimental MLEM imaging results of a point source 67
4.22 Experimental MLEM imaging results of two point sources 68
4.23 Source configuration 69
4.24 Energy spectra of multiple source measurement 69
4.25 Multiple sources image 70
4.26 Examples of gamma-ray images and energy spectrum taken in field test in Fukushima 71

5.1 Diagram of the 3-D MLEM reconstruction 75
5.2 Schematic geometry of sensitivity map 76
5.3 3-D sensitivity map of the handheld Compton camera 77
5.4 Configuration of the single-angle data acquisition 77
5.5 Configuration of the multi-angle data acquisition 78
5.6 3-D MLEM imaging result of the simulated single-angle measurement . . . 79
5.7 1-D profiles of single-angle MLEM imaging on simulation 79
5.8 3-D MLEM imaging result of the simulated multi-angle measurement 80
5.9 1-D profiles of multi-angle MLEM imaging on simulation 80
5.10 MLEM imaging result of the pattern 1 82
5.11 MLEM imaging result of the pattern 2 83
5.12 MLEM imaging result of the pattern 3 83
5.13 3-D MLEM imaging result of the experimental single-angle measurement . . 84
5.14 1-D profiles of single-angle MLEM imaging 84
5.15 3-D MLEM imaging result of the experimental multi-angle measurement . . 85
5.16 1-D profiles of multi-angle MLEM imaging 85

6.1 Angular resolution of the DOI and the medical Compton camera 89
6.2 Configuration of the medical Compton camera on Geant4 90
6.3 Detector configuration of the medical Compton camera 91
6.4 The position response of the scintillators in the scatterer 92
6.5 The position response of the scintillators in the absorber 93
6.6 Energy spectra of the medical Compton camera 95
6.7 Temperature dependence of energy resolution 96
6.8 Optimization of the energy range E_1 96
6.9 ARM distribution of the medical Compton camera 98
6.10 The evaluation of the spatial resolution using a ^{137}Cs point source 99
6.11 Distance dependence of angular resolution 100
6.12 Energy dependence of angular resolution 100
6.13 Distance dependence of detection efficiency 101
6.14 Energy dependence of detection efficiency 101
6.15 Comparison of the number of data acquisition angle 103
6.16 Spatial resolutions as a function of number of data acquisition angle 104
6.17 Imaging results of ^{137}Cs diffuse source 105
6.18 NMSE value as a function of number of data acquisition angle 106
6.19 Spatial resolution as a function of the number of iteration 107
6.20 Schematic geometry to evaluate positional dependence 107
6.21 Spatial resolution and relative intensity as a function of the position 108
6.22 MLEM imaging result of the double ^{137}Cs sources measurement 110
6.23 Schematic view of geometry of the line source measurement 111
6.24 MLEM imaging results of the ^{137}Cs line source 112
6.25 The spatial resolution of line source as a function of the distance 113
6.26 Geometries of plane source imaging 115
6.27 2-D slices of the plane source image as measured in the pattern-1 116
6.28 Imaging results in the pattern-1 117
6.29 2-D slices of the plane source image as measured in the pattern-2 118
6.30 2-D imaging results in the pattern-2 119
6.31 Uniformity and spatial resolution as a function of iteration number 120
6.32 Photograph of syringe phantoms 122
6.33 Energy spectrum of multi-color gamma-ray measurement 122
6.34 MLEM imaging results of multi-color measurement 123
6.35 X profile of the multi-color phantom imaging result 123
6.36 Comparison of MLEM images on various event statistics 124
6.37 Comparing the event number used for image reconstruction 126
6.38 Comparing intensity of reconstructed image 127

6.39 Images reconstructed by escape events 128
6.40 Experimental evaluation of the number of event and the intensity 129
6.41 Energy spectrum for a mouse imaging 129
6.42 Results of 2D slice of mouse imaging 130
6.43 2-D montage of the mouse image 131

A.1 Temperature coefficient of MPPC arrays 137

B.1 2-D position map 139

List of Tables

2.1 Isotopes released from Fukushima Daiichi nuclear power plant 13
2.2 Typical SPECT radioisotopes 18

4.1 Characteristic of Ce:GAGG and other scintillators 42
4.2 Scintillator configuration of the non-DOI Compton camera 45
4.3 Scintillator configuration of the DOI Compton camera. 47
4.4 Format of the list-mode data stored in the Compton camera 48
4.5 Energy resolution of the DOI Compton camera 59
4.6 Influence of back-scattering events 59
4.7 The number of hit pixel for 662 keV gamma rays 60
4.8 Energy cut regions for multi-source imaging 66

5.1 Source positions for the image response measurements 81
5.2 Spatial resolutions as measured for pattens 1−3 82

6.1 Scintillator configuration in the medical Compton camera. 90
6.2 Energy cut conditions for the medical Compton camera 94
6.3 RI tracers used for multi-color imaging 121
6.4 Features of radioactive tracers in mouse imaging 127
6.5 Comparison of the intensity of the radioactive tracers 132

Chapter 1

Introduction

Recently, the demand for gamma-ray imaging is growing in various fields including astronomy, nuclear medicine, homeland security, and environmental survey. However, accurate imaging of gamma ray is difficult because, unlike optical light, gamma ray can not be focused by using lenses or mirrors, thus a number of imaging techniques have ever been studied and developed. Compton camera, that is the imaging devices utilizing the Compton kinematics, is one of the promising detectors for imaging in wide energy range from hundred of keV to MeV gamma rays.

The first concept of Compton imaging was proposed by Schøenfelder in 1975 for the gamma-ray astronomy. In fact, the most successful application of Compton camera in space was the imaging Compton telescope (COMPTEL) as shown in Fig. 1.1, which was onboard Compton Gamma-Ray Observatory (CGRO) launched in 1991 [1, 2, 3, 4]. COMPTEL was the first Compton telescope which conducted observation on satellite orbit. COMPTEL consisted of liquid scintillator and inorganic scintillator NaI(Tl), characterized by high background rejection performance. In consequence, COMPTEL succeeded in achieving significant contributions in MeV gamma-ray astronomy such as providing the information of the distribution of ^{26}Al [5]. As shown in Fig. 1.2, COMPTEL achieved the highest sensitivity in the MeV energy region although over 20 years has past since then. As another accomplishment of Compton camera in astronomy, Ge detector based Compton camera succeeded in detecting Crab Nebula in 2011 [6].

Not only in the space experiments but in various other fields, the Compton camera has vast potential to revolutionize the conventional gamma-ray imaging. For example, in the radiography and X-ray CT system, we can obtain 2-D black-and-white image but energy information is completely lost. In contrast, the Compton camera makes 3-D multi-color imaging possible by estimating the direction of incident gamma rays based on Compton kinematics. In this study, we aimed to apply the Compton camera particularly to the fields of environmental radiation measurement and nuclear medicine. This thesis provides the

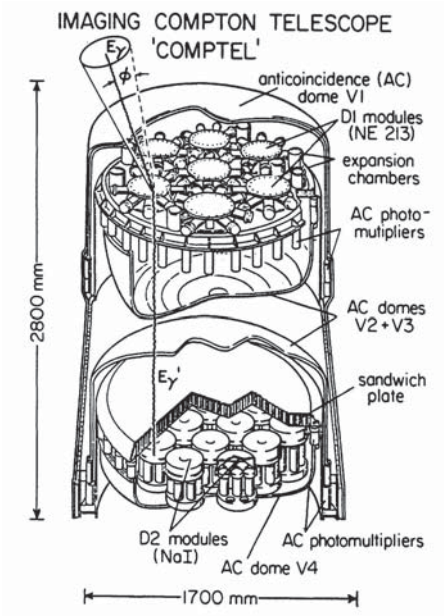

Figure 1.1: Outlook of the COMPTEL onboard Compton Gamma-ray Observatory [1].

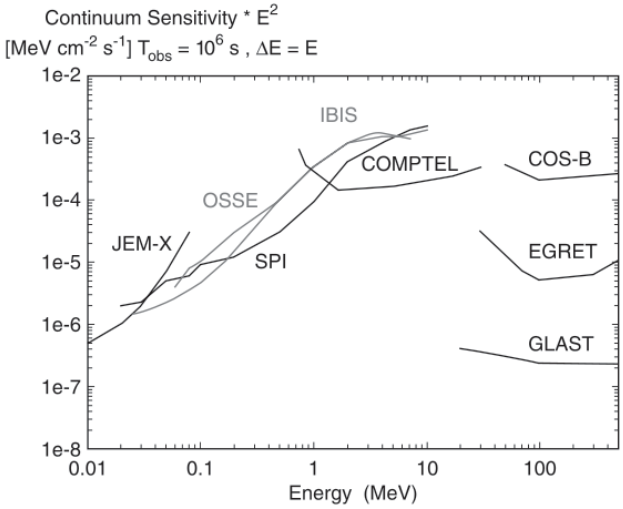

Figure 1.2: Sensitivities of the hard-X and Gamma-ray detectors on board astronomical satellites [4].

development of the Compton cameras which are suitable for each application, the imaging reconstruction, and experimental study for practical use in each fields. The structure of the thesis is as follows; Chapter 2 describes motivations and background studies in each fields. In chapter 3, basic interactions of gamma ray and principles of a Compton camera are summarized. In chapter 4, development, performance verification, and field tests of our handheld Compton camera for environmental measurement are described. In chapter 5, we studied 3-D reconstruction algorithm aimed at medical use. Chapter 6 report on the medical Compton camera from a standpoint of development, verification of its basic and imaging performances, and the results of small animal imaging. Finally, in chapter 7 we summarized and concluded our studies.

Chapter 2

Radiology Imaging

2.1 Environmental imaging

After the Japanese nuclear disaster in 2011, a large number of radioactive isotopes were released from Fukushima Daiichi nuclear power plant as shown in Fig. 2.1. Although several years have already passed since the accident, the residual radiation still remains a serious problem in Fukushima. Table 2.1 shows the amounts and characters of typical radioactive nuclides which were released to the environment. Among various types of isotopes emitted into the atmosphere soon after the accident as shown in Table 2.1, the dominant radioisotopes still remaining in the environment are ^{137}Cs and ^{134}Cs, as of 2016. Now the air dose rate has conventionally been measured by using dosimeters spot by spot. If we can quickly obtain the information of dose level as images over wide field of view (FOV), it may help in finding the radioactive hotspots within short time and this can reduce the exposure in decontamination operation. In order to identify such hotspots in environment, several imaging devices have been developed and commercialized since 2011 in Japan. In this section, typical imaging devices used for environmental measurement are introduced with its advantages and weaknesses.

2.1.1 Mechanical collimation method

One of the simplest gamma-ray imaging technique is the mechanical collimation method. The distribution of the source can be projected onto the detector by each photons which passed the collimator from a certain direction. The configuration of collimator directly affects imaging performances such as spatial resolution and efficiency. Fig. 2.2 shows two examples of typical collimator.

A pinhole collimator, which has an small circular hole like shown in Fig. 2.2 (a), magnifies the object as a function of the distance to the object and takes an advantage of providing high resolution images. The spatial resolution of pinhole collimators, R_{pinholle},

Table 2.1: Isotopes released from Fukushima Daiichi nuclear power plant [7]

Isotopes	amount of emission[Bq]	disintegration	decay time
^{242}Cm	1.0×10^{11}	α	162.8d
^{238}Pu	1.9×10^{10}	α	87.7y
^{240}Pu	3.2×10^{9}	α	6537y
^{239}Pu	3.2×10^{9}	α	24065y
^{241}Pu	1.2×10^{12}	$\alpha\beta^-$	14.4y
^{132}I	1.3×10^{13}	β^-	2.3h
^{135}I	2.3×10^{15}	β^-	6.6h
^{133}I	4.2×10^{16}	β^-	20.8h
^{131}I	1.6×10^{17}	β^-	8d
^{129m}Te	3.3×10^{15}	ITβ^-	33.6d
^{127m}Te	1.1×10^{15}	ITβ^-	109d
^{131m}Te	5.0×10^{15}	β^-	30h
^{132}Te	8.8×10^{16}	β^-	3.204d
^{91}Y	3.4×10^{12}	β^-	58.5d
^{89}Sr	2.0×10^{15}	β^-	50.5d
^{90}Sr	1.4×10^{14}	β^-	29.1y
^{99}Mo	6.7×10^{9}	β^-	66h
^{140}Ba	3.2×10^{15}	β^-	12.7d
^{143}Pr	4.1×10^{12}	β^-	13.6d
^{127}Sb	6.4×10^{15}	β^-	3.9d
^{129}Sb	1.4×10^{14}	β^-	4.3h
^{147}Nd	1.6×10^{12}	β^-	11d
^{134}Cs	1.8×10^{16}	β^-	2.1y
^{137}Cs	1.5×10^{16}	β^-	30y
^{239}Np	7.6×10^{13}	β^-	2.4d
^{141}Ce	1.8×10^{13}	β^-	32.5d
^{144}Ce	1.1×10^{13}	β^-	284.3d
^{95}Zr	1.7×10^{13}	β^-	64d
^{133}Xe	1.1×10^{19}	β^-	5.2d
^{103}Ru	7.5×10^{9}	β^-	39.3d
^{106}Ru	2.1×10^{9}	β^-	368.2d

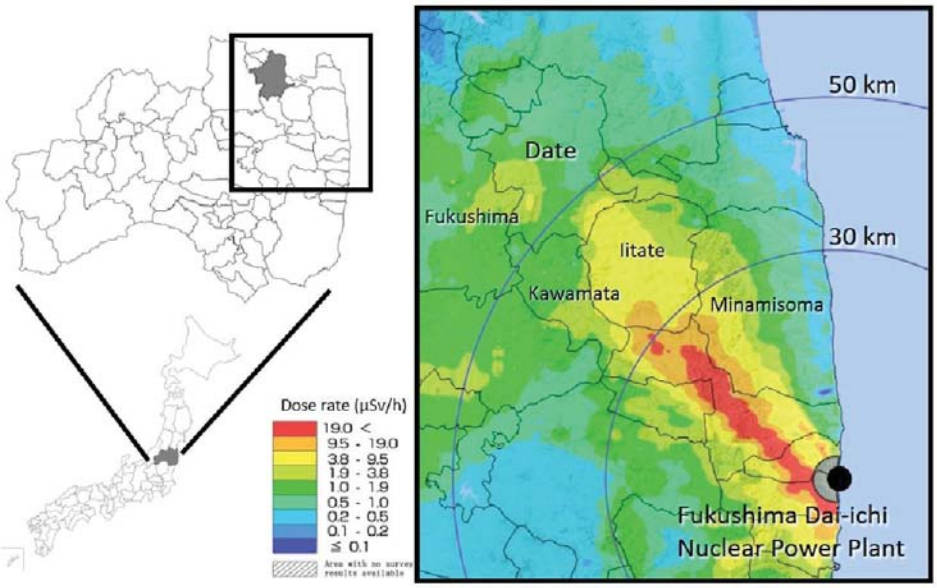

Figure 2.1: Dose rates map around Fukushima Daiichi Nuclear Plant as of November 5, 2011 [8]

can be theoretically calculated by

$$R_{\text{pinhole}} = \sqrt{(\frac{a}{b} \times R_{\text{detector}})^2 + (\frac{a+b}{b} \times d)^2} \tag{2.1}$$

where, the parameters a, b, d, and R_{detector} denote distance between the collimator and the detector, distance between the collimator and the source, diameter of the pinhole, and the resolution of the detector, respectively. On the other hand, the pinhole collimator has poor sensitivity because almost all photons are wasted and not reached on the detector surface. Hence, pinhole collimators are often used for proximity imaging such as small organs [9, 10, 11].

As another typical collimator, a parallel multihole collimator which has many holes arranged in parallel like shown in Fig. 2.2 (b) has also been widely used for a gamma-camera [12, 13]. With a parallel multihole collimator, the image size and the count rates do not largely depend on the distance to the object. The parallel multihole collimator resolution $R_{\text{multihole}}$ is given by

$$R_{\text{multihole}} = d \times \frac{l_e + b}{l_e} \tag{2.2}$$

where, the parameters b, d, and l_e denote distance between the collimator and the source, diameter of the holes, and the effective length of the collimator holes, respectively.

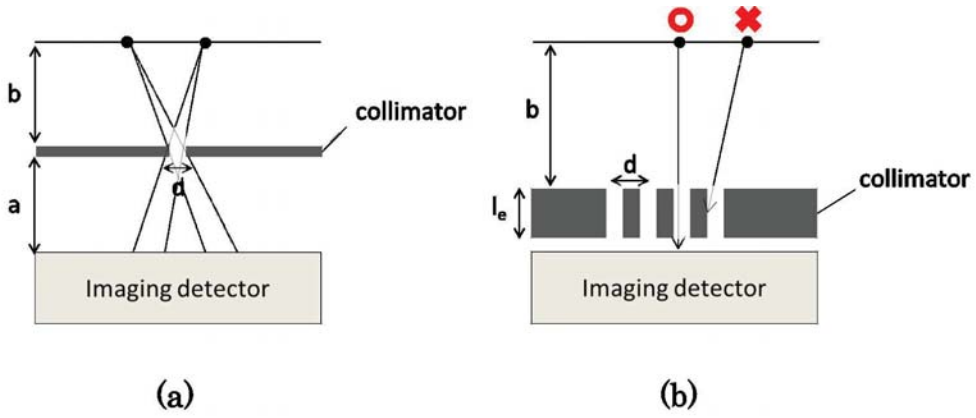

Figure 2.2: Schematic view of collimators of (a) pinhole camera and (b) parallel multihole collimator.

In general, the gamma camera with a collimator has the advantage of simple structure, however, the energy range of gamma ray that can be measured is limited to low energy because the collimator is almost transparent to high-energy gamma rays. Furthermore, in order to reduce the background contamination, the weight of the collimator-based gamma camera tends to become large by adopting thick a collimator and shields especially for stopping high-energy gamma ray.

In order to obtain gamma-ray distribution images, several gamma cameras based on these mechanical collimators have ever been developed and commercialized [14]. In particular, in order to identify radiation hotspots in environment a gamma camera based on the semiconductor detector was produced by Hitachi [15, 16]. It consists of CdTe detector with the size of $4 \times 4 \times 0.5\,\mathrm{cm}^3$ and a pinhole collimator made of tungsten, and the camera weights 15.9 kg (40 kg with internal additional shields). The camera features good energy resolution of $\sim$2 % at 662 keV and the practical spatial resolution of 0.68 m at a distance of 5 m was confirmed. Although the sensitivity of the gamma camera is not high under low dose late circumstances, this camera is conversely able to work in high dose environment such as in the nuclear power plant up to several-hundred mSv/h.

2.1.2 Compton camera in environmental measurement

In contrast to collimation method, a Compton camera estimates the source direction by utilizing the Compton kinematics. Although imaging process of Compton cameras is more complex compared to collimator-based gamma cameras, it is possible to develop a device in lightweight because Compton cameras do not require heavy shields to determine the directions of incident sub-MeV gamma rays. Note, in this context, that portability can be one of the key advantages of the device in the actual environmental survey. Furthermore,

Compton camera in general has a wide FOV of 180° compared to the collimation camera FOV of typically ∼60°.

Several Compton cameras for environmental measurement have ever been developed. The Polaris-H, which consists of 3D-position-sensitive pixelated CdZnTe (CZT) detector, has been developed in Michigan University for measurements at nuclear power plants [17, 18, 19]. The CZT detector size is $20 \times 20 \times 15\,\mathrm{mm}^3$, and the total device weights about 4 kg. In the detector, the depth of interaction (DOI) can be determined by using the time profiles of the cathode and anode signals [20], so that the detector provides 3-D interaction position information. This DOI method improves the angular resolution. The Polaris-H has excellent energy resolution of ∼1% (FWHM) at 662 keV, and the angular resolution is typically ∼20° (FWHM) for all 4π directions. As reference of sensitivity, the Polaris-H has the ability to image a ^{137}Cs point source producing ∼30 nSv/h within 5 min.

Another Compton camera based on Ge detectors has also been commercialized [21, 22]. It consists of two high-purity Ge (HPGe) detectors implemented in a DSSD configuration. The angular resolution for 662 keV gamma ray is about 4°.

Furthermore, some Compton cameras have been developed in Japan for gamma-ray imaging in the field of Fukushima. One of the representative device is the Si/CdTe semiconductor Compton camera, whose product name is ASTROCAM (Fig. 2.3 (*left*)). The ASTROCAM is developed on the technologies of JAXA's Si/CdTe Compton camera for space development [23, 24, 25, 26]. The detector in a standard model consists of 8 layers of Si detectors and 4 layers of CdTe detectors, of which size is 5×5 cm [27]. The weight of camera unit is approximately 8−13 kg depending on specifications. As well as other semiconductor based Compton camera described above, it has good energy resolution of 2.2% (FWHM) for 662 keV gamma rays. The angular resolution and efficiency were 5.4° (FWHM) and 0.16 cps/MBq at 1 m, respectively. Tests of ASTROCAM have also been performed several times in Fukushima. Fig. 2.3 (*right*) shows an example image of field tests taken in the 20 km zone of the nuclear plant with an exposure time of 30 min.

In addition to these devices, there are several other Compton cameras for environmental imaging in Fukushima such as the Ce:GAGG scintillator based Compton camera [28] and the Gamma-I which consists of CsI (Tl) scintillators with 16 PMTs [29].

In the circumstances of relatively low dose rates under a few dozen μSv/h, high sensitivity of detector is required for imaging within practicable measurement time. In this aspect, Compton cameras tend to be more profitable than collimator-based gamma cameras.

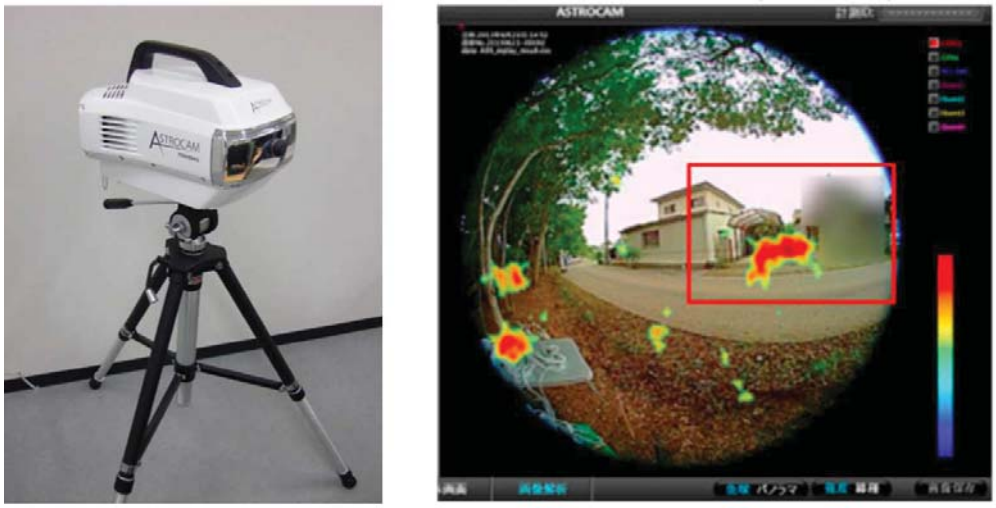

Figure 2.3: (*Right*) Photograph of the ASTROCAM, and ($left$) an example demonstration in the 20 km zone of the Nuclear Plant with exposure time of 30 min [27].

2.2 Medical imaging

As well as the environmental measurement, the demand for radiology imaging has also increased in medical field, especially for diagnostic imaging. Nuclear medicine, which utilizes gamma-ray emitting radioisotopes (RI) to have physiological information or information of lesions such as cancer and Alzheimer's disease, is one of the important branch of recent diagnosis. In contrast to the traditional imaging modalities such as X-ray imaging, computed tomography (CT) and magnetic response imaging (MRI) provide configuration images, in nuclear medicine diagnosis functional images of lesion can be obtained thus it produces a beneficial effect on early detection and treatment of diseases.

The nuclear medicine diagnosis is conducted by administering RIs into the patient body. Radiation detectors, surrounding the patient body, then detect gamma rays emitted from tumors to reconstruct an image. The used RIs differ from measuring function or target organs, and by its property these are divided into two categories; single-photon emitters and positron emitters. The single-photon emitting RIs emit a gamma ray which arises from electron capture (EC) or isomeric transition (IT). On the other hand, the positron emitting RIs produce a positron. The positron subsequently arises annihilation with an electron, generating a pair of 511 keV gamma rays which are emitted in 180° opposing directions.

In order to obtain precise and accurate information of these RI tracers distribution, instruments capable of visualizing the radionuclides have an important role. Here, representative imaging modalities for nuclear medicine are introduced in terms of image mechanism, advantages and disadvantages.

Table 2.2: Typical SPECT radioisotopes

Radioisotopes	Energy [keV]	Decay time	purpose
^{99m}Tc	141	6.0 h	
^{123}I	159	13.2 h	
^{131}I	364	8.04 d	
^{201}Tl	135/167/71	72.9 h	
^{133}Xe	81	5.24 d	
^{111}In	171/245	2.83 d	

2.2.1 Single photon emission computed tomography (SPECT)

Single photon emission computed tomography (SPECT) is the first method which can obtain tomographic images of biological distribution of radioactive medicines. SPECT images the 3-dimensional gamma-ray distribution by collecting data based on gamma camera from multiple angles. As the name indicates, SPECT is aimed at imaging single-photon emitters. The radioactive tracers which are typically used for SPECT are listed in Table. 2.2. The performances of the SPECT depend on the data collection condition such as the number of detectors, collimator type, sampling angle and interval, trajectory of the detector, and data collection time. In particular, the collimator has very important role in the performance of spatial resolution and sensitivity. In general, parallel hole collimator is applied: it is important to select suitable collimator considering target organ, measurement time, and data-collection method. The resultant image is reconstructed from the collection of projection data from multiple angles.

The first experiment of SPECT was conducted by Kuhl and Edwards in 1963 [30]. During 1970s and 1980s, rotating-camera SPECT systems were evaluated by several groups, and not only hardware but data processing methods to improve the images were proposed [31, 32, 33].

SPECT can provide various targeting abilities because it images single-photon emitters. However, since SPECT utilizes the mechanical collimator the energy of tracers for SPECT imaging is restricted to low range under $\sim$300 keV as shown in Table 2.2. In addition, the spatial resolution and the sensitivity of SPECT are not so good, so that many attempts to improve the imaging performances have been conducted in the latest SPECT studies.

2.2.2 Position emission tomography (PET)

As well as the SPECT imaging, positron emission tomography (PET) is one of the representative imaging modality in recent nuclear medicine. PET is the system which obtains positional information of the source by detecting back-to-back paired 511 keV annihilation gamma rays from positron-emitting radioisotopes such as ^{11}C, ^{13}N, ^{15}O, and ^{18}F. These

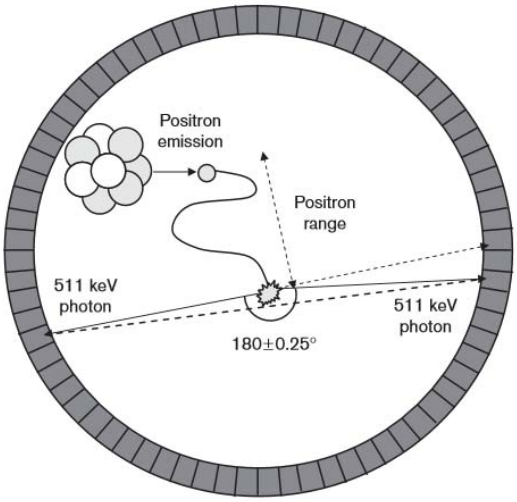

Figure 2.4: Schematic diagram of PET [34].

RIs are labeled to natural metabolites such as glucose and distributed inside the body through biochemical reaction. The typical PET detector consists of a number of detection units which are arranged in a ring structure as shown in Fig. 2.4. In contrast to SPECT, PET utilizes the coincidence events and the existence probability of each event is represented as a line of response (LOR) connecting the two interaction positions. The spatial resolution of PET depends on three factors: detector-related effects, positron range which is the positron-travel distance before annihilation, and photon non-collinearity because of the momentum for an emitted positron. The effects of positron range and photon non-collinearity are also described in Fig. 2.4.

The first positron emitter imager was proposed by Browenall and Sweet in early 1950s [35]. In recent years, in order to improve detector performance of PET various technologies have been applied. DOI measurement is one of the important technology for achieving a high spatial resolution over the entire FOV. The principles and various techniques in previous studies are described in section 4.3.2. Time of Fright (TOF) is another technique for improving the PET image quality. The TOF technique identifies the interaction position by utilizing the difference of arrival time of two gamma rays [36]. The TOF technique is effective to improve signal to ratio of reconstructed images, rather than image resolution.

Comparing with SPECT, one of the most important advantage of PET imaging is a much higher sensitivity by approximately 2−3 orders, that is because PET does not require physical collimators. Furthermore, PET imaging also provides good spatial resolution. Fig. 2.5 shows the typical spatial resolution across various SPECT and PET applications. For existing clinical application, SPECT and PET have the spatial resolution of around 10 mm and 5 mm, respectively. In addition, superior quantitative performance is also a

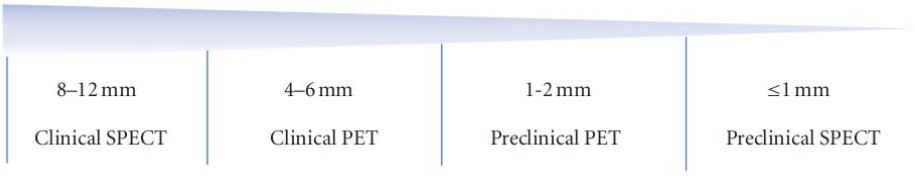

Figure 2.5: Spatial resolution across clinical and preclinical SPECT and PET images [37].

big advantage of PET imaging.

2.2.3 Compton camera in medical field

Although SPETCT and PET have been widely used and achieved valuable results in nuclear medicine, the radioactive tracers which are available for each modalities are restricted in the aspect of energy: SPECT only images tracers emitting low energy gamma rays of under ∼400 keV and PET can image only coincident gamma rays of 511 keV from positron-emitting source. On the other hand, Compton camera features very wide energy range, so that Compton camera can be a new promising detector that makes it possible to utilize various other radionuclides which have never been applied. Furthermore, this advantage of wide energy range enables the simultaneous imaging of multiple radioactive tracers which emit gamma rays of different energy. The simultaneous color imaging provides not only more detailed information of lesions at diagnosis, but perception that which element is relevant to a specific function at once [38].

The first use of Compton cameras in medical field was proposed in 1970s [39]. Since then, several attempts to utilize the Compton camera in nuclear medicine have been conducted [40, 41, 42, 43, 44, 45]. The semiconductor based Compton camera named GREI carried out multi-source imaging experiments [46, 47]. It consisted of two double-sided germanium (Ge) detectors. The dimensions of the active volume of Ge crystals are $39 \times 39 \times 10\,\mathrm{mm}^3$ and $39 \times 39 \times 20\,\mathrm{mm}^3$ for the scatterer and the absorber, respectively. The strip pitch is 3 mm for both detectors. The absolute efficiency of the first GREI for 662 keV gamma ray emitted from 15 mm away is approximately 0.01%, and in the GREI-I I the sensitivity was improved by 2.3 times. In 2013, Motomura et al. proposed two- and three-dimensional mouse images injected three different types of radioactive tracers of $^{65}ZnCl_2$, $^{85}SrI_2$ and ^{131}I at the same time (Fig. 2.6) [38]. Furthermore, Munekane et al. applied the GREI to a biodistribution assay of Zn complexes [48].

Another approach for small animal imaging was also conducted by the Si/CdTe Compton camera which was developed by JAXA and University of Tokyo. Takeda et al. reported development the Si/CdTe Compton camera for medical imaging use and reconstruction method [49, 50]. Furthermore, they also provide the experimental results of imaging mul-

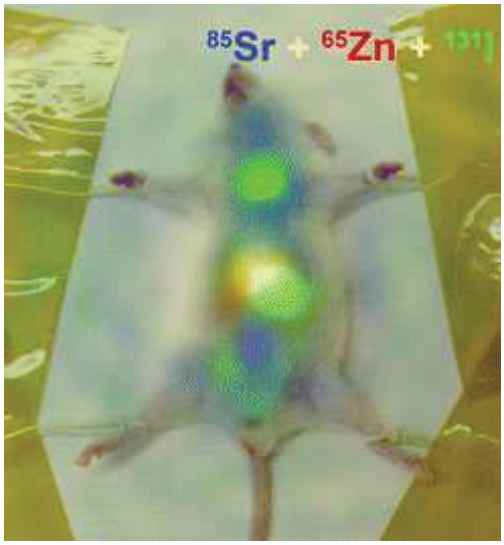

Figure 2.6: Multi-color mouse imaging using GREI [47].

tiple radiopharmaceuticals such as ^{131}I (364 keV) and ^{85}Sr (514 keV) injected into a living mouse. Although significant imaging results for both ^{131}I and ^{85}Sr were obtained, its measurement time of mouse imaging amounted to 6 hours. Long exposure is mainly due to relatively low sensitivity of the Si/CdTe camera. The detection efficiency for 356 keV at a distance of 10 cm was improved up to 3.4×10^{-4}% in the latest Si/CdTe Compton camera [25], while that of the existing clinical SPECT is typically approximately 100×10^{-4}%. Hence, improving the sensitivity becomes one of the problems to be solved for practical use.

In addition to these semiconductor-based Compton cameras, a Compton camera using implementing the gaseous detector, called the electron-tracking Compton camera (ETCC), was also developed by Kyoto University [51, 52, 53, 54, 55]. The ETCC consisted of two detectors; micro-time projection chamber (μ-TPC) based on the proportional gaseous pixel chamber as the scatterer and pixel scintillator detector such as GSO [56] or $LaBr_3$ [57] as the absorber. The most distinctive feature of the ETCC is the recoil electron tracking and restricting the direction of incident photon on the arc. From this effect, the ETCC can provide good signal to noise ratio even under low statistics. The typical spatial resolution measured at 511 keV was 11 mm (FWHM) at a distance of 10 cm from the detector. Kabuki et al. reported application the ETCC to small animal imaging: it imaged the head and thyroid gland of mice using double tracers of ^{18}F-FDG (511 keV) and ^{131}I ions (365 keV) [57] under the measurement time of 16 hours.

Thus Compton imaging is promising for largely expanding the field of nuclear medicine and these Compton cameras provide significant experimental results in small animal imag-

ing, but comparing with existing modalities there still remains challenging to be improved in practical use of a Compton camera. The one is poor sensitivity and long acquisition time. The detection efficiency of Compton cameras described above is still worse than that of SPECT or PET. Hence significant improvement of sensitivity is required for practical applications. In addition, image reconstruction method is far from being matured compared to current modalities such as PET. This is because the complexity of image reconstruction from Compton events, so that the performances of Compton imaging such as imaging accuracy and quantitativity is not enough compared to that of other devices. In order to achieve clinical use, these problems have to be overcome.

Chapter 3

Principle of Compton camera

3.1 Basic physics

3.1.1 Interaction of photons in materials

When photons in sub-MeV and MeV energy range interact with materials, the interaction of photons is classified into three processes; photoelectric absorption, Compton scattering, and electron-pair production. Fig. 3.1 shows dominant interaction process by photon energy and atomic number of the material.

In the photoelectric absorption process, incident gamma ray provides its all energy to an orbital electron, and then the orbital electron is ejected from the orbit as photoelectron. The photoelectric absorption process dominantly occurs especially at low energy range such as under 100 keV. The cross section of the photoelectric absorption has a relation with the energy of incident gamma ray E_γ and the atomic number Z described below:

$$\sigma_f \propto \frac{Z^n}{E_\gamma^{3.5}} \tag{3.1}$$

where, n has a value of 4−5 depending on E_γ.

As the energy of incident gamma ray increase, the dominant process gradually shifts from photoelectric absorption to Compton scattering. Fig. 3.2 shows a diagram of Compton scattering. The Compton scattering is an elastic scattering between a photon and an electron, so that a gamma ray is scattered to a different angle from incident direction after depositing a part of energy to the recoil electron. Assuming the recoil electron before scattering has no momentum, based on law of conservation of energy and momentum the energy of scattered gamma ray E'_γ is represented as

$$E'_\gamma = \frac{E_\gamma}{1 + \frac{E_\gamma}{m_e c^2}(1 - \cos\theta)} \tag{3.2}$$

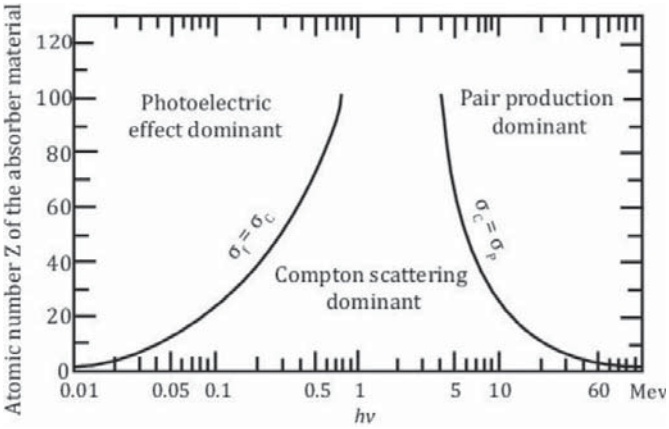

Figure 3.1: Dominant interaction process of photons in material [58].

where, θ is the scattered angle of the photon. The cross section of Compton scattering is given by Klein-Nishina formula:

$$\frac{d\sigma_C}{d\Omega} = \frac{r_e^2}{2}\left(\frac{E'_\gamma}{E_\gamma}\right)^2\left(\frac{E_\gamma}{E'_\gamma} + \frac{E'_\gamma}{E_\gamma} - \sin^2\theta\right) \tag{3.3}$$

where r_e=$e^2/m_e c^2$ (2.8×10^{-13} cm) represents the classical electron radius. The calculated distribution of differential scattering cross section for various energy is shown in Fig. 3.3. In addition, the cross section of Compton scattering is proportional to the atomic number Z

$$\sigma_C \propto Z \tag{3.4}$$

When the energy of incident gamma ray exceeds twice of rest mass energy of electron $m_e c^2$, electron-pair production process comes to occur. In electron-pair creation process, incident photon vanishes in the atomic Coulomb field, and produces an electron and positron pair. The cross section of electron-pair production depends on Z as follows,

$$\sigma_p \propto Z^2 \tag{3.5}$$

3.1.2 Compton kinematics

A Compton camera is a detector which aims to image gamma rays in the energy range from about a few hundred keV to several MeV, so that Compton scattering effect is dominant. Fig. 3.4 shows an example diagram of Compton scattering event in the Compton camera. A Compton camera generally consists of two detectors, often referred to scatterer and absorber. An incident gamma ray that has the energy of E_γ is first Compton scattered at the scatterer providing a part of energy E_1 to recoil electron, and then scattered photon

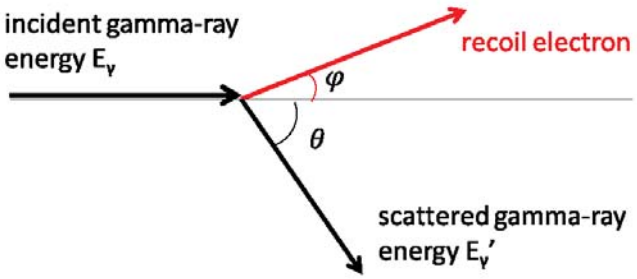

Figure 3.2: Diagram of Compton scattering

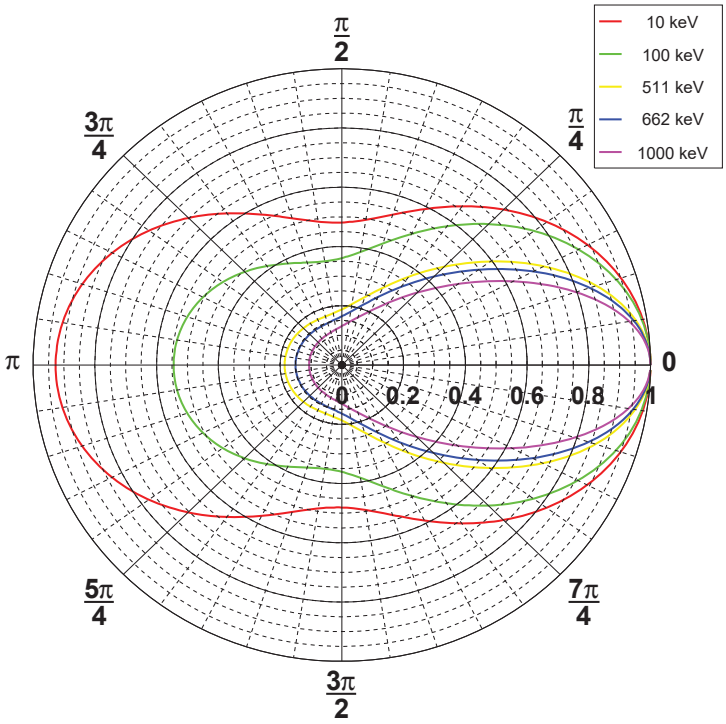

Figure 3.3: The angular distribution of Compton scattering calculated by Klein-Nishina formula

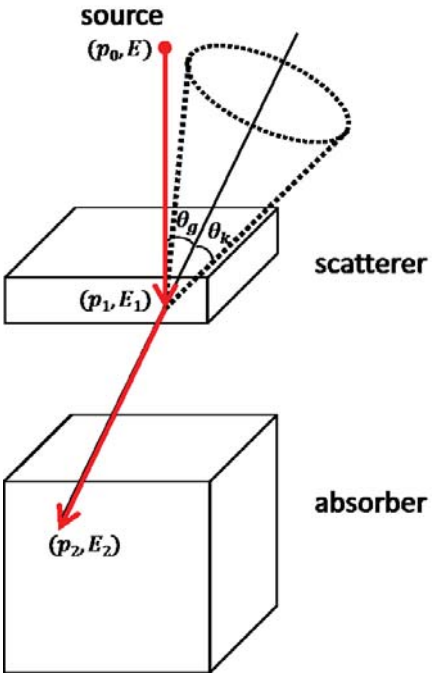

Figure 3.4: Basic concept of Compton camera.

is absorbed at the absorber depositing energy E_2. Using these observed quantities, the scattering angle θ is calculated as

$$\cos\theta = 1 - \frac{m_e c^2}{E_2} + \frac{m_e c^2}{E_1 + E_2} \tag{3.6}$$

$$E_\gamma = E_1 + E_2 \tag{3.7}$$

Fig. 3.5 shows that the relationship between Compton scattering angle θ and energy deposit E_1 for various incident gamma ray which has different energies E_γ. From θ and the information of interaction positions, the direction of each incident gamma rays can be constrained within a cone which has the vertex at the scattered position, that is called Compton cone. Therefore, accuracy of determination of energy and interaction position in the detector directly influence the performance of Compton camera.

3.2 Factors governing Compton Camera performance

The performance of Compton camera is generally characterized by two important parameters: angular resolution and detection efficiency. This section describes these parameters in detail.

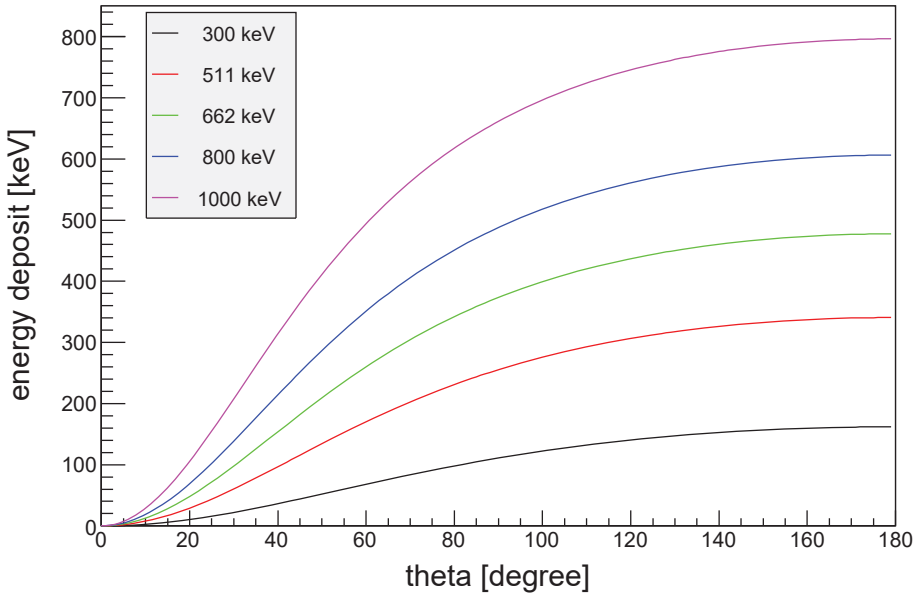

Figure 3.5: Relationship between Compton scattering angle θ and energy deposit E_1 for various incident gamma ray which has different energies E_γ.

3.2.1 Angular resolution

The angular resolution is one of the parameters which defines the imaging performance of Compton camera. In the evaluation of the angular resolution, the value of Angular Resolution Measure (ARM) is conventionally used. ARM is defined as the difference between actual scattered angle and reconstructed angle from measured information. As shown in Fig. 3.4, the incident gamma ray is first scattered at the position p_1 giving the recoil electron energy E_1 and then absorbed at the position p_2 depositing its energy E_2. The value of ARM is defined as following equation:

$$ARM \equiv \theta_k - \theta_g \tag{3.8}$$

where, θ_k represents the angle which is calculated from energy deposits (E_1, E_2) in the detector and θ_g represents the geometrical angle between the real direction of incident gamma ray and measured interaction positions (p_1, p_2);

$$\cos\theta_g = \frac{|\overrightarrow{p_0p_1}||\overrightarrow{p_1p_2}|}{\overrightarrow{p_0p_1} \cdot \overrightarrow{p_1p_2}} \tag{3.9}$$

Although in ideal θ_k equals to θ_g, measured energy and positional uncertainty in the detectors causes the degradation of the angular resolution. The angular resolution of

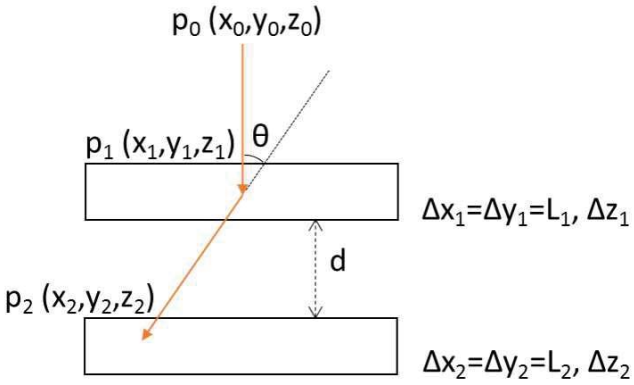

Figure 3.6: Parameter definition in calculating position uncertainty.

Compton camera is usually defined by the full-width at half-maximum (FWHM) of the ARM distribution. The reasons causing the uncertainty of the angular resolution are divided into three components: position uncertainty, energy uncertainty, and the Doppler broadening effect. In what follows, we discuss each elements.

Effect of positional uncertainty

The positional uncertainty where incident gamma ray interacts in the detector introduces an uncertainty of θ_g. The accuracy of position determination is generally defined by a pixel size of the detector, and the effect of the positional uncertainty largely depend on the detector geometry of the Compton camera. In order to estimate the contribution of the positional uncertainty to the angular resolution, we assume a geometry as shown in Fig. 3.6. An incident gamma ray emitted from $p_0 = (x_0, y_0, z_0)$ first scattered at $p_1 = (x_1, y_1, z_1)$ and then fully absorbed at $p_2 = (x_2, y_2, z_2)$. The scattered angle θ can be represented by

$$\theta_g = \arctan \frac{\sqrt{(x_1 - x_2)^2 + (y_1 - y_2)^2}}{|z_1 - z_2|} \tag{3.10}$$

Because θ is a function of x_i, y_i, and z_i $(i = 1, 2)$, the uncertainty of θ is calculated as bellow:

$$\sigma_\theta^2 = \sum_{i=1,2} \left\{ \left(\frac{\partial \theta}{\partial x_i} \right)^2 \sigma_{x_i}^2 + \left(\frac{\partial \theta}{\partial y_i} \right)^2 \sigma_{y_i}^2 + \left(\frac{\partial \theta}{\partial z_i} \right)^2 \sigma_{z_i}^2 \right\} \tag{3.11}$$

$$= \frac{\cos^4 \theta}{(z_1 - z_2)^2} \{ (L_1^2 + L_2^2) + \tan^2 \theta (\Delta z_1^2 + \Delta z_2^2) \} \tag{3.12}$$

where, L_1 and L_2 represent the pixel size of the scatterer and the absorber in both x and y directions, respectively. The term of $|z_1 - z_2|$ in equation (3.12) is comparable

to the average distance of two interaction positions in the scatterer and the absorber. The distance approximately depends on the detector distance d, hence equation (3.12) indicates that the contribution of geometrical uncertainty decreases with the increasing d. Fig. 3.7 shows the calculated uncertainty of angular resolution caused by the geometrical uncertainty under various pixel sizes. As obviously seen in Fig. 3.7, the angular resolution becomes smaller as the distance of $|z_1 - z_2|$ becomes larger. In addition, the thick detector may cause considerable degradation of the angular resolution at certain range of scattering angle. Therefore, in designing the Compton camera, the positional determination accuracy of the detector in depth direction directly influences the angular resolution.

Effect of Energy uncertainty

The energy uncertainty introduces the uncertainty of θ_k in equation (3.8). The scattering angle θ_k can be expressed as equation (3.6) with energy deposits E_1 and E_2. Hence, the uncertainty of θ caused by the energy uncertainty is calculated as follows:

$$\begin{aligned} \sigma_{\theta_k}^2 &= \sum_{i=1,2} \left\{ \left(\frac{\partial \theta_k}{\partial E_i} \right)^2 (\Delta E_i)^2 \right\} \\ &= \left\{ \frac{m_e c^2}{\sin\theta} \frac{1}{(E_1+E_2)^2} \right\}^2 (\Delta E_1)^2 + \left\{ \frac{m_e c^2}{\sin\theta} \left(\frac{1}{(E_1+E_2)^2} - \frac{1}{E_2^2} \right) \right\}^2 (\Delta E_2)^2 \end{aligned} \tag{3.13}$$

where,

$$\theta_k = \arccos\left\{ 1 - \left(\frac{m_e c^2}{E_2} - \frac{m_e c^2}{E_1+E_2} \right) \right\} \tag{3.14}$$

Then, by approximating $E_1 + E_2$ by the energy of incident gamma ray E_γ, σ_θ^2 can be represented as a function of θ and E_γ:

$$\sigma_\theta^2 = \left(\frac{m_e c^2}{\sin\theta} \right)^2 \cdot (\Delta E)^2 \cdot \left\{ \frac{1}{E_\gamma^4} + \frac{1}{E_\gamma^4} (1 - (1 + \frac{E_\gamma}{m_e c^2}(1 - \cos\theta))^2)^2 \right\} \tag{3.15}$$

where, ΔE is the energy resolution which is approximately proportional to $\sqrt{E}$. Fig. 3.8 shows the contribution of the energy uncertainty to the angular resolution under assumption of the energy resolution of 7% and 10% at 662 keV. Obviously, higher energy gamma ray results in the better angular resolution. Furthermore, the impact of the energy uncertainty to the angular resolution depend to a large part on the scattering angle. In other word, even within the same detector, the angular resolution can change significantly depending on scattering angle of each event. Thus, in order to reduce the contribution of the energy uncertainty to the angular resolution, it is useful to improve the energy

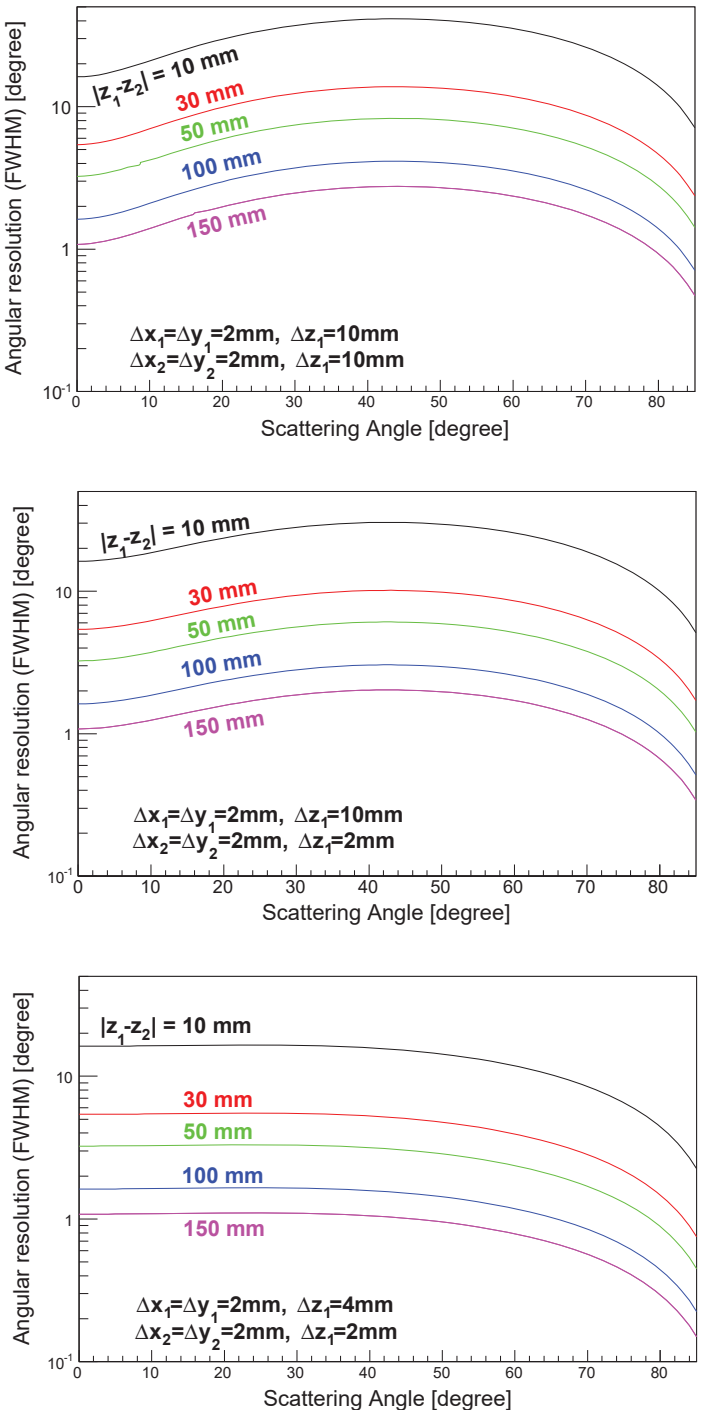

Figure 3.7: The uncertainty of angular resolution caused by the detector geometrical uncertainty. The pixel dimensions of the scatter and the absorber are (*top*) $2 \times 2 \times 10\,\mathrm{mm}^3$ and $2 \times 2 \times 10\,\mathrm{mm}^3$, (*center*) $2 \times 2 \times 10\,\mathrm{mm}^3$ and $2 \times 2 \times 2\,\mathrm{mm}^3$, and (*bottom*) $2 \times 2 \times 4\,\mathrm{mm}^3$ and $2 \times 2 \times 2\,\mathrm{mm}^3$, respectively.

resolution of the detector and select the optimum scattering angle by detector geometric configuration.

Doppler broadening effect

Even in the ideal detector which has no positional and energy uncertainties, the ARM always has finite width due to the momentum of scattered electron. This is known as Doppler broadening effect. In real detector, the electron before Compton scattering has momentum by nuclear or molecular orbit, thus Doppler broadening effect actually determines the theoretical limit of the angular resolution that can achieved with Compton cameras.

Because Doppler broadening is caused by scattered electron momentum, the degree of Doppler broadening effect depends on materials of the scatterer and the energy of incident photons. Fig. 3.9 shows the contribution of Doppler broadening effect to the angular resolution as a function of proton number. As can be seen from this figure, the Doppler broadening effect has a tendency to become large with increasing atomic number (Z), and also depends on periodicity; alkaline-earth materials have the smallest contribution and noble gases have the largest influence.

For describing the Doppler broadening, Klein-Nishina formula is insufficient and a more precise Compton cross section which includes the effect of electron initial momentum is required. Whereas Ribberfors [60] and Brusa et al. [61] analytically provide precise cross section model, here we estimated the Doppler broadening effect by using Monte Carlo simulation toolkit Geant4 described in section 4.7. In the simulation, gamma rays were irradiated to an ideal material which has no uncertainty both in positional and energetic, and the energy deposit in the material when Compton scattering occurs was recorded by each scattering angle. Fig. 3.10 shows the energy fluctuation $\Delta E'_{\gamma \cdot DP}$ by Doppler broadening effect in the case of one of the inorganic scintillator Ce-doped $Gd_3Al_2Ga_3O_{12}$ (Ce:GAGG) that is described in section 4.2.1 for 662 keV gamma rays. As the scattering angle becomes large, the degree of energy fluctuation also increases. This is because the larger momentum transfer of incident photon becomes, the more E'_γ is affected by the fluctuation caused by initial momentum of orbital electron.

By utilizing the FWHM value in Fig. 3.10 as $\Delta E'_{\gamma \cdot DP}$, we estimated the contribution to angular uncertainty caused by the Doppler broadening effect. The influence of Doppler broadening effect to the angular resolution can be calculated as follows. Assuming that the effect of Doppler broadening propagates to the energy of the scattered photon E'_γ, the degree of influence is converted to the uncertainty of scattered angle θ caused by energy

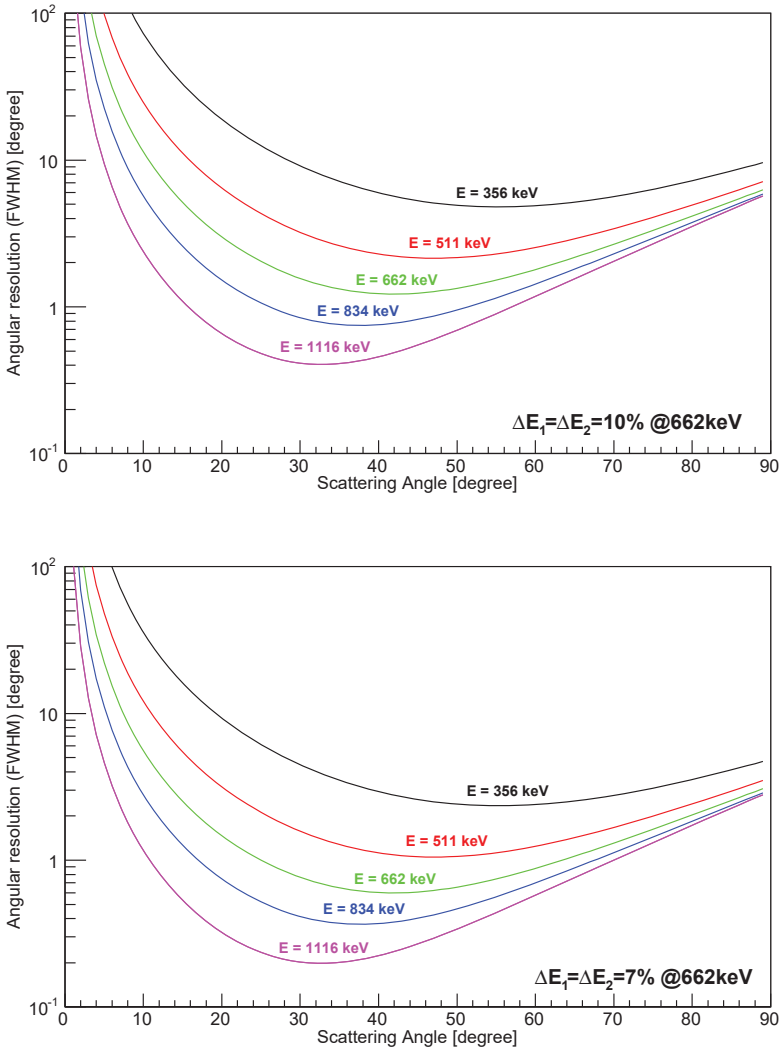

Figure 3.8: The uncertainty of angular resolution caused by energy uncertainty. The energy resolution was assumed as (*top*) 10% and (*bottom*) 7%.

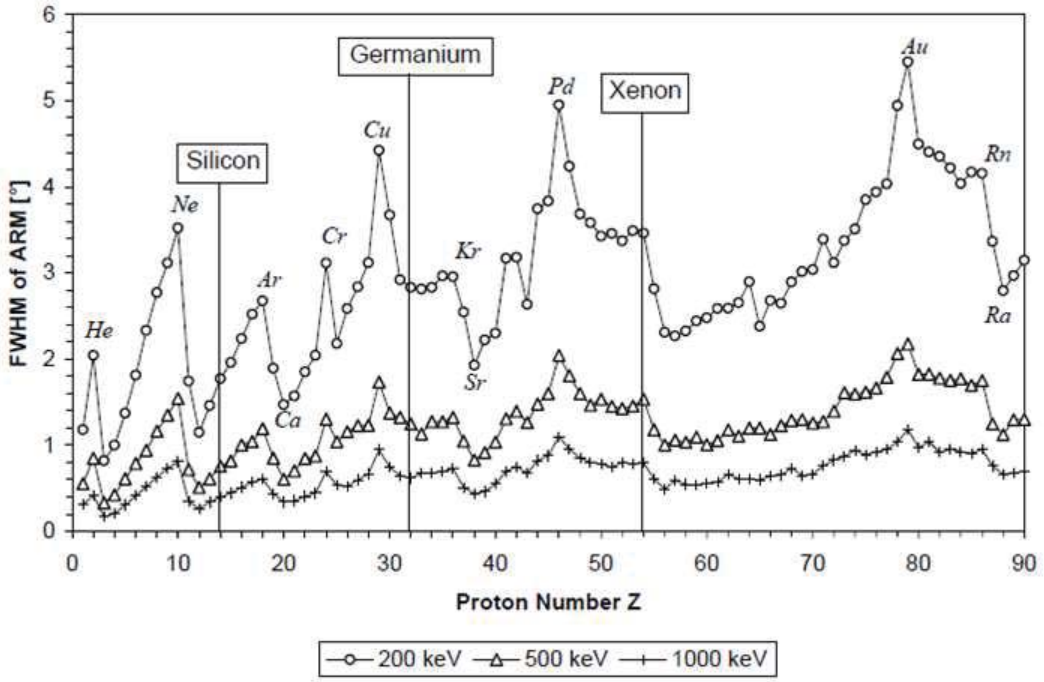

Figure 3.9: Doppler broadening effects as a function of proton number [59].

fluctuation of E'_γ. Using E_γ and E'_γ, the θ is given by

$$\theta = \arccos\left\{1 - m_e c^2 \left(\frac{1}{E'_\gamma} - \frac{1}{E_\gamma}\right)\right\} \tag{3.16}$$

Hence, the Doppler broadening effect can be represented as

$$\begin{aligned} \sigma^2_{\theta \cdot DP} &= \left(\frac{\partial \theta}{\partial E'_\gamma}\right)^2 (\Delta E'_{\gamma \cdot DP})^2 \\ &= \left\{\frac{1}{E_\gamma}\left(1 + \frac{E_\gamma(1-\cos\theta)}{m_e c^2}\right)\right\}^4 (m_e c^2)^2 \frac{1}{1-\cos^2\theta} (\Delta E'_{\gamma \cdot DP})^2 \end{aligned} \tag{3.17}$$

Fig. 3.11 shows the calculated result of the contribution of Doppler broadening effect in Ce:GAGG scintillator based on equation (3.17) for various energy of incident gamma rays. From this figure, it is confirmed that the angular resolution becomes significantly worse with increasing the scattering angle. For example, in Ce:GAGG scintillator, for 662 keV gamma ray the angular resolution caused by Doppler broadening effect is smaller than 2° (FWHM) within the scattering angle range of less than 90°, however, it increases to approximately 4° (FWHM) if scattering angle is around 140°.

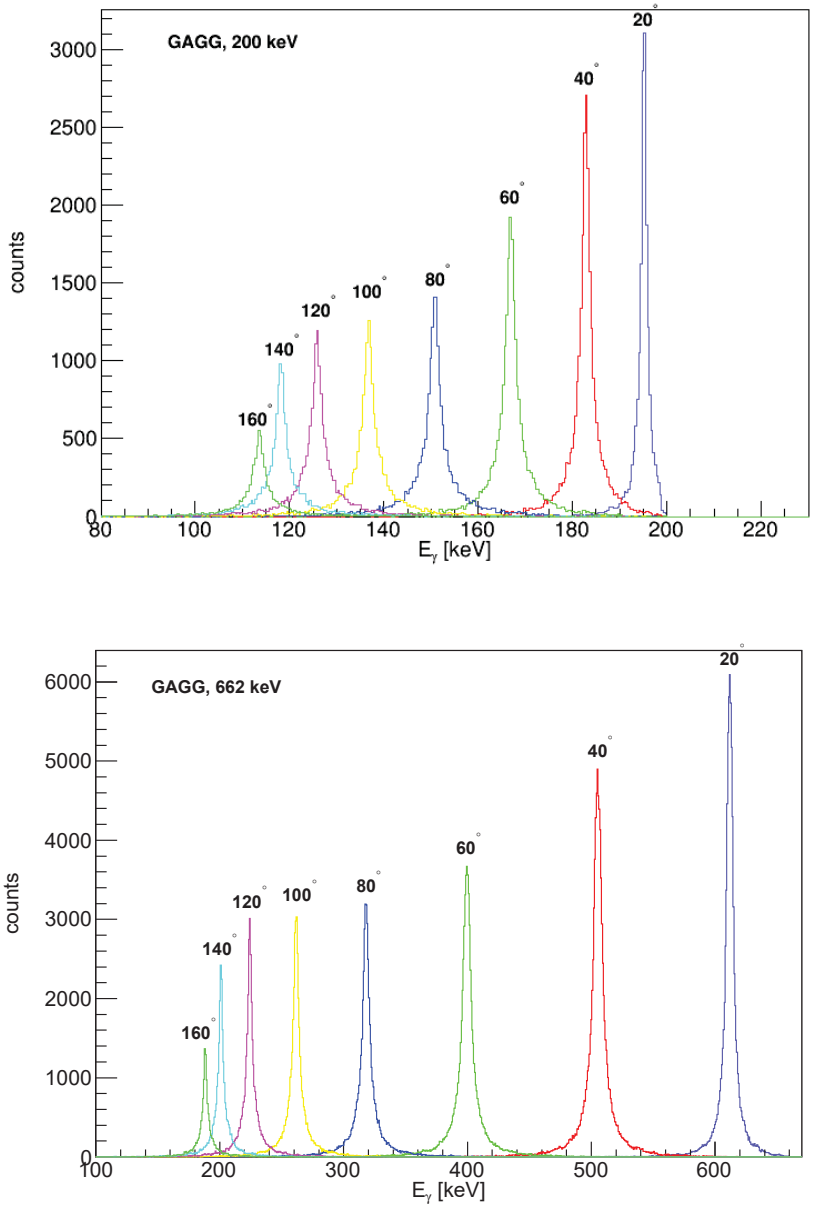

Figure 3.10: Doppler broadening effect in GAGG scintillator for (*top*) 200 keV and (*bottom*) 662 keV gamma rays.

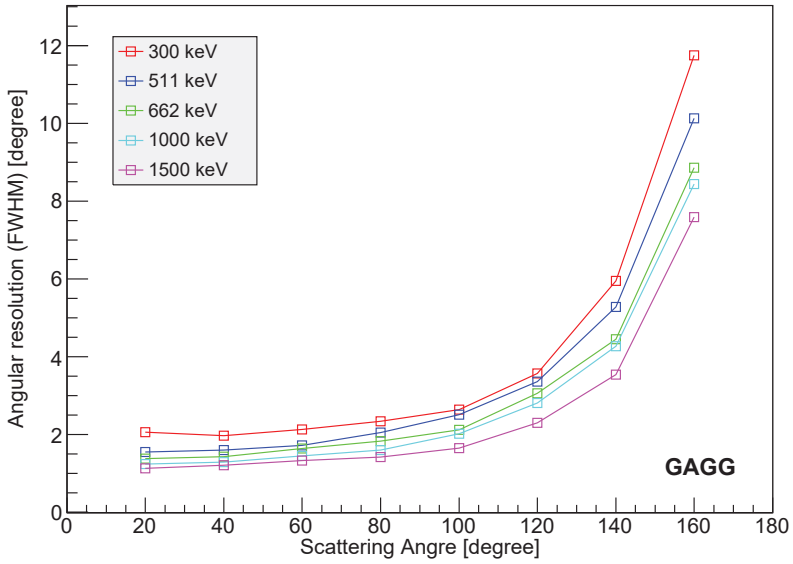

Figure 3.11: Contribution of the Doppler broadening effect in GAGG.

3.2.2 Detection efficiency

Another important factor which determines the performance of Compton camera along with the angular resolution is the detection efficiency. In general, there are two types of detection efficiency; absolute efficiency (ε_{abs}) which contains the effect of geometry between the source and the detector and intrinsic efficiency (ε_{int}) which is defined as the detection ability to incident events. Assuming the ideal situation of a point source which isotropically emits gamma rays, both efficiencies have the relation as

$$\varepsilon_{abs} = \frac{\Omega}{4\pi}\varepsilon_{int}, \tag{3.18}$$

where Ω represents the solid angle of the detector viewed from the source.

As described in section 3.3, all events which interact with the detector can not be necessarily applied for imaging. In developing and evaluating our Compton camera, we defined the efficiency by the events which passed the event selection and used for image reconstruction. Furthermore, in a Compton camera the detection efficiency complexly depends on various factors, such as the probability of Compton scattering in the scatterer, solid angle between the scatterer and the absorber, the probability of absorption in the absorber, and the effect of multiple scattering, so that it is not easy to derive it based on theoretical formula. Therefore, in this study we use the Monte Carlo simulation for calculating the detection efficiency.

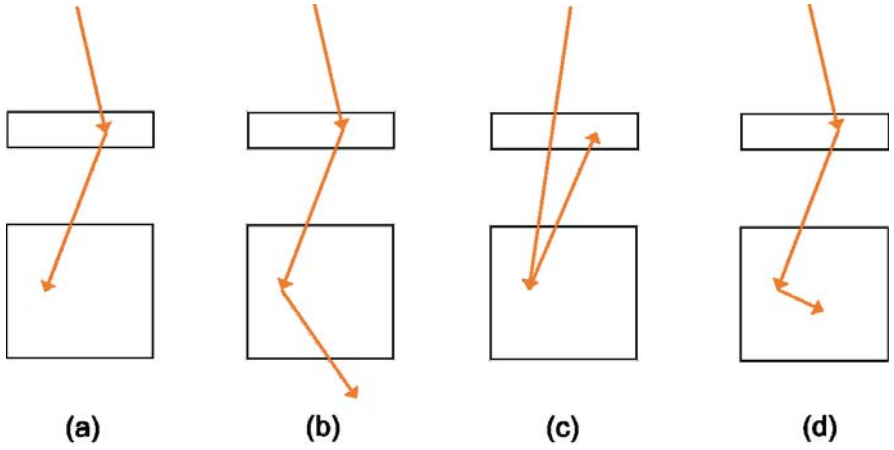

Figure 3.12: Typical hit patterns of gamma rays in Compton camera

3.3 Hit patterns of gamma ray in Compton camera

Although Compton camera utilizes Compton scattering events, there are various interaction patterns of gamma rays in the scatterer and the absorber and the patterns are not always ideal for reconstruction. Fig. 4.16 shows typical hit patterns of gamma ray in a Compton camera. Fig. 4.16 (a) is preferable event which is first scattered in the scatterer and then absorbed in the absorber. On the other hand, in the measured data there are also events that interact in other hit patterns like Fig. 4.16 (b)$-$(d). Fig. 4.16 (b) shows so-called escape event that scattered gamma ray does not fully be absorbed and a part of gamma ray escapes outside of the absorber. Fig. 4.16 (c) shows the back-scattering event which is firstly scattered in the absorber and then absorbed in the scatterer. As one of the representative technique in order to eliminate this back-scattering events, COMPTEL utilized Time of Fright (TOF) information and identified the order of interaction. The large distance between the scatterer and the absorber of 1.5 m makes the use of TOF information possible in COMPTEL, achieving good discrimination performance [2]. Fig. 4.16 (d) is multiple-scattering event that a gamma ray is scattered more than twice in the scatterer and/or the absorber. If the detector can read out the signals individually, the multiple-scattering events are correctly identified. On the other hand, in the case of using centroid method for position determination, the multi-scattering event in the same detector block is difficult to be discriminated.

These events cause false reconstruction and deteriorate signal to noise ratio on reconstructed image, so that event selection of measured data is very important. The detail study for event selection in our Compton cameras is described in section 4.6.

3.4 Image reconstruction

For gamma-ray imaging, not only detector performance but also image reconstruction method is important, so that many groups develop the reconstruction algorithm for Compton camera. In this section, we describe basic theory of the reconstruction algorithms applied in this study. Smith [62] provides an overview of existing reconstruction algorithms for Compton imaging. The reconstruction algorithms are divided into two major methods: analytical approach and statistical approach. Although many algorithms used to be based on the direct analytical approach because of the computational limitation in the past, recently the studies based on the statistical approach have been also general thanks to improvement of computational performance. In this study, we focused the statistical method aiming to improve imaging quality such as the quantitative accuracy. Here, we introduce the general concept of the reconstructed algorithms which used in this study.

3.4.1 Simple back projection (SBP)

The simple back projection (SBP) image reconstruction, in which the trajectory of each Compton cone is directly superposed in imaging space, is the simplest and the most basic method for image of Compton camera. SBP is computationally easy and fast, however, spatial resolution and signal to noise ratio of its image is not good because the rest of trajectory remained as background. In this study, we consider the cone distribution which is equal to the uncertainty of the cone determination.

Fig. 3.13 (a) shows the simulated result of the SBP image for a ^{137}Cs point source which is arranged at the center of FOV. The image is represented by the spherical surface as described in section 4.8.1. Although the source position is correctly reconstructed, the image contains substantial artifacts and the point source image spreads broadly. Hence in order to obtain more accurate gamma-ray distribution image, advanced reconstruction algorithm should be applied.

3.4.2 Maximum Likelihood Expectation Maximization (MLEM)

The Maximum Likelihood Expectation Maximization (MLEM) is one of the most widely used reconstruction algorithm in the field of Compton camera. The MLEM method statistically estimates an image using projection data based on iterative calculation. The MLEM method can be typically divided into two types according to the data set: bin-mode and list-mode. In bin-mode, the measured position and energy data set are once divided into bins and the size of measured data space is defined as the possible combination of the number of positions and energy bins. On the the other hand, in list-mode each measured data is directly reconstructed event by event, so that its size is determined by the number of measured events. In this study, we adopt list-mode MLEM because in

reconstruction of Compton camera the total volume of data space of list-mode tends to be much smaller than that of bin-mode. In addition, list-mode method has an advantage that the accuracy of image produces no deterioration by discretization.

Wilderman et al. [63] translated the bin-mode MLEM algorithm into list-mode. Moreover, Zoglauer et al. [64] provided the list-mode MLEM algorithm as following equation:

$$\lambda_j^n = \frac{\lambda_j^{n-1}}{s_j} \sum_{i=1}^{N} \frac{t_{ij} v_i}{\sum_k t_{ik} \lambda_k^{n-1}} \tag{3.19}$$

where, λ_j^n denotes the reconstructed image value after n^{th} iteration, s_j the probability that a photon emitted from image pixel j is detected, v_i the probability that an event i comes from the image space, t_{ij} the probability that a photon emitted from imaging pixel j is measured as the event i. Compared to the formulation in Wilderman et al. [63], equation (3.19) contains the additional factor v_i. The event has a non-zero probability that it came from outside the imaging space, especially in the case that Compton events with large cone sections in combination with small imaging space. The v_i is the factor for taking into account this effect in the reconstruction.

In the list-mode MLEM reconstruction, determining the parameters which describe the response of the imaging system becomes key point for reconstruction accuracy. Exact calculation of t_{ij} and s_j, which have to take into account the position and energy uncertainty of the detector, as well as Doppler broadening effect, is very complicated. Thus Wilderman et al. [63] provides that the system matrix t_{ij} can be determined by back projection cone which is calculated from measured data set of event i, which traces out a conic section in the image space. This approach showed reasonable results, so that many list-mode MLEM algorithms which were developed after that takes this method.

For an example of iterative algorithm, Fig. 3.13 shows the MLEM imaging results of ^{137}Cs point source by different iteration number. As increasing the number of iteration, we can clearly confirm that the spatial resolution of reconstructed image becomes better and artifact is significantly reduced. As an example, Fig. 3.14 shows the intensity of reconstructed image of a point source emitting 662 keV gamma rays as a function of the number of iteration. The vertical axis denotes the integrated value of 80 pixels around source position. The red and blue markers represent the source position of (θ, ϕ)=(0°, 0°) and (45°, 0°), respectively, and the open symbols show the case of half intensity of the closed symbols. Fig. 3.14 indicates that there is little fluctuation in the intensity values of both positions after 10 iterations, and the convergent intensities of the reconstructed image are consistent with real source intensities. Note that the appropriate number of iteration changes depending on such as the configuration of imaging object and the amount of statistics of measured data.

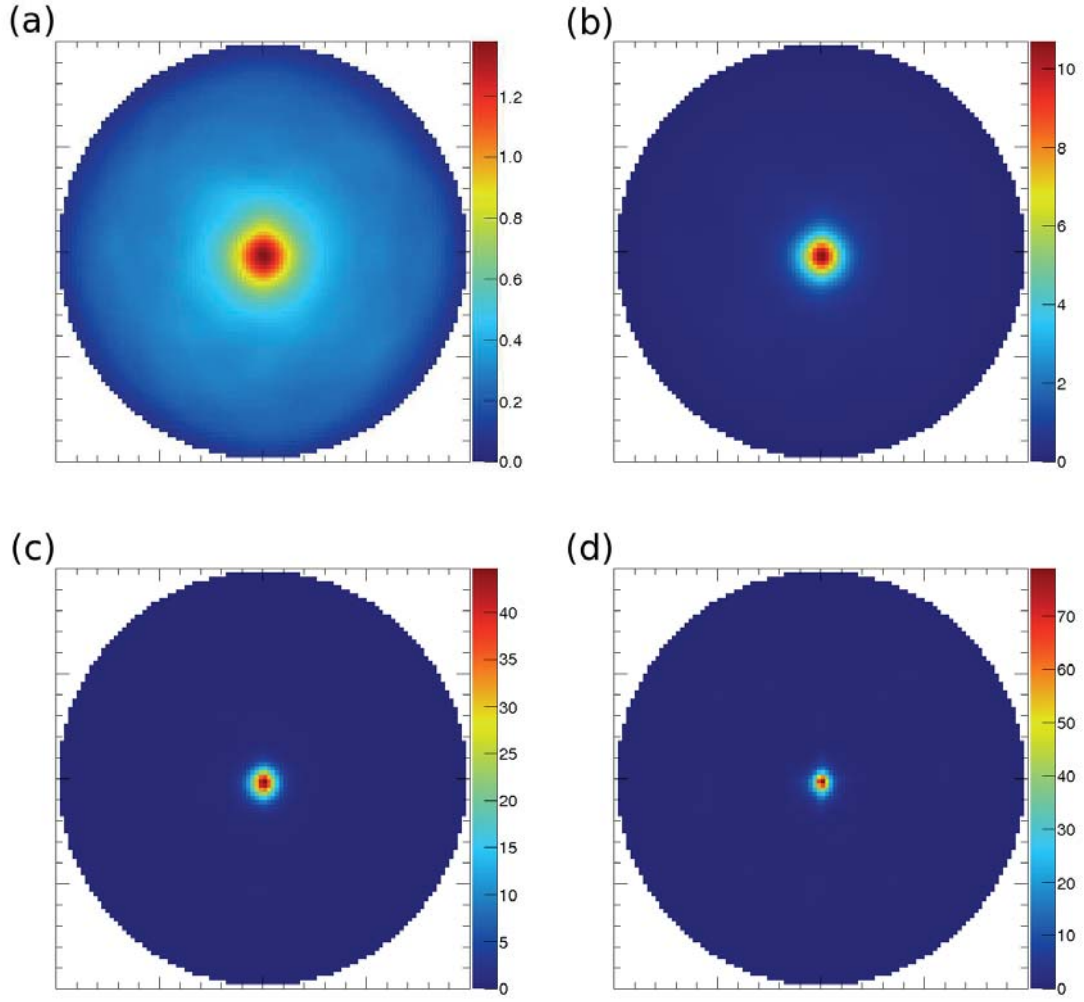

Figure 3.13: MLEM reconstruction images after (a) 1 iteration (equal to SBP image), (b) 3 iterations, (c) 10 iterations, and (d) 50 iterations, respectively.

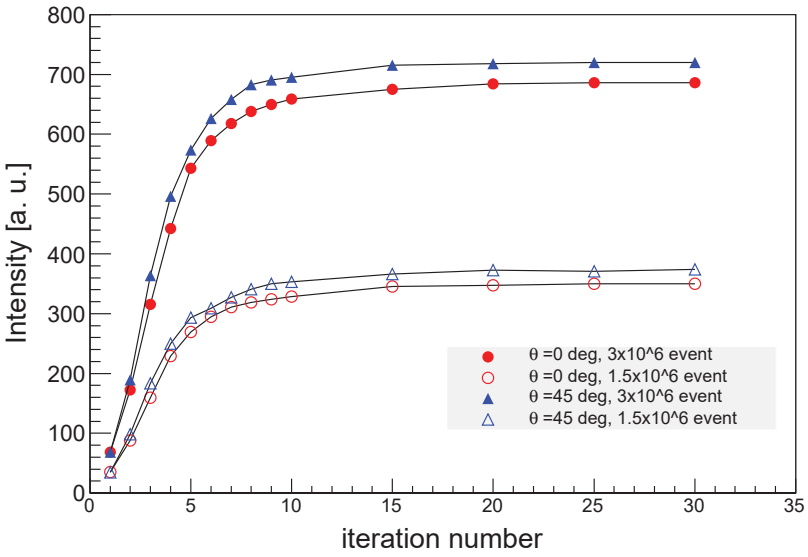

Figure 3.14: Intensity of reconstructed image as a function of the number of iteration. The red and blue markers represent the source position of (θ, ϕ)=(0°, 0°) and (45°, 0°), respectively.

Chapter 4

Compton camera for environmental measurement

4.1 Introduction

Although a number of gamma cameras and Compton cameras have been proposed for the purpose of environmental measurement to identify radiation hotspots after the Japanese nuclear disaster, there are still problems such that long measurement time required due to low detection efficiency and poor portability of heavy detectors. In this study, in order to realize quick and accurate gamma-ray imaging in the field work, we developed the handheld Compton camera consisting of inorganic scintillators of Ce:GAGG.

In this context, scintillator-based Compton camera has an advantage of high detection efficiency especially for high energy gamma ray such as 662 keV from ^{137}Cs, however, its angular resolution becomes in general lower than that of the semiconductor based camera because of the poor energy and position resolution. In order to overcome this situation, we invented a new method of 3-D position identification in a scintillator array, which makes it possible to significantly improve the resolution without reducing the detection efficiency.

In this chapter, the concept, development, and various simulation and experimental studies of the environmental handheld Compton camera are proposed.

4.2 Materials

4.2.1 Scintillator

For the scintillators implemented in the Compton cameras, the performances such as high energy resolution, precise position resolution, and appropriate density are required in order to obtain good angular resolution and detection efficiency. In this respect, we utilized Ce:GAGG scintillator [65, 66, 67, 68] both in the scatterer and the absorber. Table

4.1 shows the properties of Ce:GAGG as compared with other representative inorganic scintillators. Ce:GAGG features relatively large amount of luminescence and good energy resolution of around 6% (FWHM) for 662 keV gamma ray. In addition, since Ce:GAGG does not have hygroscopicity, good position resolution is expected by fabricating array configuration. Other characteristics of high density, reasonable decay time, and no intrinsic radioactivity are also advantageous for the detector of Compton cameras.

Table 4.1: Characteristic of Ce:GAGG and other scintillators.

	NaI(Tl)	CsI(Tl)	Ce:$LaBr_3$	Ce:GAGG
Density [g/cm^3]	3.7	4.5	5.1	6.6
Light yield [photon/MeV]	45000	56000	75000	57000
Decay time [ns]	230	1000	30	88 (91 %) + 258 (9 %)
Peak emission [nm]	415	530	375	520
Hygroscopicity	Yes	Yes	Yes	No
Intrinsic radioactivity	No	No	Yes	No

4.2.2 Multi-pixel photon counter (MPPC)

For the photo-sensor receiving light from the scintillators, we use Multi-pixel photon counters (MPPCs), also known as silicon photomultipliers (SiPMs) provided by Hamamatsu Photonics K. K.. MPPC is a semiconductor photodetector consisting of a number of geiger-mode avalanche photodiode (APD) pixels [69, 70, 71]. When a photoelctron is generated, an avalanche takes place in a pixel and provides the output charge Q which is given by

$$Q = C \times (V - V_{BR}), \tag{4.1}$$

where C, V, and V_{BR} denote the capacitance of the pixel, the impressed voltage, and the breakdown voltage, respectively. The total output charge from an MPPC is proportional to the number of the fired pixel. When the number of photoelectron is adequately smaller than that of the pixel numbers, output charge is proportional to the number of photoelectron. Because the MPPC is operated in geiger-mode, it has high gain of $10^5 - 10^6$. In addition, the MPPC is a thin detector compared to bulky photon multiplier Tube (PMT), thus the compactness of the sensor enables flexible design of the Compton camera as well as reducing amount of wasted material between the scatterer and the absorber.

For the use in handheld Compton camera, large area 8×8 monolithic MPPC arrays are particularly used. Fig. 4.1 shows a photograph of MPPC array consisting of the handheld Compton camera. Each monolithic array is arranged in 4×4 channels of 3.0×3.0 mm^2 effective area, and a whole MPPC array consists of 2×2 monolithic arrays. Thus, the total size of the effective area is 24×24 mm^2, and the size of APD pixel pitch is 50 μm.

Figure 4.1: Photograph of 8×8 MPPC array used in the DOI Compton camera.

The print board also carries a resistive charge-division network, which compiles the outputs from each 64 channels into four position encoded analog signals (denoted here as p1 to p4). Fig. 4.2 provides configuration and resistive value of the network. When an incident gamma ray is detected, the light outputs from the scintillator distributed several neighboring MPPC channels. Then the charge from each channel is divided into four signals in different weights depending on the channel position, so that by applying the centroid method to the four signals the interaction position can be calculated. Using the parameters in Fig. 4.2, we calculate the 2-dimensional interaction positions based on the following equations:

$$X = \frac{(p2 + p4) - (p1 + p3)}{\sum_{k=1}^{4} p_k} \tag{4.2}$$

$$Y = \frac{(p1 + p2) - (p3 + p4)}{\sum_{k=1}^{4} p_k}. \tag{4.3}$$

4.3 Depth of interaction (DOI)

4.3.1 non-DOI Compton camera

In our previous study, we developed so-called non-DOI Compton camera in conjunction with Hamamatsu Photonics K. K.. It is the first Compton camera developed by our team and utilizes only two-dimensional information for position identification in the scintillator block [72, 73, 74]. The non-DOI Compton camera also aims to apply the environmental measurements in the field, hence the non-DOI Compton camera features its compactness ($14 \times 14 \times 15\,\mathrm{cm}^3$) and the total weight is only 1.9 kg. Table 4.2 shows the scintillator

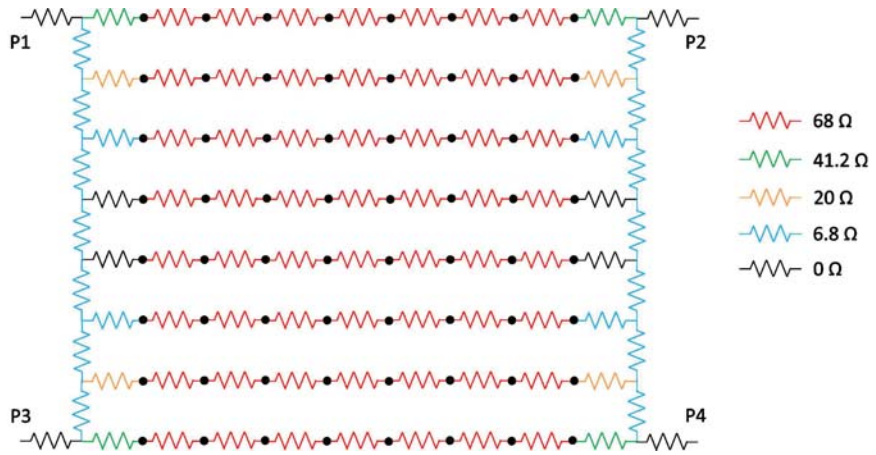

Figure 4.2: Resistive charge division network.

configuration of the non-DOI Compton camera. The angular resolution of the non-DOI Compton camera is around 14° (FWHM) for 662 keV gamma rays. Although high sensitivity is one of the great advantages of the camera, this performance of the angular resolution is not good as compared with other cameras based on semiconductor detector. This is especially due to the poor position resolution along thick scintillator length.

One of the simplest method to reduce the effect of the position uncertainty in the depth direction is to expand the distance between the scatterer and the absorber as described in section 3.2.1. However, the large distance also largely reduces the detection efficiency for coincident events. Another approach for improving the resolution is the 3-D position identification in the scintillator blocks. By obtaining not only 2-dimensional position information but also depth-of-interaction (DOI) position, we can reduce the contribution of the position uncertainty to the angular resolution without reducing the detection efficiency. Hence, in this study we aimed to achieve good performances both in the resolution and efficiency by applying the DOI method.

4.3.2 DOI technique for the handheld Compton camera

Historically, such DOI techniques have been studied and developed especially in the field of PET imaging. In the PET imaging, the DOI identification makes it possible to prevent degradation of the spatial resolution in the reconstructed image which arises from parallax error, so that in the past various DOI-approaches have been proposed. One of the most common method is pulse-shape discrimination called “phoswich”, which utilizes different decay time constants of several types of scintillator [75, 76, 77]. Another approach is measuring pulse-height ratio of continuous scintillators by dual-ended readout detectors [78, 79, 80, 81]. Other than those methods, the light sharing approaches by

Table 4.2: Scintillator configuration of the non-DOI Compton camera

Parameter	Value
SCATTERER	
Crystal dimensions	$1.5\,\mathrm{mm} \times 1.5\,\mathrm{mm} \times 5.0\,\mathrm{mm}$
Array	15×15 arrays, 2×2 set
Layer	1 layer
ABSORBER	
Crystal dimensions	$1.5\,\mathrm{mm} \times 1.5\,\mathrm{mm} \times 10.0\,\mathrm{mm}$
Array	15×15 arrays, 2×2 set
Layer	1 layer
DISTANCE	16 mm

changing reflector arrangement layer by layer [82, 83], and 6-side readout method with photo-detectors [84, 85, 86] are also utilized for DOI identification.

In our study, we have developed a novel-design module with DOI capability using MPPC arrays [87]. Fig. 4.3 shows the conceptual design of the DOI detector. The scintillator block consists of a number of discrete crystals, and the MPPC arrays are coupled at both ends of the scintillator block. Each scintillator pixel is divided by a reflector such as $BaSO_4$ and ESR in X-Y directions, shown as red line in Fig. 4.3. On the other hand, in the Z direction the layer of air intervenes in the pixels. When an incident gamma ray interacts in a certain scintillator pixel, the scintillation lights spread toward both ends along with the reflector, and each layer of air reflecting a part of the light. Thus the air layer contributes to making clear difference of light distribution depending on the depth position of gamma-ray interaction. By applying the resistive charge division network, the number of read-out channels which is need to read a scintillator block can be reduced to eight channels ($\mathrm{p_1}$−$\mathrm{p_8}$). The X, Y, and Z (=DOI) interaction positions are calculated based on the centroid method which is described as

$$X = \frac{(p2 + p4 + p6 + p8) - (p1 + p3 + p5 + p7)}{\sum_{k=1}^{8} p_k} \tag{4.4}$$

$$Y = \frac{(p1 + p2 + p5 + p6) - (p3 + p4 + p7 + p8)}{\sum_{k=1}^{8} p_k} \tag{4.5}$$

$$Z = \frac{\sum_{k=1}^{4} p_k}{\sum_{k=1}^{8} p_k}. \tag{4.6}$$

By applying this technique, we confirmed that the pixels can be 3-dimensionally resolved by 1 mm cubic for 662 keV gamma ray. See Kishimoto et al. [87] for more details.

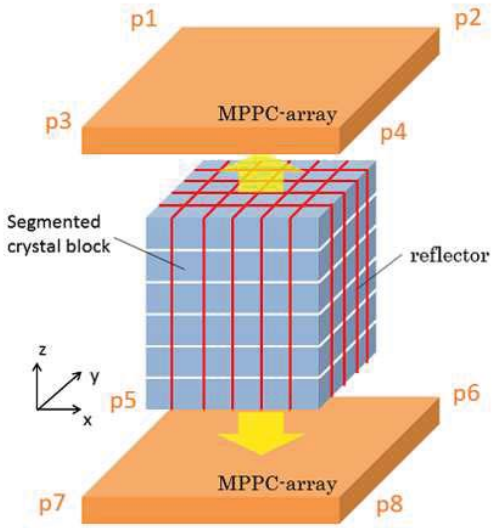

Figure 4.3: Schematic view of of the DOI method.

4.4 Geometric configuration

Based on the DOI method described above, we developed the brand-new handheld Compton camera, hereafter we call it the DOI Compton camera. Fig. 4.4 shows the overview of the DOI Compton camera. The whole size of the camera is $16\,\mathrm{cm} \times 15\,\mathrm{cm} \times 15\,\mathrm{cm}$ and its weight is 2.5 kg. The camera is composed of a gamma-ray detection unit, a signal processing unit, and a USB 3.0 interface.

In the gamma-ray detection unit, the scatterer and the absorber are both constructed of Ce:GAGG scintillators and 8×8 MPPC arrays. Table 4.3 lists the configuration of scintillator arrays of the DOI Compton camera. The scatterer is composed of two layers of scintillator arrays and each layer is coupled to a MPPC array. Although the probability of Compton scattering becomes large as the thickness of scintillator increases, the probability of interaction in the scatterer after the first Compton scattering also increases as the thick of the scatterer becomes large, so that the thickness of the scatterer has to be optimized. The configuration of the scintillator arrays described below is reflected the simulation results of optimization [88]. The pixel size of each crystal is $2.0\,\mathrm{mm} \times 2.0\,\mathrm{mm} \times 4.0\,\mathrm{mm}$ and each pixel is separated by ESR reflector of 0.065 mm. On the other hand, in terms of efficiency the absorber needs more thickness since it must absorb all energy of scattered gamma ray. The total thickness of the absorber is 20.0 mm, and the DOI measurement technique described above is applied in the absorber in order to prevent deterioration of the angular resolution. Each crystal size in the absorber is $2.0\,\mathrm{mm} \times 2.0\,\mathrm{mm} \times 2.0\,\mathrm{mm}$, and

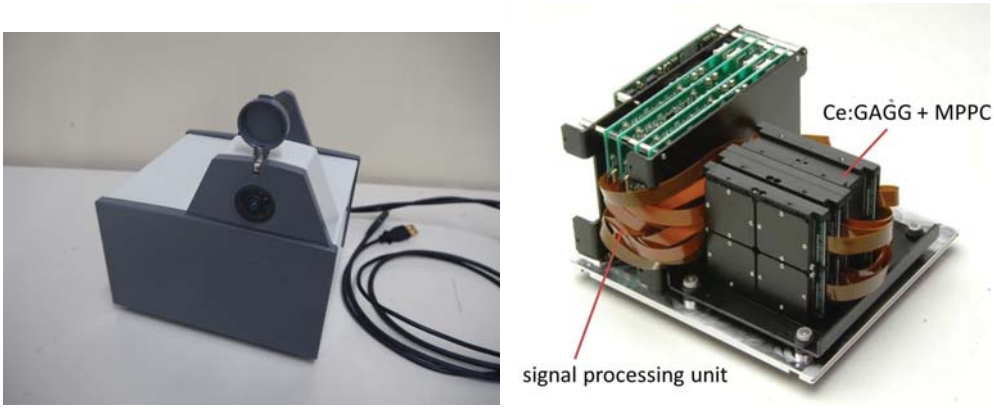

Figure 4.4: Photographs of the DOI Compton camera.

Table 4.3: Scintillator configuration of the DOI Compton camera.

Parameter	Value
SCATTERER	
Crystal dimensions	$2.0\,\text{mm} \times 2.0\,\text{mm} \times 4.0\,\text{mm}$
Array	11×11 arrays, 2×2 set
Layer	2 layer
ABSORBER	
Crystal dimensions	$2.0\,\text{mm} \times 2.0\,\text{mm} \times 2.0\,\text{mm}$
Array	$11 \times 11 \times 10$ arrays, 2×2 set
Layer	10 layer
DISTANCE	12.5 mm

there are 10 DOI layers. Fig. 4.5 shows the photograph of assembled scintillator array in the absorber. As well as the scatterer, ESR reflectors are inserted between each pixel in the X and Y directions, and the layer of air intervenes in the pixels in depth direction.

As shown in equation (3.12), the distance between the scatterer and the absorber also strongly influences both the angular resolution and detection efficiency. Here, the distance is set to 12.5 mm.

4.5 Readout system

Fig. 4.6 shows the read-out diagram of the DOI Compton camera. After passing through the resistive charge division network on the MPPC board, the signals from all MPPC arrays are fed into a signal processing unit through flexible flat cable (FFC). The signal processing board is composed of an application-specific integrated circuit (ASIC), analog-to-digital converter (ADC), programmable logic device (PLD), and a high-voltage power

Figure 4.5: Photograph of Ce:GAGG array used in the absorber.

Table 4.4: Format of the list-mode data stored in the Compton camera. The number in the parenthesis shows the size of each data [in unit of Byte].

header (3)	address (1)	time stamp (4)	Ch1 data (2)	Ch2 data (2)	Ch3 data (2)	Ch4 data (2)
header (3)	address (1)	time stamp (4)	Ch1 Offset (2)	Ch2 Offset (2)	Ch3 Offset (2)	Ch4 Offset (2)

supply (HVPS). The ASIC includes a pulse-shaping amplifier, baseline restorer circuit, comparator circuit, and peak-hold circuit [73].

The unit of signals from an MPPC array is named a "block", and a signal processing board handles up to four block signals. As shown in Fig. 4.6, the camera has four signal processing board, so that the readout system can read 16 MPPC arrays in total: eight of them are used for the two layers of the scatterer and the rest of eight are for the double-sided readout of the absorber.

When an incident gamma ray hits in a certain scintillator array, the information of address (board and block number), time, and four channel data of the block after resistive charge division network is measured and accumulated as list-formal data set. Table 4.4 shows the format of measured data set for an event. The whole data size for an measured event transferred to a personal computer (PC) is 32 byte. The address information includes the board and block number where the interaction occurs. With respect to each event offset data is also taken and the value that subtracts the offset from the raw data channel by channel is utilized for calculation.

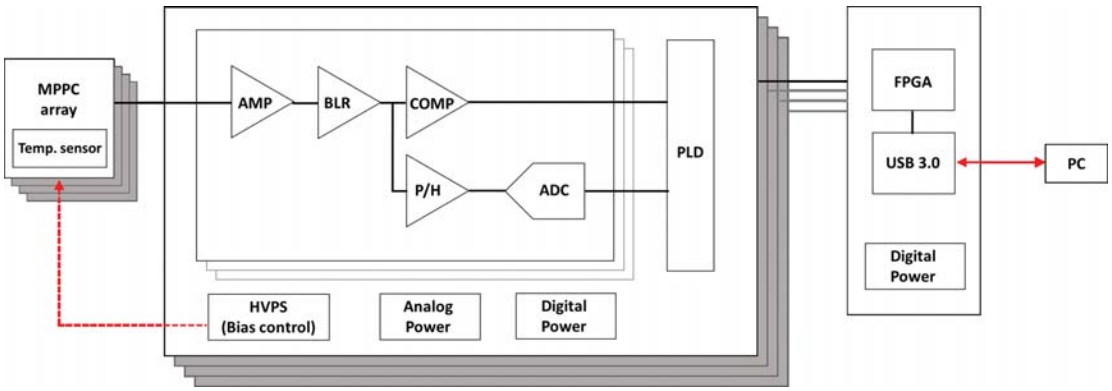

Figure 4.6: Read-out diagram of the DOI Compton camera.

4.6 Data analysis for event selection

In the DOI Compton camera, the event selection process is conducted after the measured data is transferred to a PC. Fig. 4.7 shows the series of flow of event selection.

All events are firstly converted from raw data to energy and position data. The energy information is calculated using the sum of the four channel data set in a block event by event. Since the linearity of MPPC output degrades when the number incident photons becomes large compared to the number of geiger-mode pixels, it is needed to convert the channel data to energy information appropriately. We conducted the energy calibration by each scintillator pixel, using energy referencing table. More details of energy calibration in the DOI Compton camera are described in appendix A. On the other hand, the position information is calculated based on the position identification equation (4.2)−(4.6) and the fired scintillator pixel is estimated with referencing the 3-dimensionally position region table which was made by each block beforehand. The detailed flow of positional identification is described in appendix B.

Then the coincidence events that one interacts in the scatterer array and the other in the absorber array are selected based on the time information. The coincidence time window can be changed in the software program, as the typical value set to 200 ns. The detected two-hit events which are satisfied the time coincidence are next checked whether they are satisfying the energy conditions. Fig. 4.8 shows an example of two-dimensional energy spectrum for 662 keV gamma ray, in which the horizontal and vertical axes denote the energy deposit in the scatterer and the absorber, respectively. The bright spot around $E_1 \simeq 200$ keV reflects the concentration of back-scattering events. Because these back scattering events cause the degradation of image quality, we aim to select only event that (1) the total energy deposit in the scatterer and the absorber (E_1+E_2) matches the concerned energy of incident gamma ray and (2) avoids the range of the back-scattering

concentration. For example, when imaging 662 keV gamma rays, we apply the following energy cut region as a default:

$$662 - 50\,\mathrm{keV} \leq E_1 + E_2 \leq 662 + 50\,\mathrm{keV} \tag{4.7}$$

$$10\,\mathrm{keV} \leq E_1 \leq 165\,\mathrm{keV}. \tag{4.8}$$

By applying this energy window, the back-scattering events can be significantly reduced. On the other hand, multiple-scattering events in single scintillator array (see Fig. 4.16) can not be eliminated from the data set used for image reconstruction because we utilize the centroid method. In addition, it is also difficult to distinguish the escape events which meets the energy conditions by chance despite that the energy of incident gamma ray is higher than the energy of interests. This arises from Compton scattering in the absorber and escaping a part of the energy. Although these escape events can be distinguished in the case that the energy of incident gamma ray is already known such as single-nuclides measurement, when conducting different multi-energy nuclides measurement the effect of the escape event has possibilities to become a problem. Hence, we will revisit this problem in section 6.5.5.

In our Compton camera system, the SBP and MLEM images are updated every second by referring the latest accumulated data over an arbitrary time using the events passed coincidence analysis and energy cut process.

4.7 Simulator of the DOI Compton camera

In order to study the response of the Compton camera, we developed a Compton camera simulator based on the Monte Carlo approach. For the simulator, we used the Geant4 4.9.6 software package [89] which is most standard in particle physics, nuclear physics, accelerator design, and medical physics. The main purpose of developing the simulator is to optimize the detector configuration and to search the physical interaction process in the detector which is not able to be known by experimental measurement.

Fig. 4.9 shows the Ce:GAGG scintillator configuration of the handheld Compton camera constructed by Geant4. The actual simulator replicates not only the active area of scintillator detector but the surrounding passive materials such as MPPC arrays, which consist of Si, glass epoxy board, and thin Cu board.

For the accurate simulation, it is essential to incorporate physical processes related to Compton camera precisely. In Geant4, several models exist even for the same interaction process, hence we have to apply appropriate model according to interested energy region. The developed simulator also takes account of the Doppler broadening effect. By the process of each event, this simulator provides the information of total energy deposit in

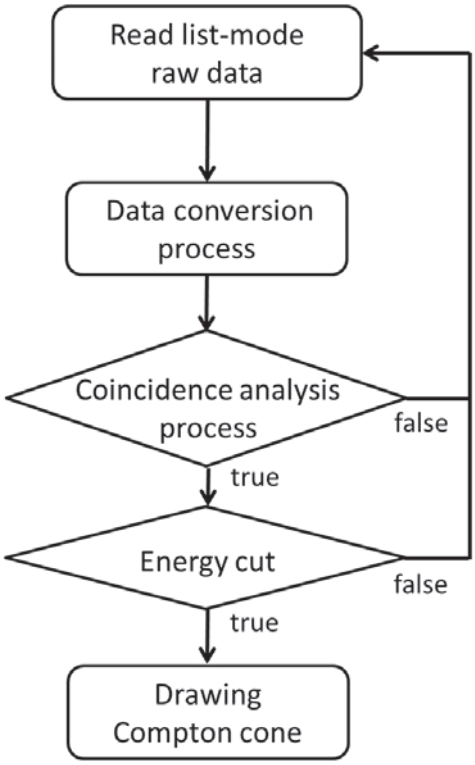

Figure 4.7: Flow chart of event selection.

the scatterer and the absorber, pixel ID where interaction occurs in scintillator array, the number of pixel that has energy deposit, and material ID where the first Compton scattering happens. If the number of pixels which have energy deposit is more than two in the scatterer or/and the absorber itself, the event means multiple-scattering event. Furthermore, by checking the material ID we can estimate whether the event is back-scattering event or not. Since these parameters can not be obtained in actual measurement, it is very meaningful to evaluate the influence of such events on the simulation. In the simulation, the energy deposit and position information in the scintillator are determined without any uncertainties. Hence appropriate energy and position resolution are considered according to the actual detector response. We assume energy resolution of 8.0% for 662 keV gamma ray, which reflects the actual measurement value of the detector (see section 4.9.2), and the resolution is given in proportion to $1/\sqrt{E}$ depending on the energy deposit.

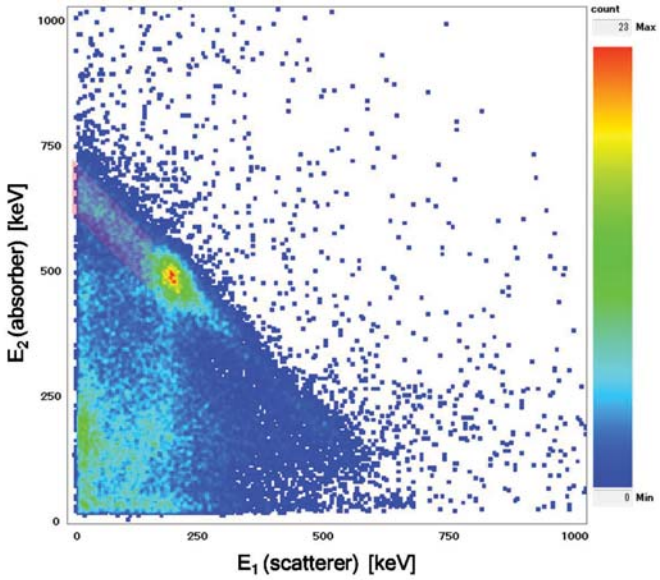

Figure 4.8: 2-D energy spectrum of the DOI Compton camera. The brightest spot (around $E_1 \sim 200\,\mathrm{keV}$) correspond to back-scattering events.

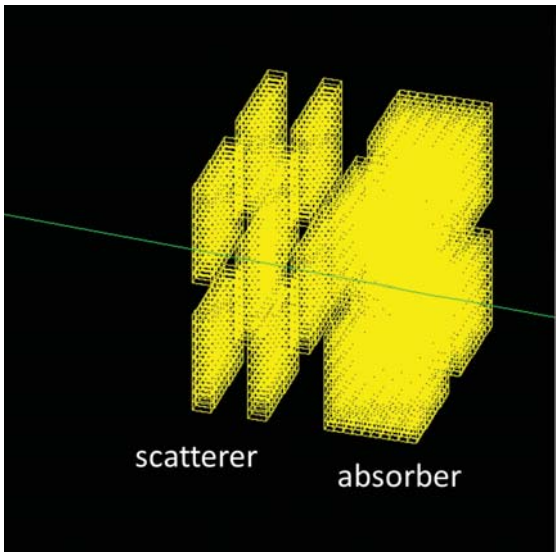

Figure 4.9: Scintillator configuration of the DOI Compton camera constructed using Geant4 simulation.

4.8 Image reconstruction

4.8.1 Image projection methods

In Compton camera imaging, the image is conventionally projected on 2-D plane, which is configured at the source position. However, in the case that the distance to the source is unknown as is the case in the environmental measurement, it is extremely difficult to assume the projection plane at appropriate position. For this reason, in imaging of the DOI Compton camera we applied spherical projection in place of the plane projection.

The spherical projection is the method that is often used for fish-eye view. In the spherical projection, there are several projection processes. For the projection of the DOI Compton camera, two types of processes are incorporated and can be switched to each other. The first one is equisolid angle projection that is represented by the following formula:

$$r = 2f \sin \frac{\theta}{2}. \tag{4.9}$$

In the equisolid angle projection, the area of image is proportional to the solid angle, hence the solid angle can be calculated by the image area. The other one is stereographic projection described as

$$r = 2f \tan \frac{\theta}{2}. \tag{4.10}$$

The stereographic projection has an advantage that the image is more similar to a sense of human sight in fish-eye imaging.

Fig. 4.10 shows the difference of the two projection process. Both method can image hemispherically over the 180° field of view. In the following imaging of the DOI Compton camera, we basically applied the equisolid angle projection method.

4.8.2 MLEM algorithm for the DOI Compton camera

Here, we describe specific MLEM reconstruction parameters in equation (3.19) for the handheld Compton camera imaging. The system matrix t_{ij} and v_i are calculated event by event as following formula:

$$t_{ij} = \exp\Big[-\frac{1}{2}\Big(\frac{|\Theta_j| - |\theta_k|}{\sigma}\Big)^2\Big] \times \frac{1}{\sin|\theta_k|} \tag{4.11}$$

$$v_i = \sum_j t_{ij}, \tag{4.12}$$

where Θ_j denotes the angle between the cone axis and the direction of the image pixel j, θ_k the scattering angle calculated by the energy deposit, and σ the intrinsic angular resolution of the Compton camera. The first factor represents the distribution of the Compton cone, which arises from the angular determination uncertainty. We consider the

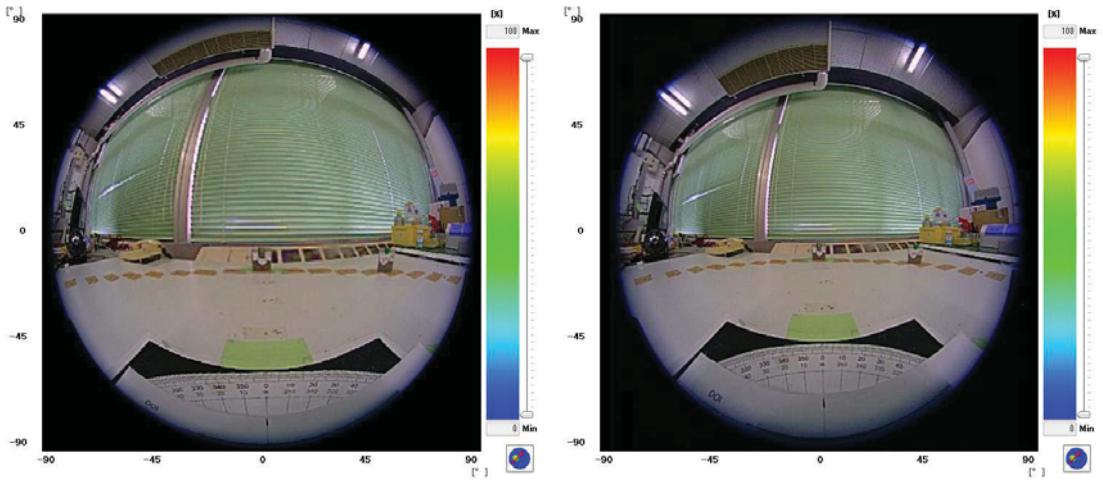

Figure 4.10: (*Left*) An example of equisolid angle projection image, and (*right*) an example of stereographic projection image.

distribution which corresponds to the angular resolution of the detector in the direction of vertically intersecting the Compton cone. On the other hand, the last factor is normalizing weight of each event regardless of the scattering angle. A circumference of the Compton cone is proportional to $\sin\theta_k$, thus the last term makes the integral value of each Compton cone equivalent weight.

The v_i, which is the probability that an event i comes from the image space in equation (3.19), is calculated by integrating the t_{ij} of the event i over the image region. The factor of background b_i is assumed to be zero in this study. Furthermore, we utilized the sensitivity map s_j which was estimated by the Geant4 simulator. In the simulator, we irradiated a given number of gamma rays isotropically and calculated the absolute detection efficiency at various representative positions on the imaging space. Then by interpolating spline function two-dimensionally the sensitivity data over whole the imaging region was developed. The sensitivity map differs by the energy of incident gamma ray, so that we conducted the same estimation by each energy of interest of gamma ray.

4.9 Detector performance

4.9.1 Position response of the scintillator

Fig. 4.11 and Fig. 4.12 show the position response of the 2-D and 3-D position-sensitive scintillator used in the scatterer and the absorber as measured for uniform irradiation of 662 keV gamma rays. Fig. 4.11 (*top*) and Fig. 4.12 (*top*) show the representative 2-D profiles in both detectors consisting of the events whose energy is over 10 keV. Fig. 4.11 (*bottom*) and Fig. 4.12 (*bottom*) show the 1-D profiles in each direction. The results of

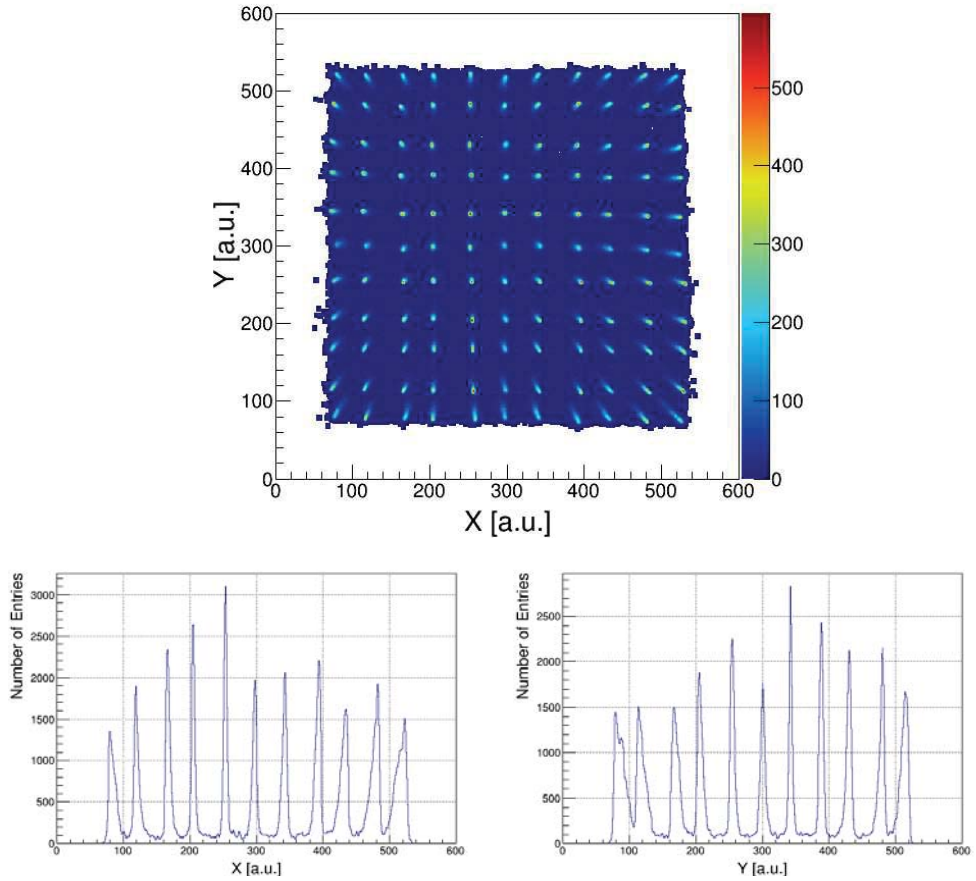

Figure 4.11: The position response of the scintillators in the scatterer. (*Top*) The 2-D segment map and (*bottom*) the 1-D profiles in X and Y directions.

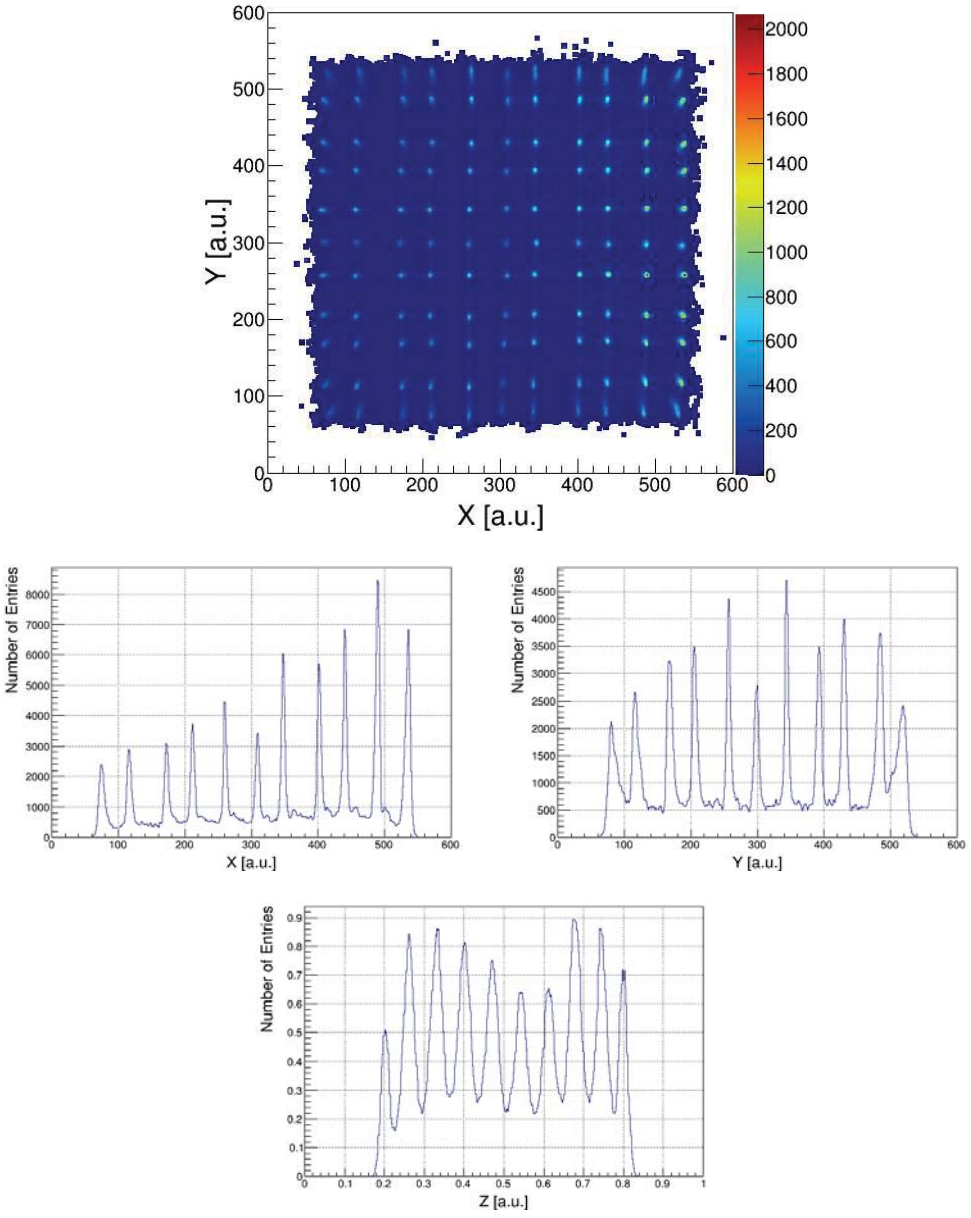

Figure 4.12: The position response of the scintillators in the absorber. (*Top*) The 2-D segment map and (*bottom*) the 1-D profiles in X, Y, and Z directions.

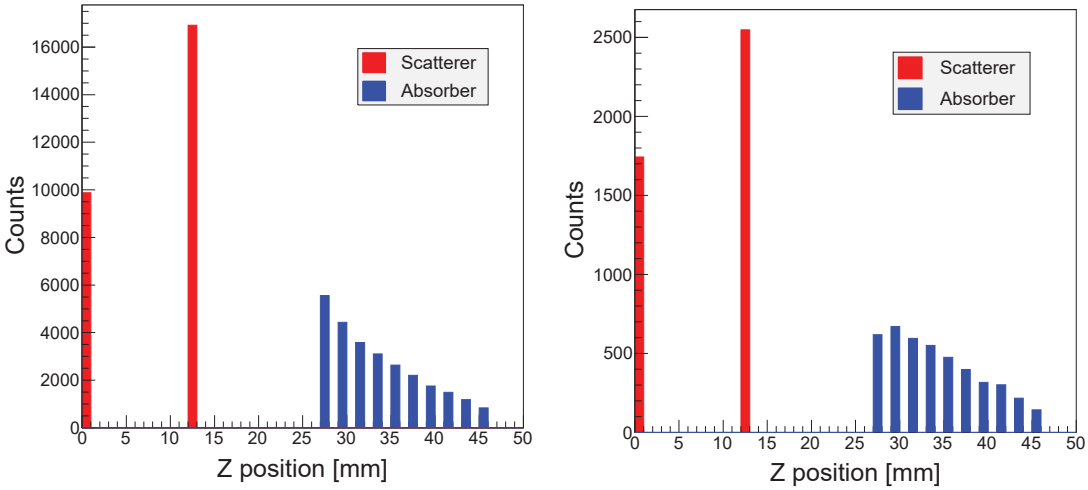

Figure 4.13: Experimental results of the number of hit events by each layer ($left$) before energy cut and ($right$) after energy cut (equal to events used for image configuration).

peak-to-valley ratio evaluation became 25.4 ± 3.0 (X) and 22.7 ± 2.6 (Y) in the scatterer, and 9.6 ± 1.0 (X), 6.1 ± 0.6 (Y), and 3.2 ± 0.1 (Z) in the absorber. From these results, we can confirm that the crystal responses are clearly distinguished each other in both two-dimension and depth direction.

Fig. 4.13 shows the distribution of the number of hit events by each layer. The horizontal axis represents the layer positions in the depth direction, and the red and blue bars denote the scatterer and the absorber layer, respectively. Fig. 4.13 ($left$) is the event distribution with coincidence selection and before applying the energy cut. On the other hand, Fig. 4.13 ($right$) is the distribution after applying the energy cut, which is equal to the events used for image reconstruction. Because the coincidence probability is higher at closer distance between the scatterer and the absorber, the hit events tend to concentrate in the second layer of the scatterer and in the upper layer of the absorber as shown in Fig. 4.13 ($left$). Furthermore, we can see that the event ratio in the second layer of the scatterer and the first layer of the absorber decreases after adapting the energy cut. This arises from rejection of the back-scattering event and restriction of the scattering angle by the energy cut for the scatterer. The interaction position of back-scattering events largely concentrate in these two layers, so that the effect of elimination of the back-scattering events appears as decrease in these layers. In addition, the energy cut for the scatterer also rejects a part of forward-scattering events which have more than certain scattering angle according to the relationship shown in Fig. 3.5. This effect also arises dominantly in closer distance between the scatter and the absorber.

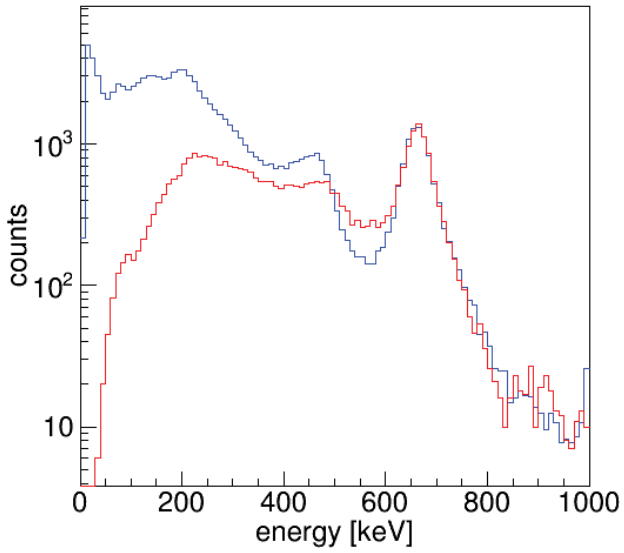

Figure 4.14: 1-D energy spectra irradiated from ^{137}Cs point source at the center of FOV. The *blue* and *red* lines represent the responses of the scatterer and the absorber, respectively.

4.9.2 Energy response

Next, we evaluated the energy response of both the scatterer and the absorber. Fig. 4.14 shows the 1-D energy spectra of the scatterer and the absorber. These were irradiated by a ^{137}Cs point source at the center of FOV, and spectra were accumulated before taking timing coincidence. Although 32 keV energy peak is clearly seen in the scatterer's spectrum, it is not confirmed in that of the absorber. This is because that the 32 keV gamma rays are fully absorbed in the scatterer and do not reach the absorber.

Table 4.5 shows the energy resolution of each layer for 662 keV gamma ray in both the scatterer and the absorber. The averaged energy resolutions are 7.8% (FWHM) and 7.4% (FWHM) in the scatterer and the absorber, respectively.

4.9.3 Signal to noise ratio

Although the event selection described in section 4.6 is applied for eliminating the events except for "true" Compton scattering event, we can not perfectly discriminate the noise contamination due to multiple-scattering event, escape event, and a part of back-scattering event as described in section 3.3 by the selection. Therefore, here we evaluated the signal to noise ratio and impact of these events after the event selection by using the simulator.

First, we evaluated the effect of the back-scattering event. Although the energy cut for

Table 4.5: Energy resolution of the DOI Compton camera for 662 keV gamma rays.

		E resolution [%]			E resolution [%]
The scatterer	layer 1	7.8±0.5	The absorber	layer 1	6.9±1.0
	layer 2	7.7±0.6		layer 2	7.3±1.1
				layer 3	7.8±1.2
				layer 4	7.4±1.3
				layer 5	7.4±1.1
				layer 6	7.6±1.2
				layer 7	7.5±1.5
				layer 8	7.9±1.6
				layer 9	7.2±1.7
				layer10	6.9±2.0

Table 4.6: Influence of back-scattering events in the image reconstruction.

	pure forward-scattering	before energy cut	after energy cut
forward-scatter	13761	13712	8178
back-scatter	0	5203	937
S/(S+N) [%]	100	72.5	89.7
resolution (FWHM) [°]	8.0	9.0	8.3

the energy deposit in the scatterer intends to reject the back-scattering events, the events used for image reconstruction still includes a slight back-scattering events. We compared the influence of the back-scattering events before and after adapting the energy cut when measuring 662 keV gamma ray from a ^{137}Cs point source at the center of FOV. Table 4.6 shows the results in terms of the number of forward-scattering and back-scattering events, its ratio, and the angular resolution which is estimated by using each events. Without energy cut (i.e. only time coincidence selection), we can see that the ratio of the back-scattering events to all events can be as high as 20% and the signal to noise ratio is 72.5%. On the other hand, by adapting the energy cut, although the total number of events slightly decreases, the signal to noise ratio is improved to near 90% in the case of center of the FOV. Fig. 4.15 shows the ARM distribution under each condition. The angular resolutions in the case of only forward-scattering events, before the energy cut, and after the energy cut are 8.0°, 9.0°, and 8.3°, respectively. The back-scattering events indeed cause the degradation of angular resolution, so that as this figure shows after the energy cut the angular resolution improves to the value which is expected for using the forward-scattering events only.

The other important noise factor is multiple-scattering events. In contrast to the back-scattering events, the multiple-scattering events can not be discriminated by experimental

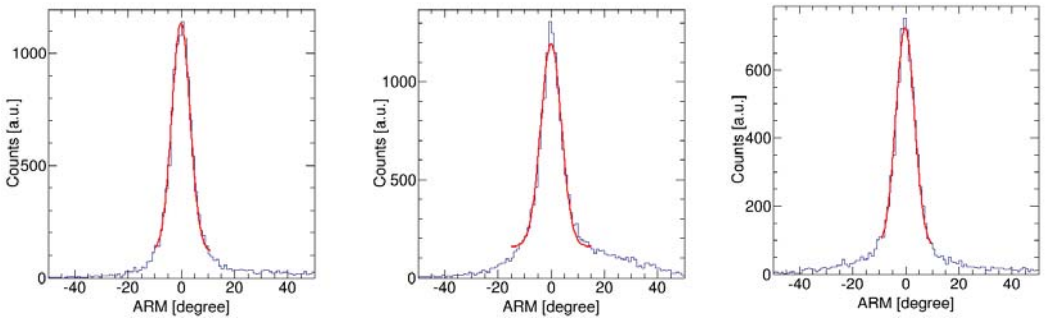

Figure 4.15: (*Left*) ARM distribution of pure forward-scattering events. The angular resolution obtained by FWHM of the ARM is 8.0°, (*center*) ARM distribution before adapting energy cut. The angular resolution obtained by FWHM of the ARM is 9.0°, and (*right*) after adapting energy cut. The angular resolution is 8.3°.

Table 4.7: The number of hit pixel for 662 keV gamma rays.

The number of hit pixel	scatterer [%]	absorber [%]
1	88.1	32.4
2	10.3	38.1
3	1.40	20.5
4	0.157	6.87
5	0.0108	1.72

selection such as energy cut because the position information of multiple interaction in the same scintillator block is lost at the step of readout. Fig. 4.16 and table 4.7 show the number of scintillator pixel which has energy deposit when 662 keV gamma rays are irradiated. The event referred to a single hit both in the scatterer and the absorber denotes the ideal Compton scattering event, and other events are the multiple-scattering events. Especially in the absorber, the ratio of the multiple-scattering is higher than that of the single hit. These events also deteriorate the angular resolution. Fig. 4.17 shows the comparison between the ARM distribution of pure scattering events and that includes multiple-scattering events when imaging a ^{137}Cs point source located the center of the FOV. By the influence of multiple-scattering events, the angular resolution becomes worse by nearly 1°. For the evaluation of the DOI Compton camera, this multiple-scattering effect is included both in the experimental and simulation performances.

4.9.4 Counting rate performance

In terms of the evaluation of the basic detector performance, tolerance to high counting rate is also important. It defines the upper limit of the source intensity which can be measured. We tested its performance by using ^{137}Cs point sources. We used 3 MBq ^{137}Cs

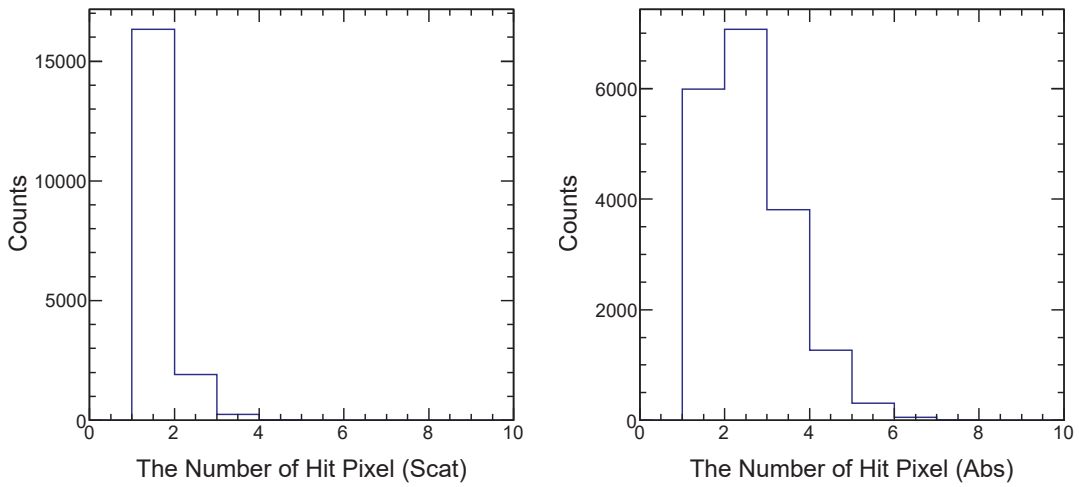

Figure 4.16: Hit pattern of multiple-scattering event ($left$) in the scatterer and ($right$) in the absorber.

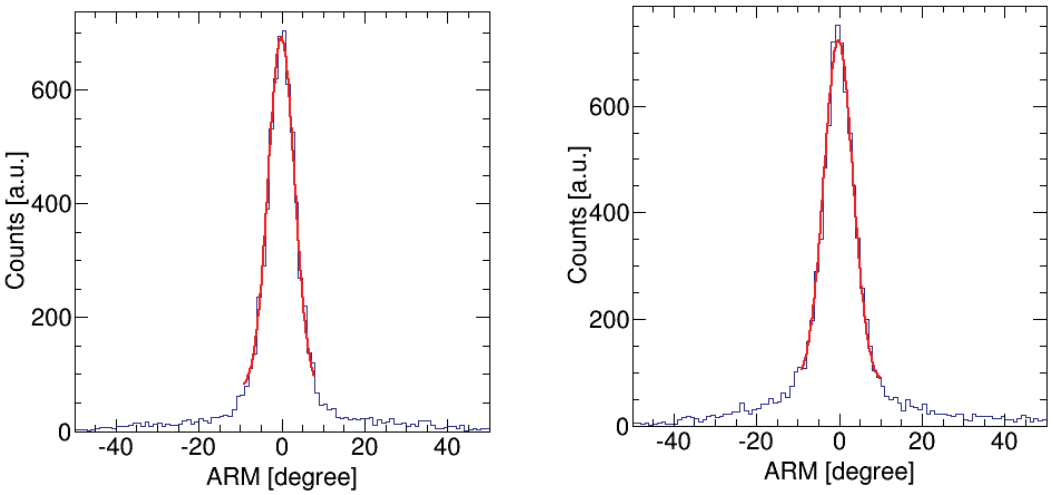

Figure 4.17: ($Left$) ARM distribution without multiple-scattering events. The angular resolution obtained by FWHM of the ARM is 7.4°, and ($right$) ARM distribution with multiple-scattering events. The angular resolution obtained by FWHM of the ARM is 8.3°.

source and measured the counting rate when changing the distance between the detector and the source. Fig. 4.18 shows the results of the counting rate: (*top*) is for the event before taking the timing coincidence, and (*bottom*) is for that after adapting timing coincidence and before energy selection to various timing coincidence windows. The horizontal axis denotes the distance between the camera and the source, and the vertical axis denotes the count rate measured with the DOI Compton camera. Without taking coincidence, the ratio increases linearly as the source distance becomes small over all coincidence windows. On the other hand, the ratio after taking timing coincidence is not linear in the range under the distance of around 7 mm. These results indicate the maximum counting rate is limited by a process of coincidence selection, and its maximum rate is around 150 Hz. They are mainly caused by the fact that the coincidence search on the software algorithm can not handle too many events at the same time because of a finite processing speed. Hence it depends on the performance of used PC such as CPU and memory.

In addition, as decreasing the coincidence time window we can see that the counting ratio also becomes smaller than that in 200 ns in the linear region. It means that a part of real coincidence events are lost under the timing window of less than 200 ns.

4.9.5 Angular resolution for various directions

Fig. 4.19 shows the comparison of the ARM distributions of the DOI and the non-DOI Compton cameras for a ^{137}Cs point source at the center of FOV, which are taken with the same acquisition time. From this result, we can confirm that the angular resolution of the DOI Compton camera is clearly improved compared to that of the non-DOI camera because of the effect of the DOI identification. The experimental evaluated angular resolution of the DOI camera was 8.8° (FWHM) at the center of FOV, whereas that of the non-DOI camera was around 14° (FWHM).

In addition, for the evaluation of the angular resolution in except the center of the FOV, we also measured the ARM distribution. The measured configuration was (1) (θ, ϕ)=(+45°, 0°), (2) (θ, ϕ)=(0°, 0°) (center of the FOV), and (3) (θ, ϕ)=(−45°, 0°). The intensity of the ^{137}Cs point source was 10 MBq and the distance to the source was 140 cm, where the corresponding radiation dose was around 0.5 μSv/h. The data acquisition time here was 1 min for each datum point. In the results, the angular resolutions at each point were (1) 7.9° (FWHM), (2) 8.8° (FWHM), and (3) 8.7° (FWHM), respectively. These results suggest that even in the positions except the center of FOV we can obtain the angular resolution of around 8° (FWHM). The imaging results of this experiment are described in section 4.10.

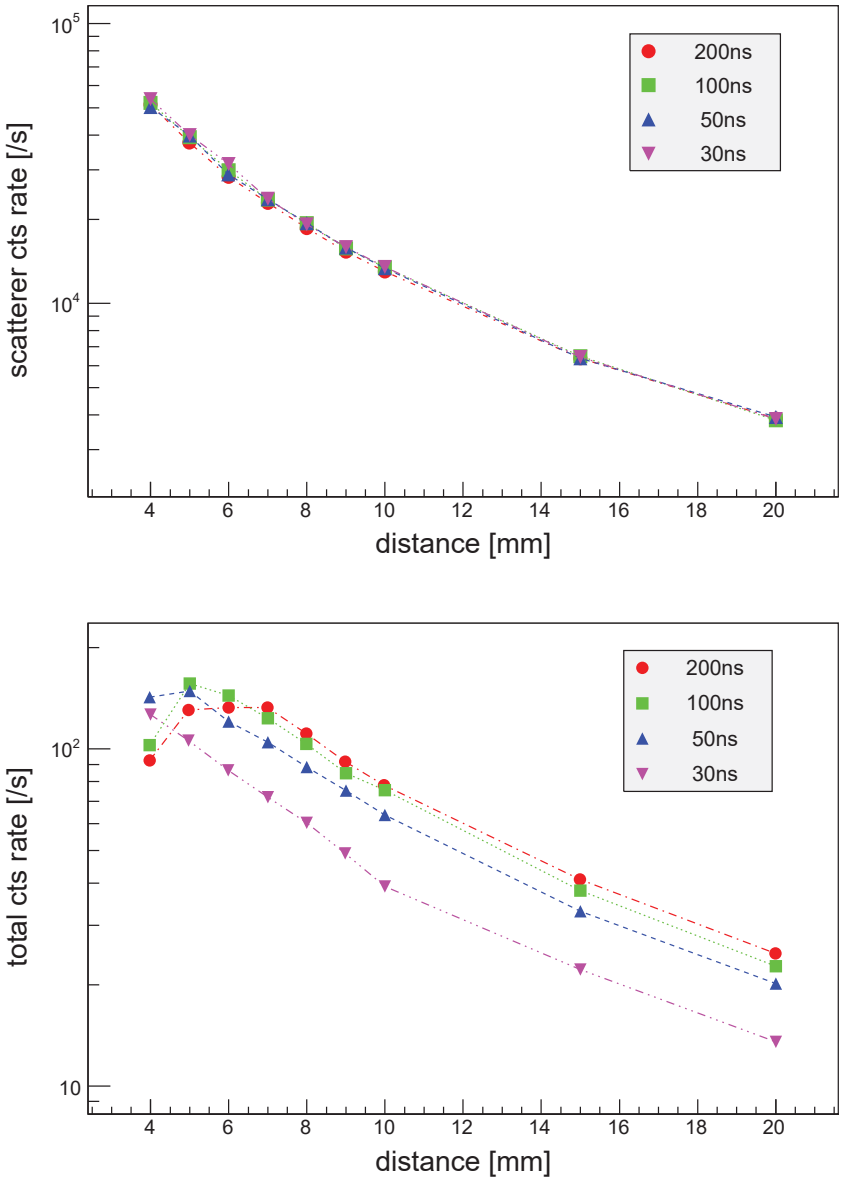

Figure 4.18: Counting rate performance of the DOI Compton camera (*top*) before taking timing coincidence and (*bottom*) after adapting timing coincidence and before the energy selection.

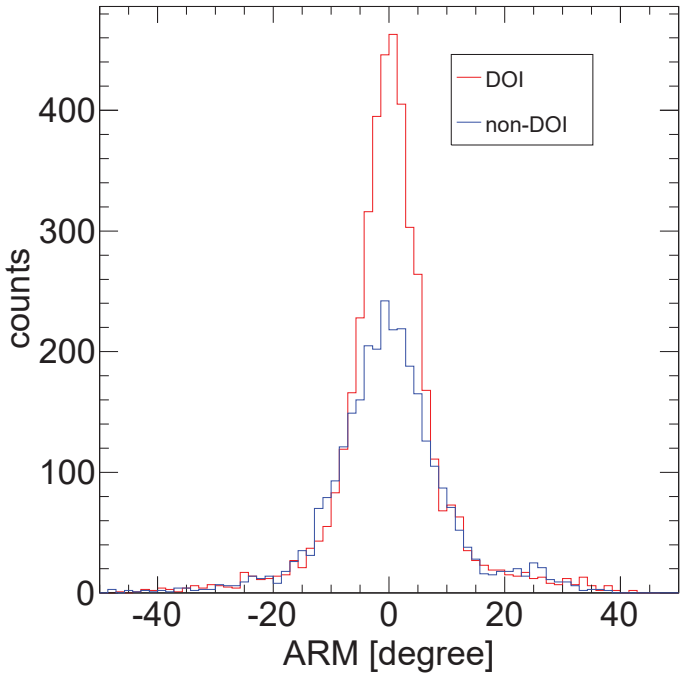

Figure 4.19: ARM distributions of the DOI and non-DOI Compton cameras at $\theta = 0°$.

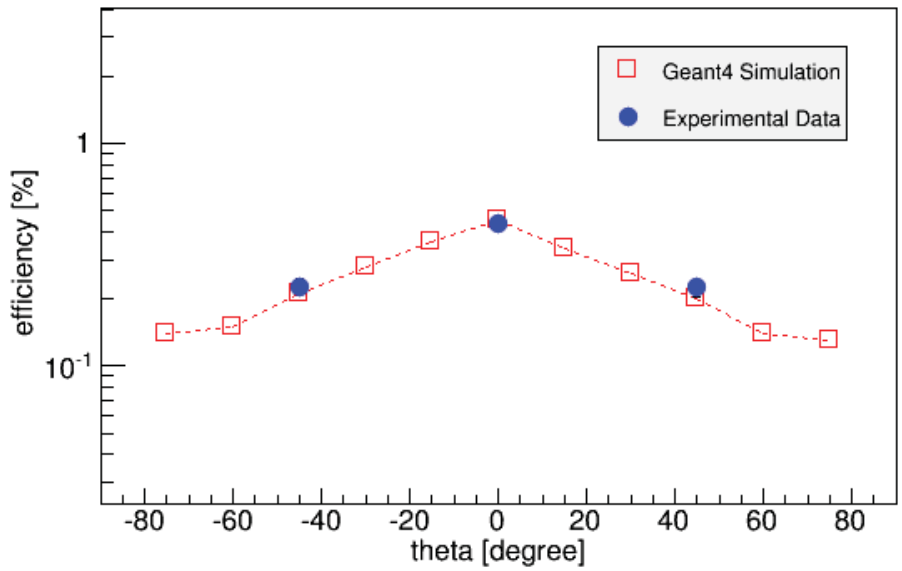

Figure 4.20: The simulated and experimental intrinsic efficiency of the DOI Compton camera as a function of source direction. The experimental efficiency was 0.43 ± 0.02 % at $\theta = 0°$.

4.9.6 Detection efficiency

Fig. 4.20 shows the evaluation results of intrinsic efficiency of the DOI Compton camera obtained by Geant4 simulation and a comparison to the representative experimental values of the experiment in section 4.9.5, as a function of source direction θ (at ϕ=0°). The experimental intrinsic efficiency is 0.43 ± 0.02% at the center of FOV (θ=0°), and 0.23 ± 0.02% at θ=±45°. The three experimental plots correspond the each value under the measurements which is described in section 4.9.5. These results are very consistent with the simulation.

The results of the detection efficiency is higher than other gamma cameras. Indeed, the detection efficiency of the DOI Compton camera is 0.71 cps/MBq at 1 m for 662 keV gamma rays, whereas that of the ASTROCAM is 0.16 cps/MBq, for example. This performance of high sensitivity provides a big advantage for the speedy measurements in the actual field in Fukushima.

4.10 Imaging performance

Before the field tests, we evaluated the imaging performance of the DOI Compton camera for various point sources. Fig. 4.21 shows the MLEM imaging results after 10 iterations in

Table 4.8: Energy cut regions for multi-source imaging.

Target energy [keV]	E_1+E_2 cut region [keV]	E_1 cut region [keV]
511	$461 \leq E_1+E_2 \leq 561$	$10 \leq E_1 \leq 150$
662	$612 \leq E_1+E_2 \leq 712$	$10 \leq E_1 \leq 165$
834	$784 \leq E_1+E_2 \leq 884$	$10 \leq E_1 \leq 170$

the experiment of a ^{137}Cs point source measurement described in section 4.9.5. From the results, we confirmed that the reconstructed images correctly identify each source position. Note that even in the short acquisition time of 1 min the DOI Compton camera can provide informative images. Although the necessary event statistics obviously depends on such as the distribution of the object, this result indicates preferable feature for the environmental measurement.

Next, we compared the images of the non-DOI and the DOI Compton camera in order to estimate the difference of the angular resolution not only by the FWHM of the ARM distribution as described in section 4.9.5 but also by the images. Fig. 4.22 shows the MLEM reconstructed images of two ^{137}Cs point sources with the image of optical fish-eye camera. The sources were separated by 10° each other, and the number of MLEM iteration was 10. Fig. 4.22 (*top*) and (*bottom*) are the images taken by the non-DOI camera and the DOI camera, respectively. As these figure shows, although in the image by the non-DOI camera the two sources are not separated, in the image by the DOI camera they are clearly resolved each other. These demonstration indicate that the DOI Compton camera actually can resolve two sources 10° apart, as estimated in section 4.9.5.

Then we conducted multi-energy source imaging in order to evaluate the imaging performance for various energy gamma rays. As shown in Fig. 4.23, we arranged three different point sources of ^{22}Na (511 keV), ^{137}Cs (662 keV), and ^{54}Mn (834 keV) at the same time. The distance to each source was all 50 cm and the measurement time here was 30 min. Fig. 4.24 shows the results of 1-D (*left*) and 2-D (*right*) energy spectrum. The three peaks of 511 keV, 662 keV, and 834 keV clearly resolved in the both results, hence by applying energy regions suitable for each energy peak we visualized each source. The energy cut conditions for each source are listed in table 4.8. Fig. 4.25 shows the SBP and MLEM after 10 iterations imaging results. We have confirmed that even for multiple energy sources the position of each source was correctly identified. On the other hand, on the images of 511 keV gamma ray there is significant artifact around the center of FOV. This is caused by the escape event which is mainly incoming from the ^{137}Cs source and accidentally meets the energy cut condition for 511 keV. The technique to remove the escape events is required and we will revisit this problem in section 6.5.5.

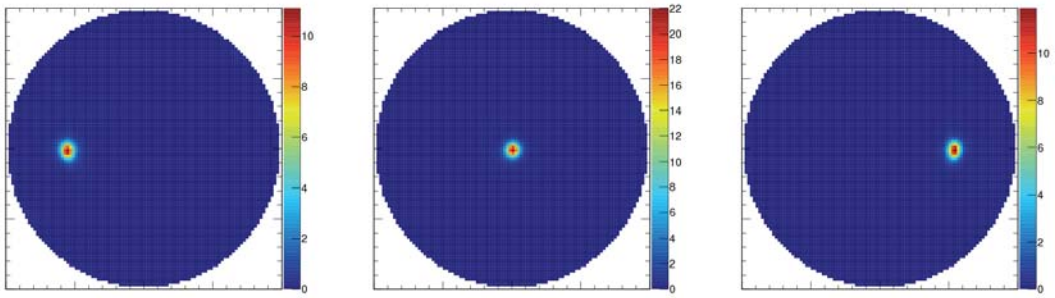

Figure 4.21: The MLEM imaging results taken by the DOI Compton camera under the following source configurations: $(left)$ (θ, ϕ)=(-45°, 0°), $(center)$ (θ, ϕ)=(0°, 0°), and $(right)$ (θ, ϕ)=(+45°, 0°).

4.11 Field tests in Fukushima

Based on these basic performance verifications, the DOI Compton camera has been tested several times in Namie, Fukushima. Fig. 4.26 (*top*) shows example images of field tests in July 2014 [90]. From Fig. 4.26 $(top, left)$, we can confirm that the dose of the ground in the forest was uniformly high. In addition, Fig. 4.26 $(top, right)$ indicates that the hotspot spreads along the path and that because of the concentration of deciduous leaf the dose level of the bush adjacent to the path becomes higher than that of other region. In this situation, the air dose rate at the camera position was $\sim$4 μSv/h, and the dose rate in the brightest hotspot corresponded to $\sim$10 μSv/h. Both images of Fig. 4.26 (*top*) were taken with an acquisition time of 3 min. The tendency implicated from the imaging results well matches the real dose distribution which was measured by a dosimeter afterwards.

Fig. 4.26 (*bottom*) shows the energy spectrum measured by the DOI Compton camera during the imaging shown in Fig. 4.26 $(top, right)$. Three photoelectric peaks clearly appear at 662 keV (^{137}Cs), 605 keV, and 796 keV (^{134}Cs). When imaging Fig. 4.26 (*top*), we selected only the events corresponding to ^{137}Cs by setting the energy region. By changing the used energy range, we can also obtain the distribution image of ^{134}Cs.

From these field tests, we have confirmed that by using the DOI Compton camera radiation hotspot images can be acquired in short time, even with strong background contamination of around 5 μSv/h.

4.12 Discussion

Through the results of basic performance evaluation, we demonstrated that the DOI Compton camera has practical angular resolution of 8° (FWHM) and high intrinsic ef-

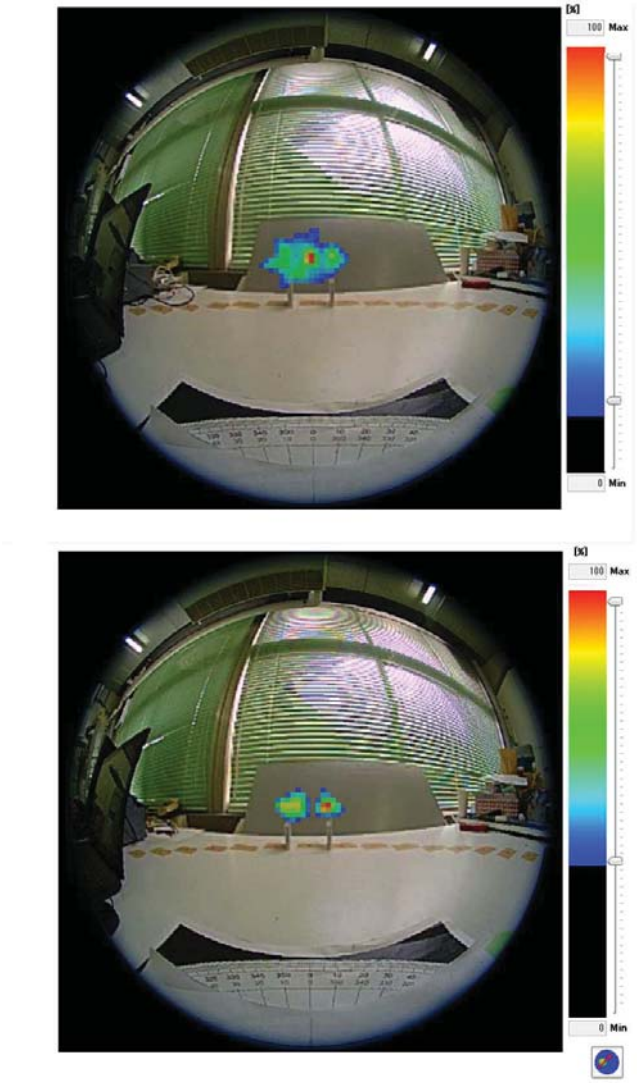

Figure 4.22: The MLEM imaging results of two ^{137}Cs point sources which are separated by an angle of 10° measured by the non-DOI Compton camera (*top*) and the DOI Compton camera (*bottom*).

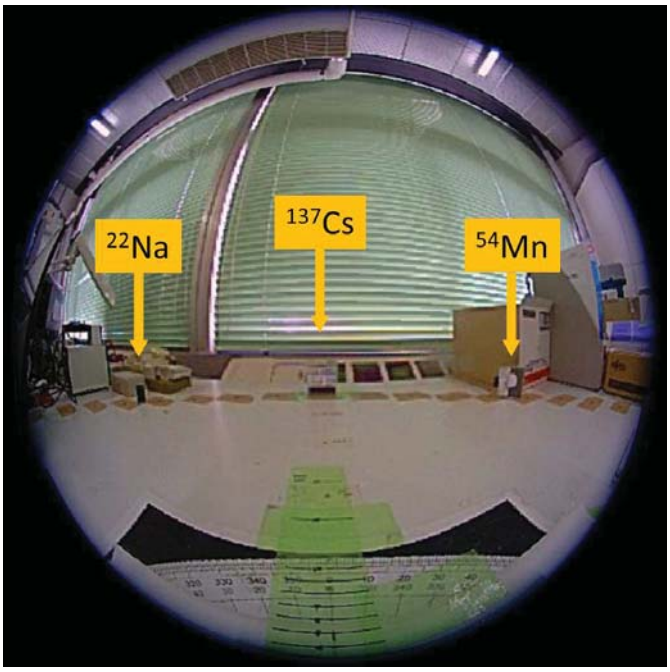

Figure 4.23: Source configuration of multiple sources measurement. ^{22}Na was located at (-45°, 0°), ^{137}Cs at (0°, 0°), and ^{54}Mn at (+45°, 0°).

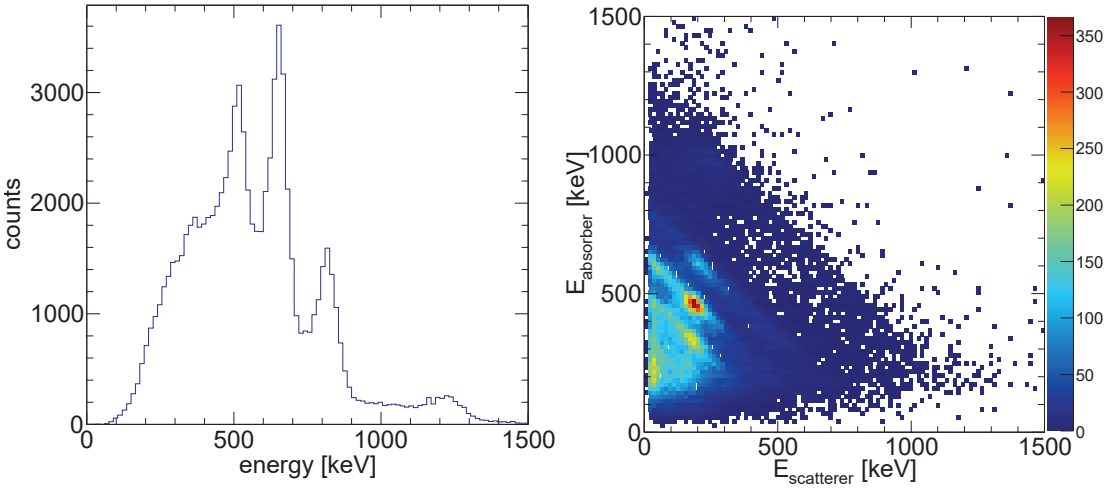

Figure 4.24: (*Left*) 1-D and (*right*) 2-D energy spectra after coincidence selection.

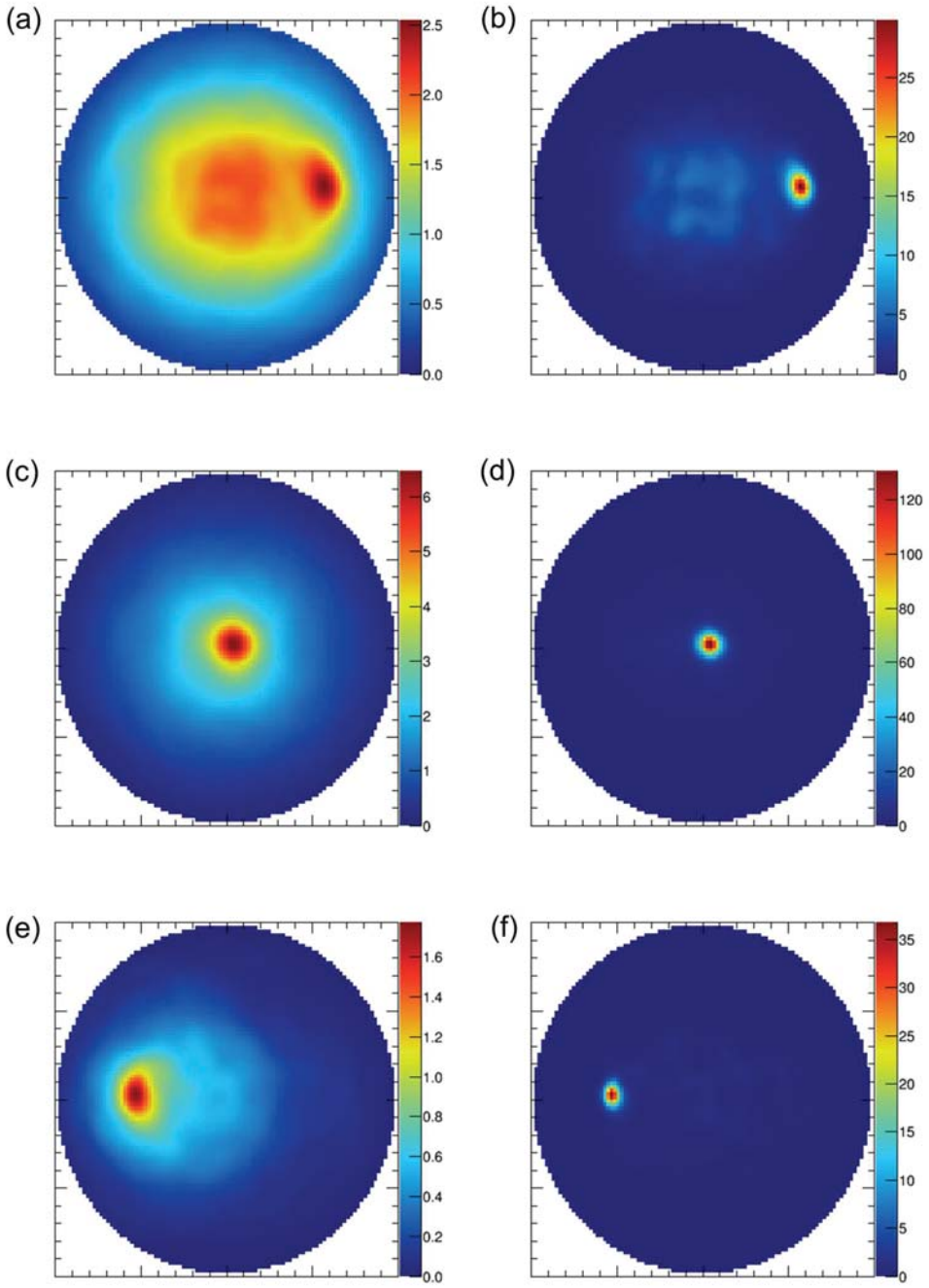

Figure 4.25: Results of multi sources imaging of (*a*) 511 keV (SBP), (*b*) 511 keV (MLEM), (*c*) 662 keV (SBP), (*d*) 662 keV (MLEM), (*e*) 834 keV (SBP), and (*f*) 834 keV (MLEM).

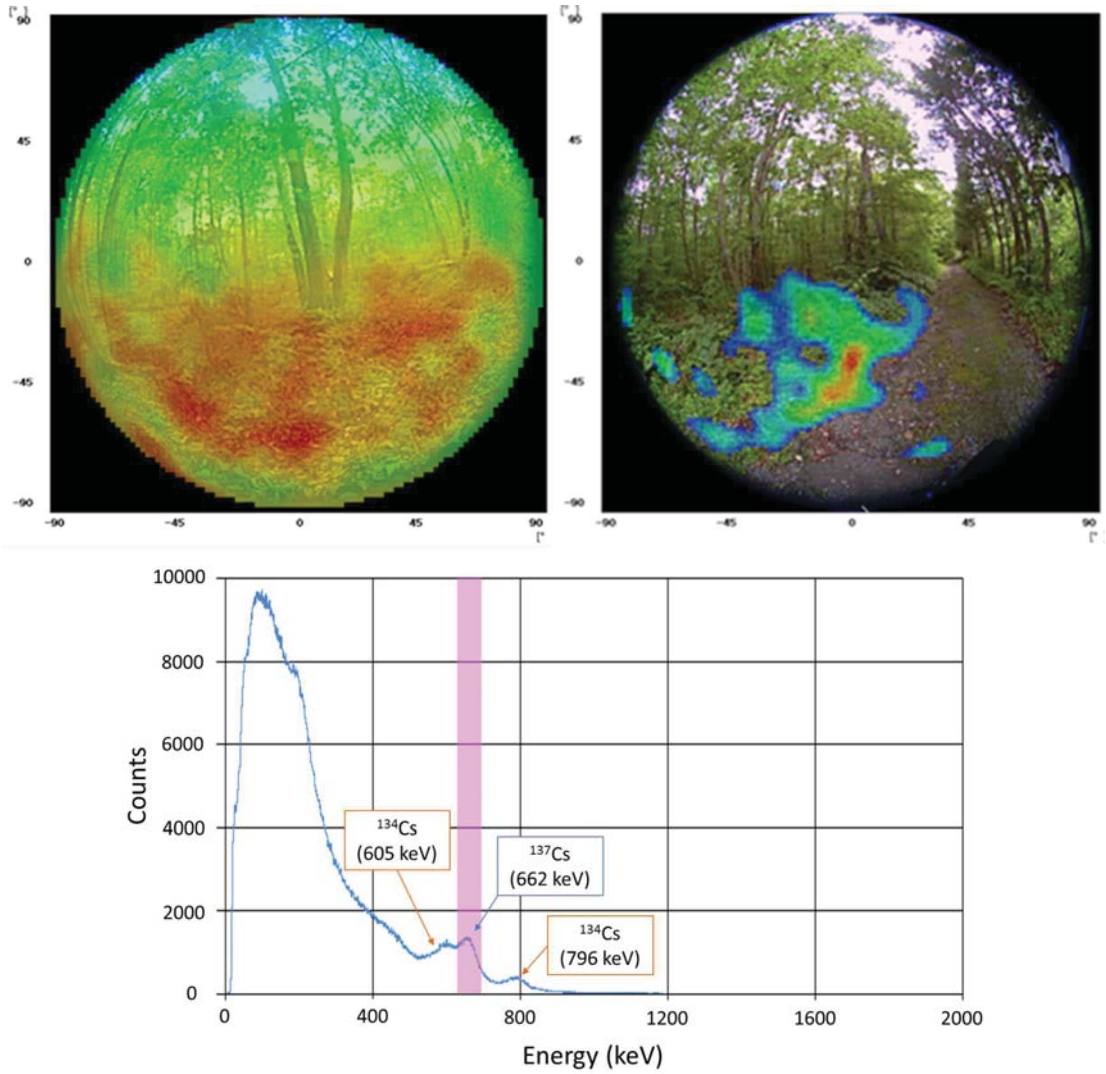

Figure 4.26: (*Top*) Examples of gamma-ray images measured in field test in Namie, Fukushima based on the DOI Compton camera in July 2014. (*Bottom*) The energy spectrum taken in the field test. The highlighted region denotes the energy utilized for reconstructing the images.

ficiency of over 0.4% for 662 keV gamma ray. Furthermore, in the field tests conducted in the forest at Namie, we confirmed that the camera can detect hotspot of 3−15 μSv/h in wide FOV typically with acquisition time of under 10 min. Compared to other imaging detectors aiming at environmental measurement, sensitivity is excellent although angular resolution is still modest. This high sensitivity feature makes it possible to provide almost real-time gamma-ray images in parallel with data acquisition. Note that, in terms of actual field investigation for hotspot identification, the responsive measurements are very advantageous. Furthermore, thanks to its light weight, our Compton camera can be easily mounted on a commercially available drone so that gamma-ray image over wide area can be taken from the air. This is especially important to survey on the forest and mountain in which ground-based survey is difficult.

On the other hand, there are still some challenging aspects for the Compton camera. In the case of insufficient statistics of the data, Compton camera has possibilities of providing false images. The appropriate amount of statistics largely depends on the source distribution, for example, it needs more large amount of measured data to obtain intricate distribution of the source. Hence it is challenging to estimate most appropriate measurement time for unknown measurement object, and the image reconstruction study in the case of low statistics should be conducted evermore.

Nevertheless, the DOI Compton camera provides beneficial information for wide area survey in short time. The achievement in this study is not restricted in the environmental measurement in Fukushima and is expected to be also applied in other field such as counterterrorism and national defense.

4.13 Chapter summary

In this chapter, we developed the DOI Compton camera for environmental measurement in Fukushima so as to promote efficient decontamination operation. In this development, we optimize the detector design by putting the highest priority on the portability and efficiencies for the prompt measurement in the field of Fukushima. The main results in this chapter are summarized as bellow:

- The DOI Compton camera achieved high detection efficiency of 0.71 cps/MBq at 1 m for 662 keV gamma rays thanks to adequate thick of Ce:GAGG scintillator.
- By utilizing the DOI identification method, the angular resolution was significantly improved. The typical angular resolution for 662 keV gamma ray is 8° (FWHM) at the center of FOV.
- The Compton camera features compact size (14 cm × 15 cm × 16 cm) and light in weight (2.5 kg).

- These features enable quick and flexible measurement in the real field, where radiation dose is mostly as low as $\sim$10 μSv/h level. Through the field tests in Namie, Fukushima, we confirmed that radiation hotspot can be identified within a few minutes even with background contamination.

In the following chapters, we try to develop the medical Compton camera for molecular imaging based on the technical know-how of developing this environmental Compton camera. In the medical use, not only high sensitivity but more precise measurement performance and better spatial resolution are required as compared to the environmental measurement use. Hence toward these improvement, in the chapter 5 we first extend the image reconstruction method to 3-D imaging, and then in the chapter 6 we report the specific development of the medical Compton camera and its imaging performances, which aims to achieve both high spatial resolution and high detection efficiency even with the compact detector.

Chapter 5

Three-dimensional image reconstruction

Although Compton imaging is usually conducted 2-dimensionally as described in section 4.8.1, various attempts to extend the reconstruction algorithm to 3-D imaging have also been reported [91, 50, 92, 93, 94]. For the use of medical imaging as described in chapter 6, we aim to obtain multi-color 3-D images covering wide energy range to maximize the advantage of a Compton camera. Hence, in this chapter, we describe how to reconstruct the 3-D imaging algorithm suited for small animal imaging, and demonstrate its imaging performances based on both simulation and experiments.

5.1 Extending MLEM algorithm to 3-D imaging

First, we extended the 2-D MLEM reconstruction algorithm in section 4.8.1 to the 3-D imaging space. In the 3-D MLEM reconstruction, the effect of the distance between the detector and each voxel in the imaging space becomes significant. Hence, we added this effect of distance to the system matrix t_{ij} when conducting the 3-D imaging. Fig. 5.1 shows schematic parameters used in the 3-D reconstruction. V_1, V_2, and θ denote the scattering position, the absorbing position, and the scattering angle, respectively. The system matrix t_{ij} is calculated voxel by voxel (V_j) over image region by considering the effect of solid angle of the target voxel, which is associated with the distance-to-voxel position, as follows;

$$t_{ij} = 2\pi\left(1 - \frac{|\overrightarrow{V_1 S}|}{\sqrt{|\overrightarrow{V_1 S}|^2 + a^2}}\right) \times \exp\left[-\frac{1}{2}\left(\frac{|\Theta_j| - |\theta_k|}{\sigma}\right)^2\right] \times \frac{1}{\sin\theta_k}, \tag{5.1}$$

where a denotes the half size of the imaging voxel, Θ_j denotes the angle between the direction of the concerned image voxel j and the Compton cone axis, θ_k denotes the

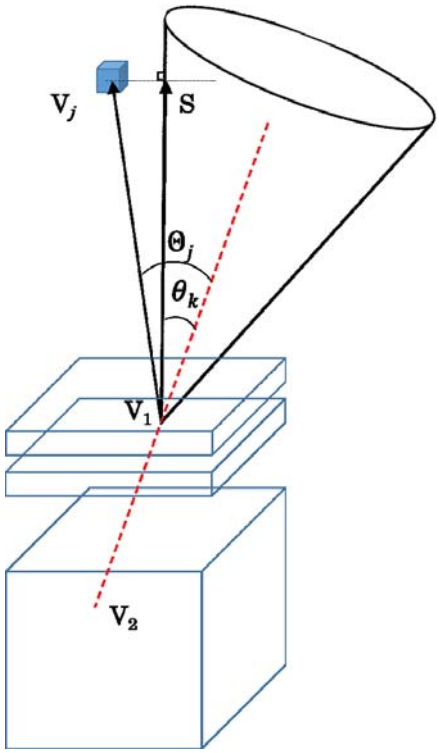

Figure 5.1: Diagram of the 3-D MLEM reconstruction.

scattering angle obtained by the energy information, and σ denotes the spatial resolution of the detector given by $\sigma = |\overrightarrow{V_1 S}| \tan(\Delta\theta)$, in which $\Delta\theta$ represents the intrinsic angular resolution. The first term of equation 5.2 represents the effect of solid angle of the image voxel seen from the camera, the second term represents a Gaussian distribution of the cone surface considering the angular resolution of the detector, and the final term is a weighting factor of each event.

Along with the extension of imaging space from 2-D to 3-D, the sensitivity map s_j also must be calculated 3-dimensionally. The s_j which represents the probability in the defined imaging region was determined based on the Geant4 as is the case of section 4.8.2. In this study, we assumed the imaging space of 80 mm × 80 mm × 80 mm from the detector surface. This size allows for small animal imaging measurement such as a mouse, from the vertical angle to its body axis. Fig. 5.2 shows schematic geometry definition of the sensitivity map. Under this configuration, Fig. 5.3 shows examples of 2-D profile slices of the 3-D sensitivity map which was obtained by the DOI Compton camera for 662 keV gamma ray: the image in the Z-X direction at Y = 0 mm (*left*) and that in the X-Y direction at Z = 0 mm (*right*), as shown in Fig. 5.2. In Fig. 5.3 (*left*), the probability around X = 0 mm is slightly low due to the gap of the scintillator array (see Fig. 4.5 for

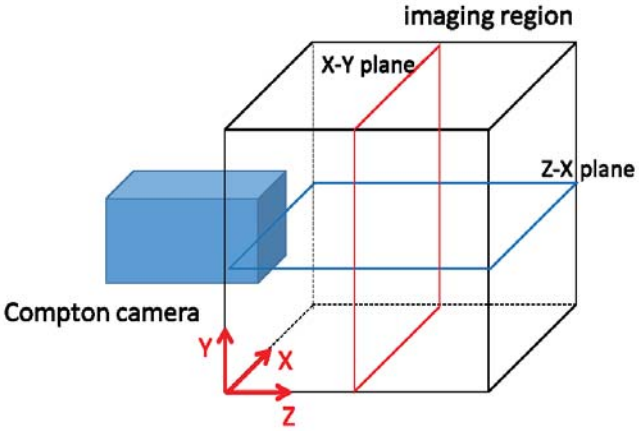

Figure 5.2: Schematic geometry of sensitivity map.

the configuration of the scintillator array).

5.2 Data acquisition method

While the above reconstruction by a Compton camera can provide a useful 3-D gamma-ray distribution, the spatial resolution in the vertical direction to the camera (Z direction in Fig. 5.2) tends to deteriorate due to the lack of diagonal intersecting data [95]. In order to compensate for the absence of this intersecting data, we propose a multi-angle data acquisition method. Fig. 5.4 shows an example of conventional imaging situation for a Compton camera, which we denote single-angle data acquisition method. On the other hand, Fig. 5.5 shows an example of configuration of the multi-angle method. In the multi-angle method, data is collected from multiple angles and then the image reconstruction is conducted by combining all these data together based on the following algorithm:

For data sets Ω_l, $l = 0, 1, ..., L-1$

$$\lambda_j^n = \frac{\lambda_j^{n-1}}{s_j^l} \sum_{i=1}^{N} \frac{t_{ij} v_i}{\sum_k t_{ik} \lambda_k^{n-1}}, \tag{5.2}$$

where L denotes the number of data acquisition angle. Hereafter in this section, we set the four data acquisition azimuthal angles of 0, 90, 180, and 270° ($L = 4$), considering symmetry to the imaging region. Single-angle data acquisition is equivalent to a measurement from 0°. In the multi-angle data acquisition, we rotate one Compton camera around the imaging region in stead of fabricating multiple Compton camera system.

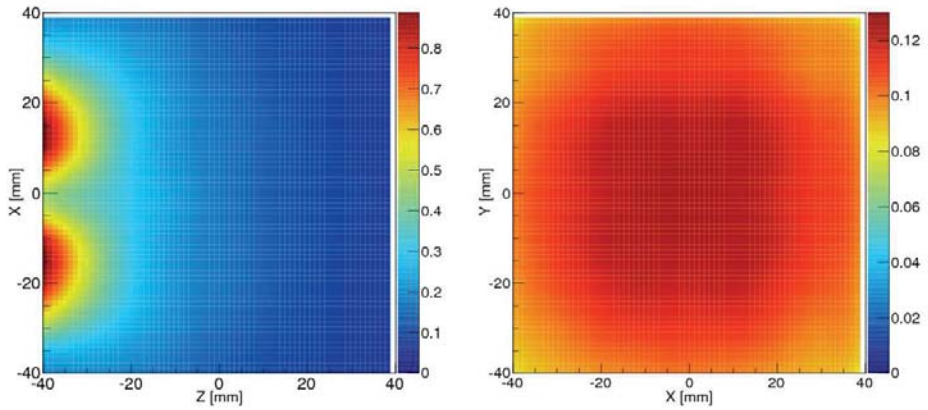

Figure 5.3: Resultant 3-D probability map of the DOI Compton camera for 662 keV gamma ray obtained by Geant4 simulation. 2-D slice in the Z-X direction at Y = 0 mm (*left*) and in the X-Y direction at Z = 0 mm (*right*).

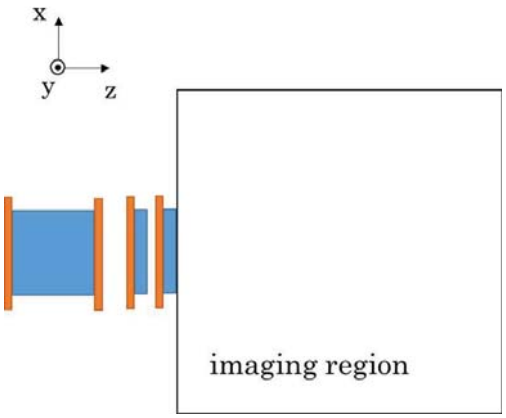

Figure 5.4: Configuration of the single-angle data acquisition measurement.

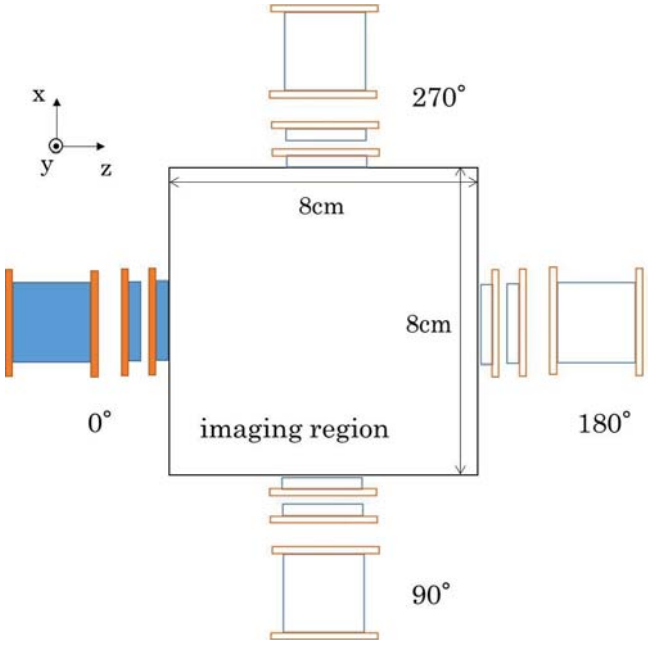

Figure 5.5: Configuration of the multi-angle data acquisition measurement.

5.3 Imaging performance

5.3.1 Simulation

Imaging response for a point source at the center of FOV

In order to confirm the accuracy of our 3-D MLEM reconstruction method, we first conducted performance tests in the case of the DOI Compton camera using Geant4 simulation.

For the single-angle configuration, we initially imaged a point source at the center of FOV. In the simulation the assumed source isotropically emits 662 keV gamma rays. The distance between the source and the first layer of the scatterer was 40 mm. Fig. 5.6 shows the MLEM imaging results after 15 iterations and Fig. 5.7 shows its 1-D profiles through the center of the source in each directions. Obviously, the source position on the reconstructed image correctly reflects the true position in all X, Y, and Z directions. The spatial resolutions calculated from the FWHM of each 1-D profile are 5.94 ± 0.06 mm, 5.69 ± 0.06 mm, and 11.1 ± 0.08 mm, in the X, Y, and Z directions, respectively. Note that, the spatial resolution in the Z direction is worse than that in other directions due to lack of diagonal intersecting data as described above. In fact, the angle of cone axis and its surface are restricted by the geometric configuration of the scatterer and the absorber, so that there exists few Compton cone which decreases the image uncertainty in the Z direction. As increasing the distance to the source, this effect becomes significant.

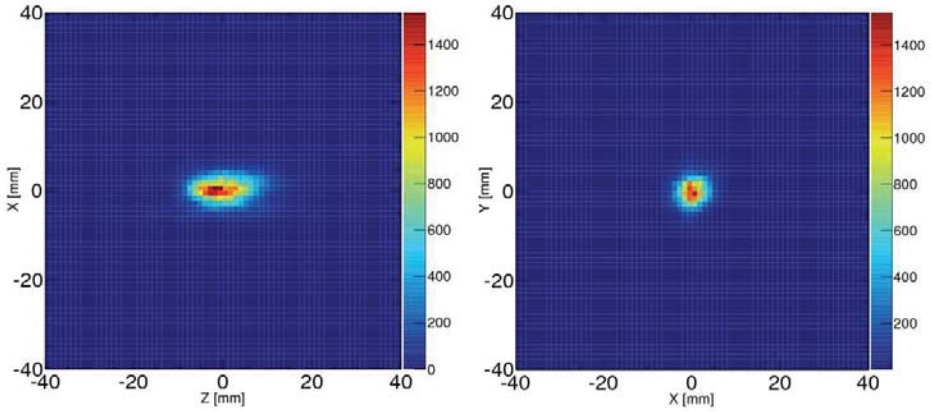

Figure 5.6: 3-D MLEM imaging result of the simulated single-angle data acquisition after 15 iterations. 2-D slice in the Z-X direction at Y=0 mm (*left*) and in the X-Y direction at Z=0 mm (*right*).

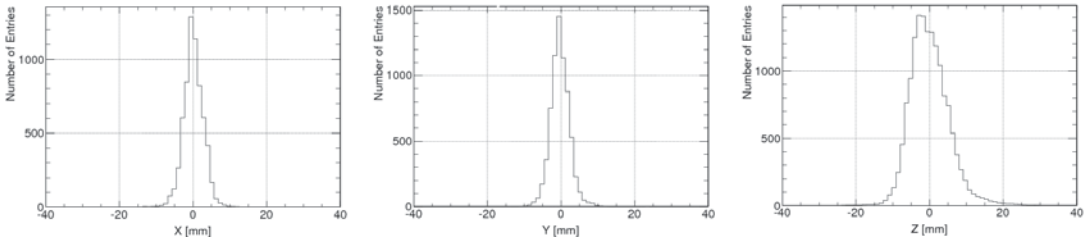

Figure 5.7: 1-D profiles corresponding to Fig. 5.6 in the X (*left*), Y (*center*), and Z (*right*) directions. The spatial resolutions in each direction measured from the FWHM of these profile are 5.94 ± 0.06 mm, 5.69 ± 0.06 mm, and 11.1 ± 0.08 mm, respectively.

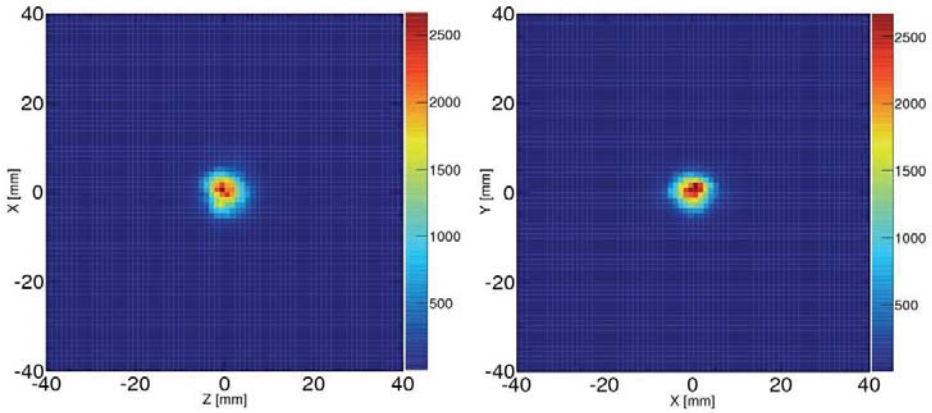

Figure 5.8: 3-D MLEM imaging result of the simulated multi-angle data acquisition after 15 iterations. 2-D slice in the Z-X direction at Y=0 mm (*left*) and in the X-Y direction at Z=0 mm (*right*).

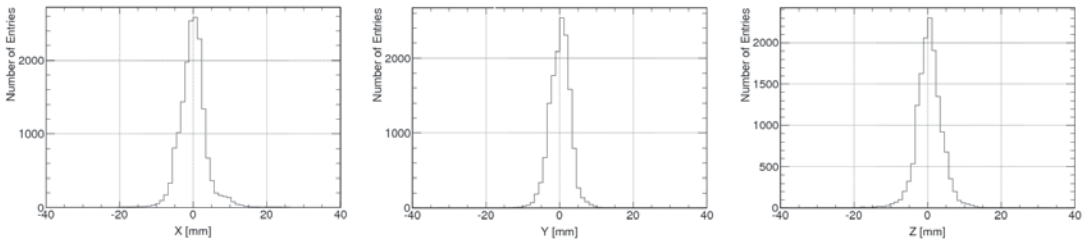

Figure 5.9: 1-D profiles corresponding to Fig. 5.8 in the X (*left*), Y (*center*), and Z (*right*) directions. The spatial resolutions in each direction measured from the FWHM of each profile are 6.27 ± 0.07 mm, 6.02 ± 0.05 mm, and 6.64 ± 0.07 mm, respectively.

Furthermore, in order to compare the multi-angle data acquisition with the single-angle method, next we conducted the multi-angle data acquisition imaging under the same condition as the single-angle method. The distance between the camera and a point source was also set to 40 mm. Fig. 5.8 and 5.9 show the imaging results of the multi-angle method. The results of spatial resolution in the X, Y, and Z directions are 6.27 ± 0.07 mm, 6.02 ± 0.05 mm, and 6.64 ± 0.07 mm, respectively. Compared to the single-angle situation, the resolution in the Z direction is largely improved and almost isotropic 3-D spatial resolution has been achieved at the center of the imaging region.

Table 5.1: Source positions for the image response measurements

	source	position (X, Y, Z) [mm]
Pattern 1	source 1	(0, 0, 0)
	source 2	(15, 0, 0)
	source 3	(30, 0, 0)
Pattern 2	source 1	(0, 0, 0)
	source 2	(15, -15, 0)
	source 3	(30, -30, 0)
Pattern 3	source 1	(0, 0, 0)
	source 2	(0, 15, 0)
	source 3	(0, 30, 0)

Evaluation of the positional dependence of image response

We have confirmed that the 3-D MLEM reconstruction method proposed in this study is viable at the center of the defined imaging space. Thus in the next, we evaluate the image response at various positions in the imaging space based on the multi-angle method. On Geant4 simulation, we also assumed three point sources of 662 keV gamma ray. In order to study the positional dependence of the image response, we conducted image reconstruction tests of three patterns under different source arrangement. Table 5.1 lists the source configurations of each pattern. We assumed that the intensities of three sources were equivalent each other. Similar to the previous evaluation, the data acquisition azimuthal angles were taken as 0, 90, 180, and 270°.

Fig. 5.10, 5.11, and 5.12 show the results of the 3-D MLEM image after 15 iterations on pattern 1, 2, and 3, respectively. The *left* figures show the 3-D images, in which the voxels in which the voxels over one-fourth of the maximum value are described, and the *right* figures show the 1-D profiles in the X or Y direction through the center of the sources. Note that all the reconstructed images correctly reflected the true source positions in all patterns. These results suggest that 3-D MLEM reconstruction method in this study successfully operate over the imaging region, not limited to the center of FOV. Table 5.2 lists the results of spatial resolution. In the pattern 1 and pattern 2, the resolution of the reconstructed image gradually improves as increasing the distance from the center of (X, Y, Z)=(0 mm, 0 mm, 0 mm). This is mainly because in principle the spatial resolution of a Compton camera is increasing with the distance from the detector [95]. Thus, the resolution at the center of FOV tends to be worse than remaining positions where distance from the Compton camera becomes smaller, at least in one observing angle of 0, 90, 180, and 270°.

Table 5.2: Spatial resolutions of as measured for pattens 1−3

	source	resolution [mm]
Pattern 1	source 1	6.14±0.06
	source 2	5.91±0.06
	source 3	5.15±0.04
Pattern 2	source 1	6.36±0.10
	source 2	5.56±0.04
	source 3	4.69±0.03
Pattern 3	source 1	6.24±0.07
	source 2	6.02±0.05
	source 3	5.77±0.06

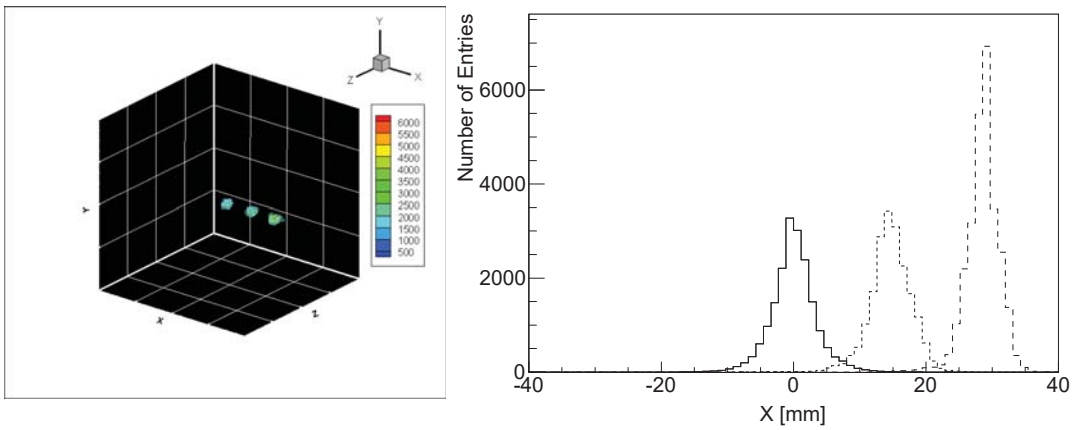

Figure 5.10: (*Left*) 3-D MLEM imaging result in the pattern 1. (*Right*) 1-D profiles through the centers of the source in the X direction. The spatial resolutions of each source are 6.14 ± 0.06 mm (X = 0 mm), 5.91 ± 0.06 mm (X = 15 mm), and 5.15 ± 0.04 mm (X = 30 mm).

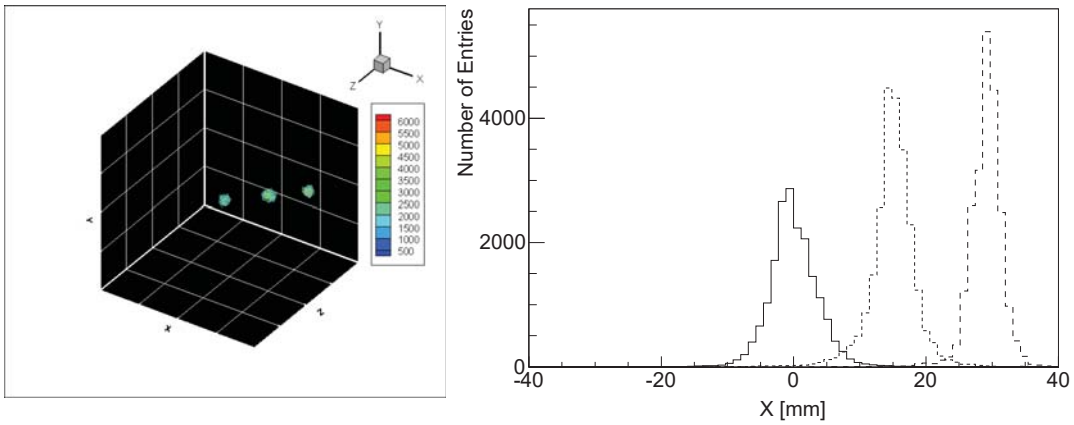

Figure 5.11: (*Left*) 3-D MLEM imaging result in the pattern 2. (*Right*) 1-D profiles through the centers of the source in the X direction. The spatial resolutions of each source are 6.36 ± 0.10 mm (X = 0 mm), 5.56 ± 0.04 mm (X = 15 mm), and 4.69 ± 0.03 mm (X = 30 mm).

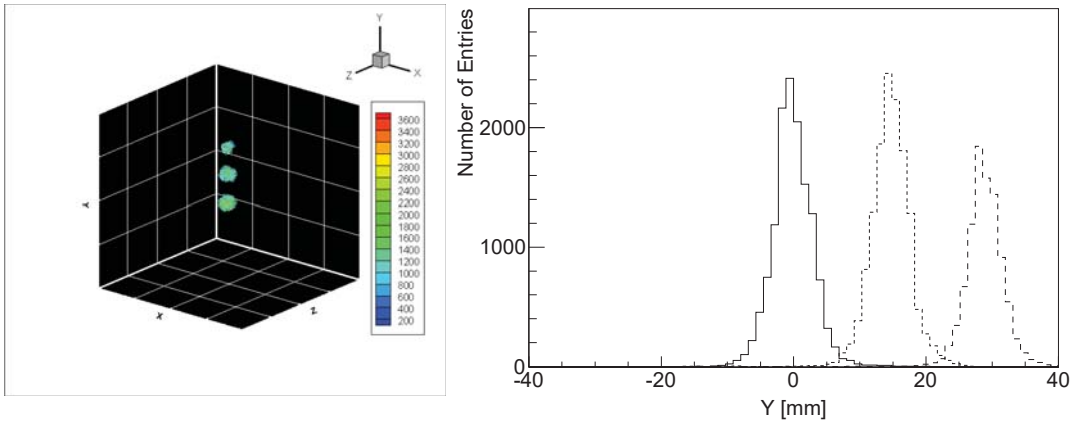

Figure 5.12: (*Left*) 3-D MLEM imaging result in the pattern 3. (*Right*) 1-D profiles through the centers of the source in the Y direction. The spatial resolutions of each source are 6.24 ± 0.07 mm (Y = 0 mm), 6.02 ± 0.05 mm (Y = 15 mm), and 5.77 ± 0.06 mm (Y = 30 mm).

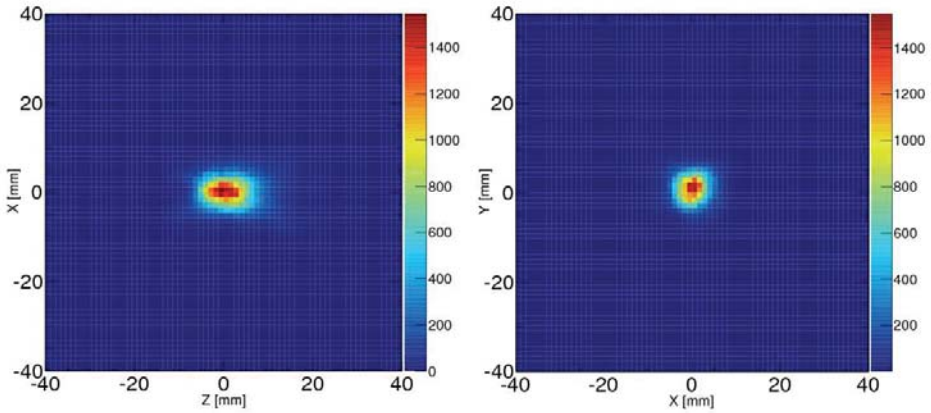

Figure 5.13: 3-D MLEM imaging result of the experimental single-angle measurement after 15 iterations. 2-D slice in the Z-X direction at Y=0 mm (*left*) and in the X-Y direction at Z=0 mm (*right*).

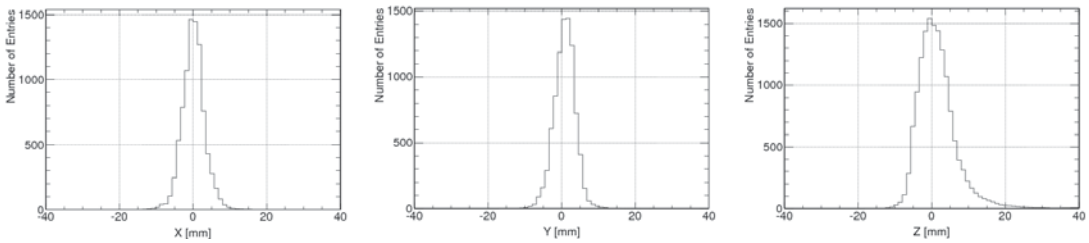

Figure 5.14: 1-D profiles corresponding to Fig. 5.13 in the X (*left*), Y (*center*), and Z (*right*) directions. The spatial resolutions in each direction measured from the FWHM of each profile are 6.24 ± 0.07 mm, 6.47 ± 0.08 mm, and 10.0 ± 0.10 mm, respectively.

5.3.2 Experiment

Imaging response for a point source at the center of FOV

To compare with the simulation as described above, we experimentally demonstrate imaging of ^{137}Cs point source using the DOI Compton camera. Firstly, we conducted an imaging test based on single-angle method under the same configuration as the simulation. We used a 1 MBq ^{137}Cs point source and set it in the center of the FOV at a distance of 40 mm from the detector. The measurement time was 120 sec. Fig. 5.13 shows the MLEM imaging results after 15 iterations, and Fig. 5.14 shows its 1-D profiles through the center of the three directions. Note that the reconstructed source positions are also consistent with the true positions. The experimental spatial resolutions obtained by the FWHM of 1-D profile in the X, Y, and Z directions are 6.24 ± 0.07 mm, 6.47 ± 0.08 mm,

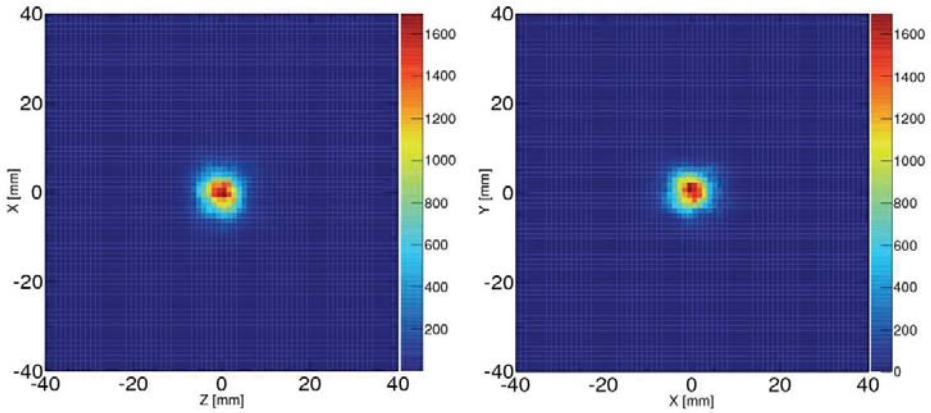

Figure 5.15: 3-D MLEM imaging result of the experimental multi-angle measurement after 15 iterations. 2-D slice in the Z-X direction at Y=0 mm (*left*) and in the X-Y direction at Z=0 mm (*right*).

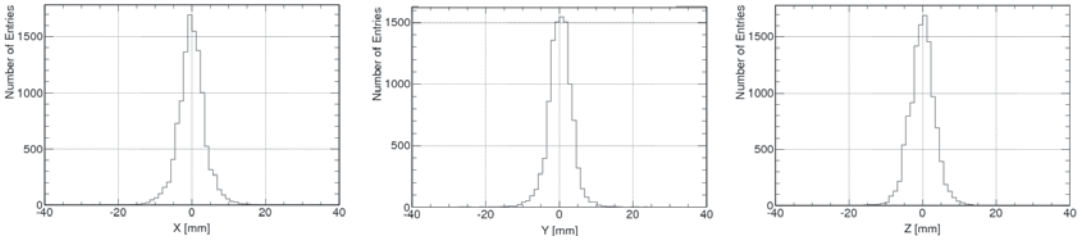

Figure 5.16: 1-D profiles corresponding to Fig. 5.15 in the X (*left*), Y (*center*), and Z (*right*) directions. The spatial resolutions in each direction measured from the FWHM of each profile are 6.81 ± 0.13 mm, 6.52 ± 0.07 mm, and 6.71 ± 0.11 mm, respectively.

and 10.0 ± 0.10 mm, respectively.

Similarly, we tried multi-angle data acquisition based on a point source. The data acquisition azimuthal angles were also taken as 0, 90, 180, and 270°. A ^{137}Cs point source was located at the distance of 40 mm from the detector and the measurement time in each data acquisition angle was 30 sec (total 120 sec). Fig. 5.15 shows the MLEM imaging results after 15 iterations, and Fig. 5.16 shows its line profiles through the center of the three directions. The results of spatial resolution measured from the FWHM of each 1-D profile in the X, Y, and Z directions are 6.81 ± 0.13 mm, 6.52 ± 0.07 mm, and 6.71 ± 0.11 mm, respectively. From these results, we confirmed that the multi-angle data acquisition measurement actually improves the spatial resolution in the Z direction as expected from simulation.

In summary, we have established a 3-D imaging reconstruction method based on mea-

surements from four azimuthal angles. However in the medical imaging, more sophisticated analysis and optimization will be required since a subject of imaging is not a point source but spatially extended. Moreover, quantitativity of reconstructed image is a key factor for medical imaging. Hence, we further optimize the 3-D imaging reconstruction based on the multi-angle method in section 6.4.

Chapter 6

Compton camera for medical imaging

6.1 Introduction

Considering all advantages as described in previous chapters, Compton cameras can be an innovative detector for not only environmental measurement but in the medical imaging. In the nuclear medicine, the use of Compton camera makes it possible to obtain various biological information which had never been obtained with SPECT and PET. For example, diagnosis such as observing graft survival and discriminating cancer and inflammation is possible by utilizing the information. Furthermore, extending the type of available RI tracer has potential to reduce the cost of producing the tracer, which is conventionally made by a cyclotron facility in each medical center. Hence, Compton camera is a promising detector to open a new era in the medical imaging.

As described section 2.2.3, although various Compton cameras have been studied for the molecular imaging application, these have not been achieved to practical use. The difficulties of existing Compton cameras are that (1) the required measurement time becomes too large because of low detection efficiency, and (2) the image reconstruction method is still at an early stage of development as compared with that of PET or SPECT due to its complexity. In this study, we try to develop a Compton camera for nuclear medicine imaging which resolves these problems based on various technical know-hows of the DOI Compton camera for environmental measurement. One of the primary goals of developing the medical Compton camera is to obtain a multi-color, that means multi-energy source in wide energy range, 3-D image by using the Compton camera. In this chapter, we describe the development for the medical Compton camera and investigation of its imaging performances.

6.2 Development of medical Compton camera

6.2.1 Study for improving the angular resolution

Although the DOI Compton camera showed high sensitivity, its angular resolution of around 8° (FWHM) is insufficient for medical use, as this angular resolution is equal to the spatial resolution of around 14 mm (FWHM) at a distance of 10 cm from the detector. The spatial resolutions of other conventional modalities such as SPECT and PET in clinical use are around 5−10 mm (see Fig. 2.5), so that the resolution of Compton camera is also needed to be improved for achieving as well or better performance. Therefore we consider that improving the angular resolution should be one of the primary factor for developing the medical Compton camera. Fig. 6.1 (*top*) shows the angular resolution of the DOI Compton camera divided by source factors: the factor of position uncertainty, energy uncertainty, and Doppler broadening effect. These resolution are calculated on the Geant4 simulation in order to estimate each contribution. In the case of the DOI Compton camera, the position uncertainty is the dominant factor at the energy of 662 keV. Thus optimizing detector geometry should improve the image resolution most effectively, for example, by reducing scintillator pixel size and changing the distance between the scatterer and the absorber, it is expected to improve the resolution most efficiently. Fig. 6.2 shows a new geometry design for the medical Compton camera constructed on the Geant4 simulation. Fig. 6.1 (*bottom*) shows the expected angular resolution in the case of the assumed detector design for medical Compton camera. By reducing the pixel size of the scatterer to 0.5 mm and by setting the distance between the scatterer and the absorber to 50 mm, the angular resolution is expected to significantly improve by nearly twice.

6.2.2 Design of medical Compton camera

Based on the simulation results described above, actual detector design is fixed as shown in Table 6.1. In the medical Compton camera, the whole 2-dimensional detector scale is one-quarter of that of the DOI Compton camera thus improving flexibility of multi-angle data acquisition. In order to improve the resolution the pixel size of the scatterer is reduced to 0.5 mm × 0.5 mm × 3.0 mm. The scintillator pixels both in the scatterer and the absorber were divided by 0.1−0.12 mm thick $BaSO_4$ in X-Y directions

Fig. 6.3 shows the photograph of the medical Compton camera system. The camera consists of a sensor head, which includes scintillator arrays and MPPC arrays, and signal processing boards. Since a volume of the detector was reduced to one-quarter scale, the total system weights only 580 g. One of the key changes is that we separate the sensor head from signal processing unit. This makes the sensor head more compact, and flexible measurements become possible. Another unique feature of the camera design is that the performance such as the resolution, efficiency, and FOV can be changed, depending on

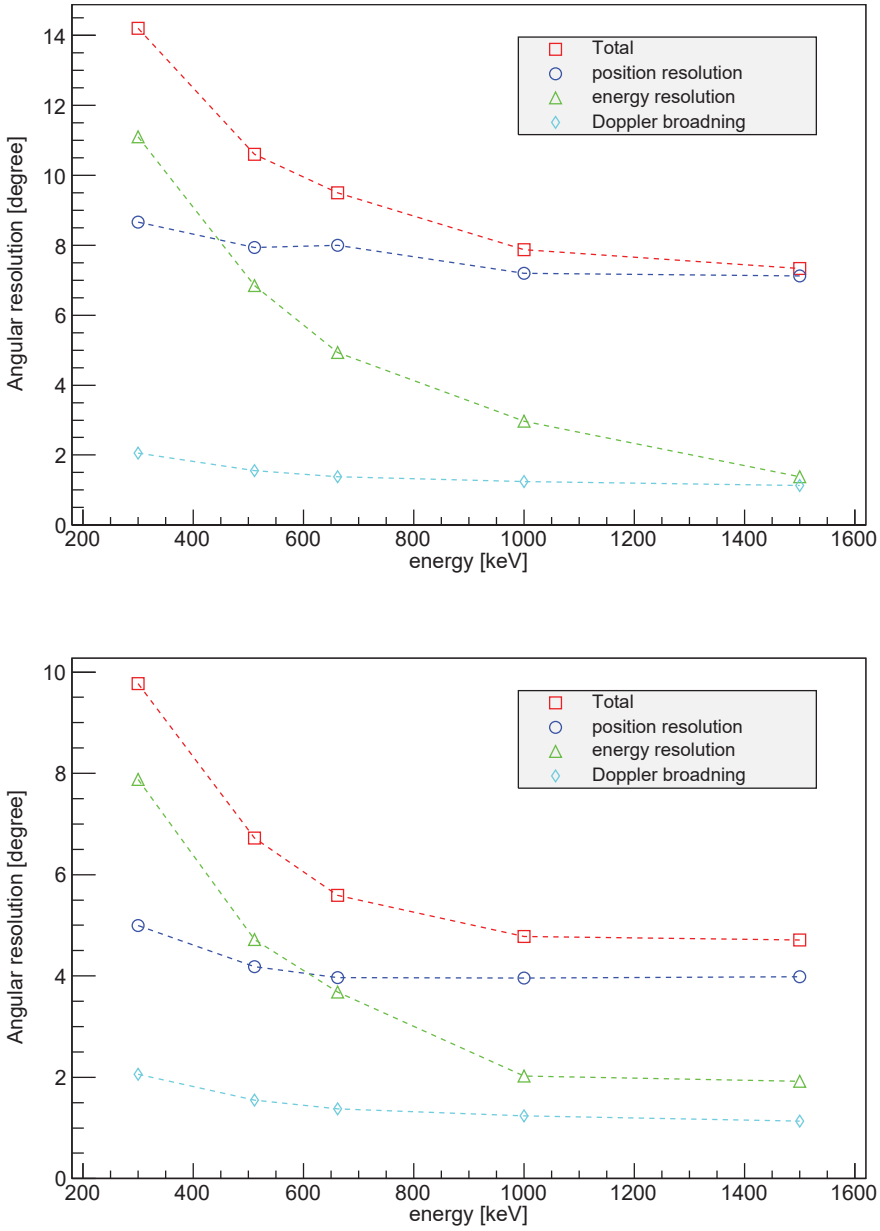

Figure 6.1: Angular resolution of (*top*) the DOI Compton camera and (*bottom*) the simulated medical Compton camera differentiated by each of the components.

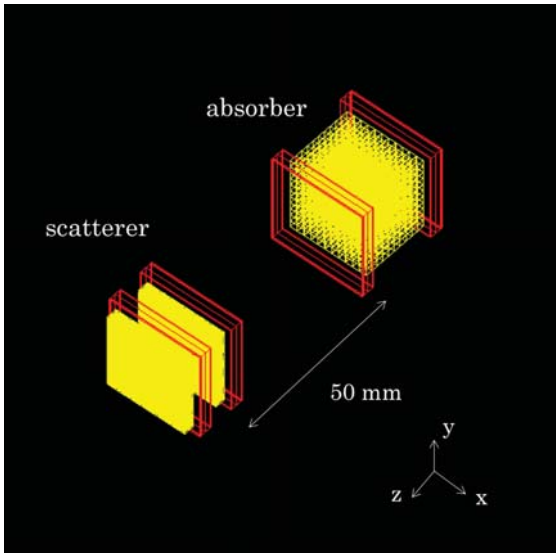

Figure 6.2: Configuration of the medical Compton camera on Geant4 simulation.

Table 6.1: Scintillator configuration in the medical Compton camera.

Parameter	Value
SCATTERER	
Crystal dimensions	$0.5\,\mathrm{mm} \times 0.5\,\mathrm{mm} \times 3.0\,\mathrm{mm}$
Array	42×42 arrays, 1 set
Layer	2 layer
ABSORBER	
Crystal dimensions	$2.0\,\mathrm{mm} \times 2.0\,\mathrm{mm} \times 2.0\,\mathrm{mm}$
Array	$11 \times 11 \times 10$ arrays, 1 set
Layer	10 layer
DISTANCE	$20-70\,\mathrm{mm}$ (variable)

various measurement situations, by adjusting the distance between the scatterer and the absorber.

To readout scintillator light outputs, we use 8×8 large monolithic MPPC arrays which is shown in Fig. 6.3 both in the scatterer and the absorber. Compared to the MPPC arrays used in the DOI Compton camera, these arrays have less dead space between the channels. The signals from 4-MPPC arrays (i.e. 4×4 ch) can be fed into a signal processing board. The basic readout system and the stream of event selection are the same as those of the DOI Compton camera.

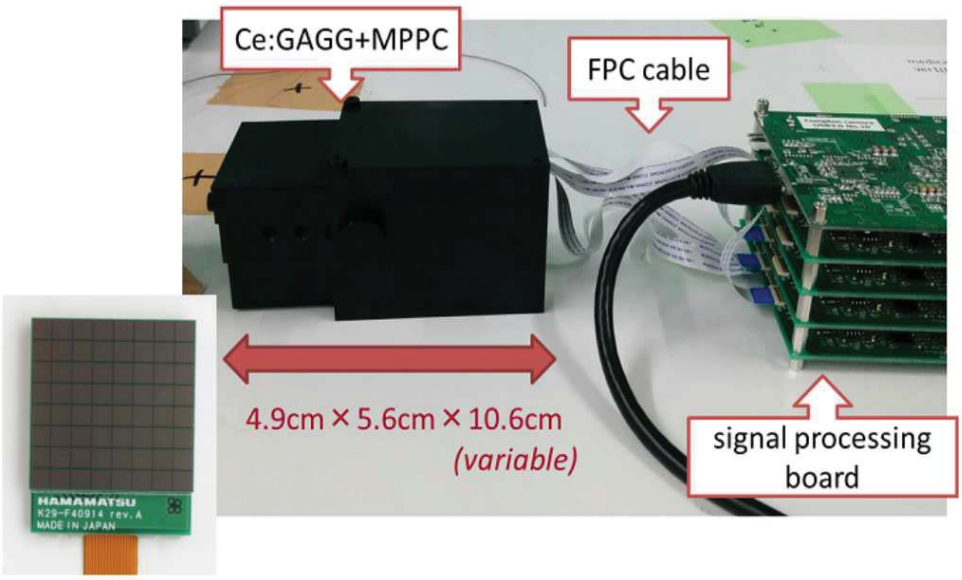

Figure 6.3: Detector configuration of the medical Compton camera.

6.3 Detector performance

6.3.1 Position response of the scintillator

First, the position map of the scatterer scintillator pixels of 0.5 mm was evaluated by using ^{137}Cs point source. Fig. 6.4 shows the position response of the scatterer in the first layer. It can be confirmed that each pixel is distinguished in almost all region except for peripheralis part. Thus we used 38×38 pixels after the removal of this degenerate region for the scatterer. Fig. 6.4 (*bottom*) shows the 1-D profiles in X and Y directions. The peak-to-valley ratios in these directions were 5.8±0.5 and 6.0±0.4, respectively.

On the other hand, Fig. 6.5 shows the position response of the 3-D scintillator array used for the absorber as measured by ^{137}Cs source. Fig. 6.5 (*top*) shows a representative 2-D slice of the 3-D array, and Fig. 6.5 (*bottom*) shows the profiles with pixels in the center row in X, Y, and Z directions. The results of peak-to-valley ratio evaluation in each direction were 6.6±0.4 (X), 5.3±0.1 (Y), and 10.6±1.7 (Z). These results indicate that the absorber also has adequate capability of pixel identification.

6.3.2 Energy response

Fig. 6.6 (*top*) and (*bottom*) show the energy spectra and scatter plot of photons measured in the scatterer and the absorber for ^{137}Cs point source at 25°C. The averaged energy resolutions in the scatterer and the absorber were 7.5% and 6.4% (FWHM), respectively. The energy resolution of the scatterer is slightly worse than that of the absorber because

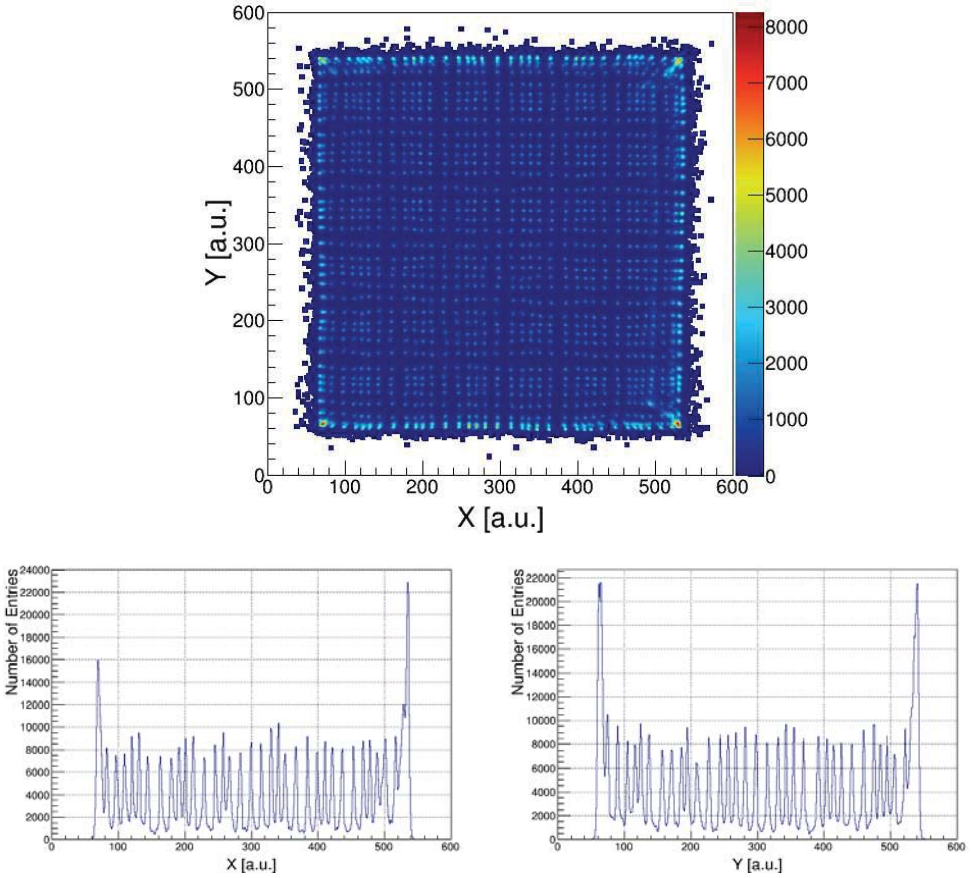

Figure 6.4: The position response of the scintillators in the scatterer for more than 10 keV energy deposit. (*Top*) The 2-D segment map and (*bottom*) the 1-D profiles in X and Y directions.

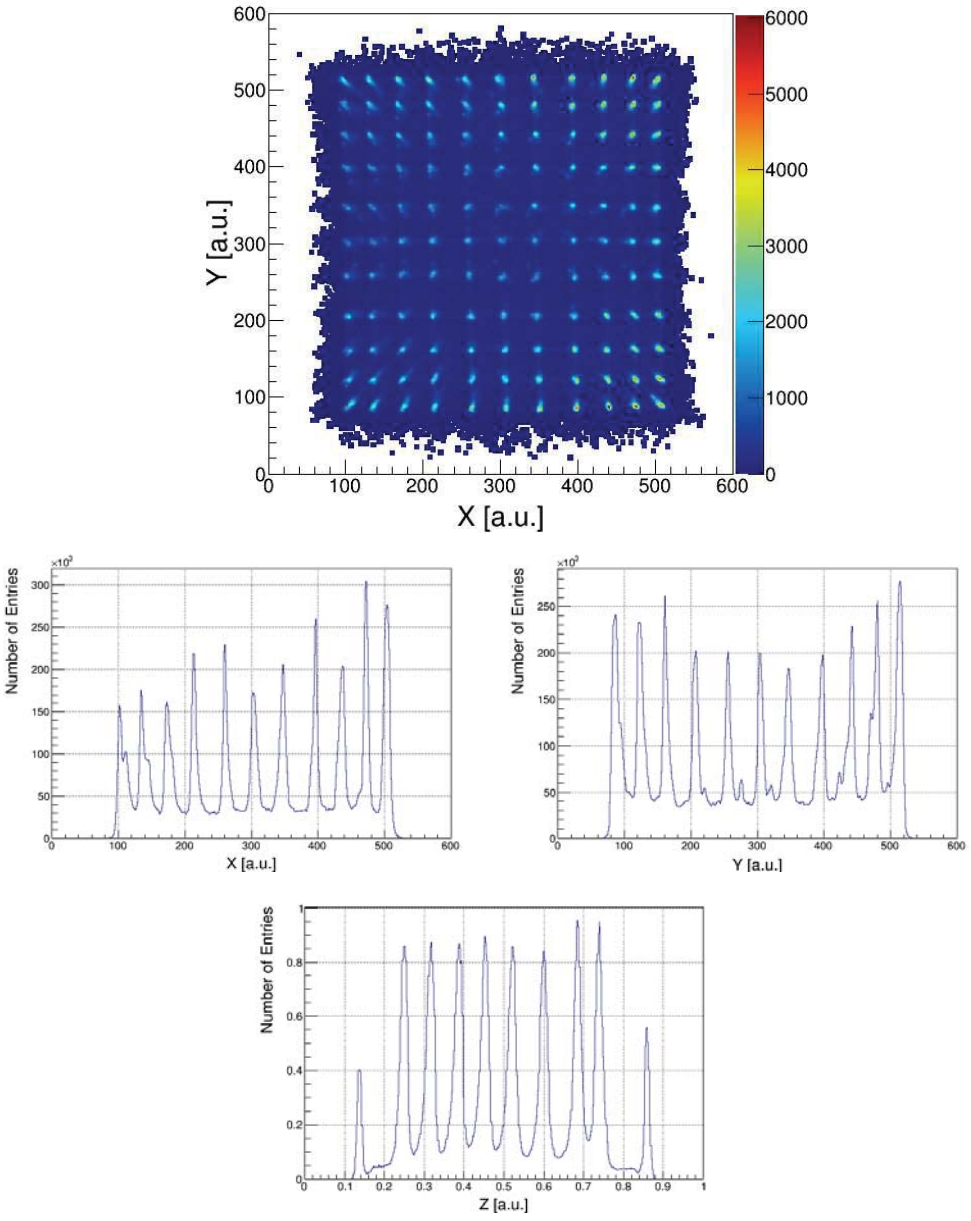

Figure 6.5: The position response of the scintillators in the absorber for more than 10 keV energy deposit. (*Top*) The 2-D segment map and (*bottom*) the 1-D profiles in X, Y, and Z directions.

Table 6.2: Energy cut conditions for the medical Compton camera.

Target energy [keV]	E_1+E_2 cut region [keV]	E_1 cut region [keV]
364	$328 \leq E_1+E_2 \leq 400$	$10 \leq E_1 \leq 120$, $190 \leq E_1 \leq 120$
511	$461 \leq E_1+E_2 \leq 561$	$10 \leq E_1 \leq 130$, $200 \leq E_1 \leq 250$
662	$612 \leq E_1+E_2 \leq 712$	$10 \leq E_1 \leq 150$, $220 \leq E_1 \leq 400$
834	$784 \leq E_1+E_2 \leq 884$	$10 \leq E_1 \leq 150$, $220 \leq E_1 \leq 550$
1116	$1047 \leq E_1+E_2 \leq 1185$	$10 \leq E_1 \leq 165$, $235 \leq E_1 \leq 700$

of light loss by reflection boundary which is more significant in the fine-pixel scintillator. Furthermore, Fig. 6.7 shows the temperature dependence of the energy resolution in each detector. The resolution in both the scatterer and the absorber becomes better with the decreasing the temperature because the amount of luminescence of Ce:GAGG increase at low temperature [96, 97].

In the medical Compton camera the distance between the scatterer and the absorber is larger compared to the DOI camera, so that scattering angle of each Compton event is more restricted geometrically. This inevitably resulted in the narrow FOV and the low detection efficiency. In order to compensate this restriction and ensure the practicable FOV, we apply a new energy cut range for the event selection in the medical Compton camera. As shown in the 2-D scatter plot for 662 keV gamma rays in Fig. 6.6 (*bottom*), the back-scattering events is concentrated at around $E_1 \sim 200$ keV under the detector configuration of the medical Compton camera. In order to utilize as many effective events as possible while at the same time to reject these back-scattering events, we set the double energy range for E_1. We determined the E_1 energy range ($E_a \leq E_1 \leq E_b$, $E_c \leq E_1 \leq E_d$) as below. The E_a is for cutting the circuit noise, so that we set to 10 keV as is the case with the DOI Compton camera regardless of the energy of incident gamma rays. The E_d is determined as adequately covering the range of scattering angle. The E_b and E_c are applied to reject the back-scattering events. Obviously, there is a trade-off between the number of appropriate event (N_{right}) and the signal-to-noise ratio (S/N). In fact, the wider energy range may contain larger number of events while the signal-to-noise ratio is degraded. Therefore, we optimized the E_b and E_c so that product of of N_{right} and S/N becomes maximum. In the Geant4 simulation, we irradiated 662 keV gamma rays from the center of FOV. Fig. 6.8 shows the result of the product $N_{right} \times S/N$ in the energy range of $10\,\text{keV} \leq E_1 \leq E_b$ as a function of E_b. As the figure shows, this value takes maximum at $E_b = 150$ keV. Hence, in the same way the optimized double energy range E_1 for 662 keV conclusively became $10\,\text{keV} \leq E_1 \leq 150\,\text{keV}$, $220\,\text{keV} \leq E_1 \leq 400\,\text{keV}$. Table 6.2 lists the energy cut ranges for various energy gamma rays from 364 keV to 1116 keV, which are applied to multi-energy imaging described in the following sections.

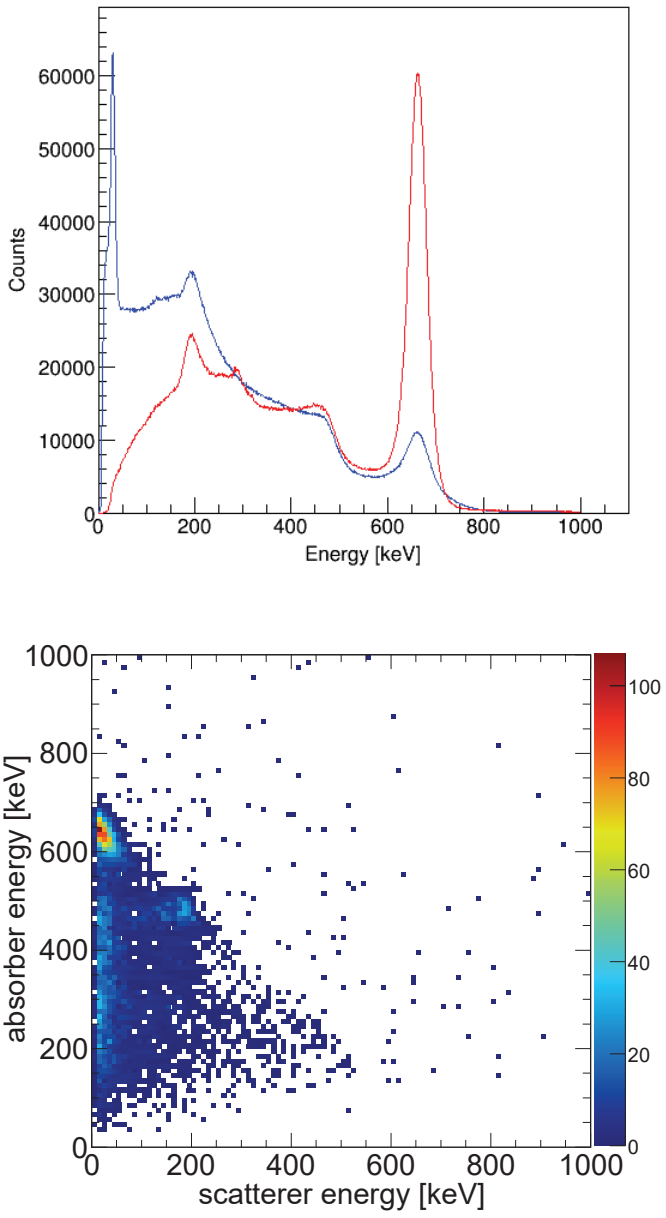

Figure 6.6: Energy spectra of the medical Compton camera. (*Top*) the 1-D energy spectrum for 662 keV gamma rays. The blue and red lines indicate the response of the scatterer and the absorber, respectively. (*Bottom*) the 2-D scatter plot for 662 keV gamma rays.

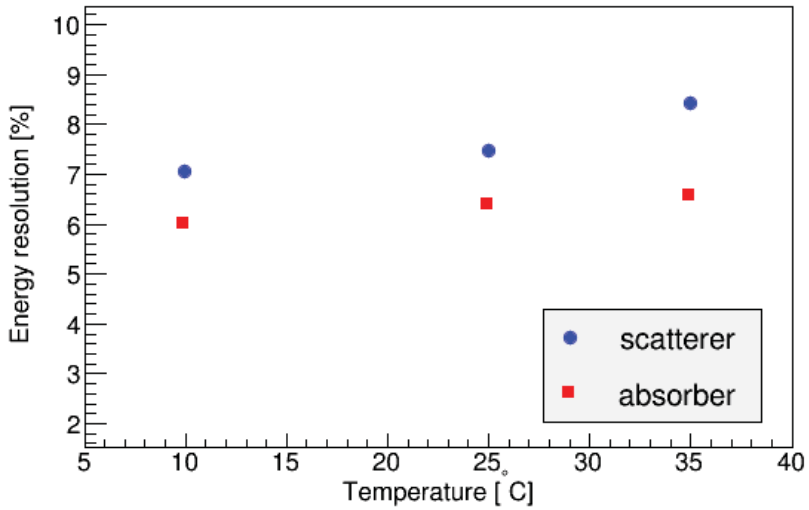

Figure 6.7: Temperature dependence of energy resolution.

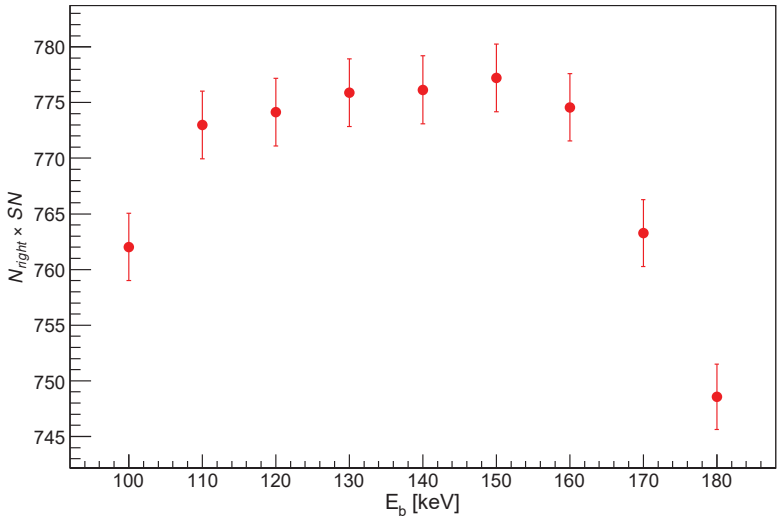

Figure 6.8: Product of the number of appropriate event and the signal to noise ratio $N_{right} \times S/N$ as a function of E_b.

6.3.3 Evaluation of image resolution

Fig. 6.9 shows the ARM distribution of the medical Compton camera for 662 keV gamma rays, compared to that of the DOI Compton camera. The distance between the scatterer and the absorber is 50 mm in this experiment. From Fig. 6.9, it is clear that the resolution of the medical camera is significantly improved. The angular resolution of the medical Compton camera for 662 keV gamma ray is 4.2° (FWHM) at the center of FOV. Although in the DOI Compton camera for environmental measurement, the image resolution has been evaluated based on the angular resolution, in the field of medical imaging the resolution is often represented by the spatial resolution, which depends on the distance to the source. Hence, we also conducted the evaluation based on the spatial resolution in this chapter. In general, the smaller the distance to the imaging object is, the better the spatial resolution of a Compton camera becomes even under the same angular resolution. Therefore it is preferred to measure the data as close as possible to the imaging object in terms of the spatial resolution. Fig. 6.10 shows the MLEM imaging result of measurement of a ^{137}Cs point source at a distance of 40 mm from the camera, which assumes small animal imaging. The iteration number of this image is 10. The spatial resolution, which is measured by the FWHM of the profile in the X direction, became 3.1 mm (FWHM). Although the spatial resolution is slightly worse because of the source distribution, this result is almost consistent with the result of the angular resolution of 4.2°.

Fig. 6.11 shows the experimental and simulation results of the angular resolution for 662 keV gamma rays as a function of the distance between the scatterer and the absorber. In addition, Fig. 6.12 shows the energy dependence of the angular resolution as measured with the distance between the scatterer and the absorber of 50 mm. In the experimental measurements, we used ^{133}Ba (for 364 keV), ^{22}Na (for 511 keV), ^{137}Cs (for 662 keV), ^{54}Mn (for 834 keV), and ^{60}Co (for 1173 keV). The Geant4 simulation takes the energy resolution based on the actual measurement value described in section 6.3.2. These simulation results well agree with the experimental results.

6.3.4 Detection efficiency

Fig. 6.13 shows the measured detection efficiency of the medical Compton camera for 662 keV gamma rays as a function of the distance between the scatterer and the absorber, as compared with simulation results. The detection efficiency is represented by the intrinsic efficiency $\varepsilon_{\mathrm{int}}$ as described in section 3.2.2. On the other hand, Fig. 6.14 shows the energy dependence of the intrinsic efficiency at the distance between the scatterer and the absorber of 50 mm. The typical intrinsic efficiency for 662 keV is 0.06%. In the experiments, the measurement condition such as the used isotopes, and the energy cut ranges were same as the case of the angular resolution evaluation described in section 6.3.3.

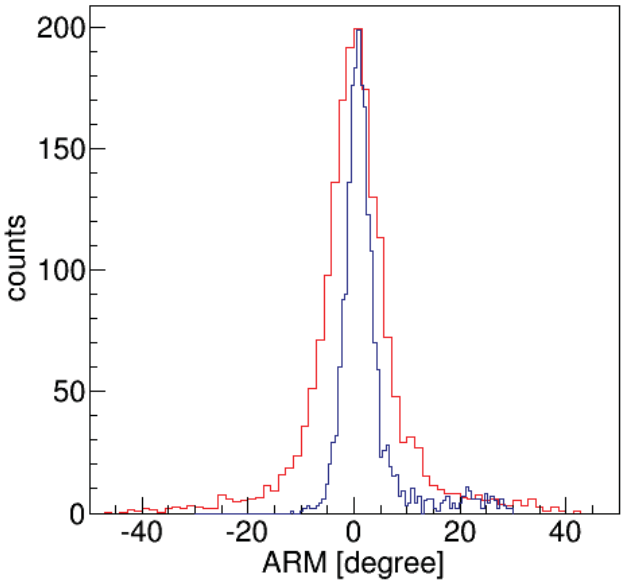

Figure 6.9: ARM distribution of the medical Compton camera (*blue*) compared with that of the DOI Compton camera (*red*). The distance between the scatterer and the absorber was 50 mm.

In Fig. 6.14, the measured efficiencies of 511 keV and 1173 keV become higher than that of simulation results. This is because in Geant4 simulation, we irradiated only single energy gamma rays of the concerned energy, however, in the experiments ^{22}Na and ^{60}Co practically emit several energy gamma rays and escape events from the higher energy gamma rays (1275 keV gamma rays for ^{22}Na and 1333 keV gamma rays for ^{60}Co) were contaminated.

Compared with the DOI Compton camera, the intrinsic efficiency of the medical Compton camera is reduced to a sixth part. This is mainly due to longer distance between the scatterer and the absorber. Furthermore, the reduction of the absolute efficiency of the medical camera becomes definitely twentieth part of that of the DOI camera, together with smaller detector size. In spite of these reduction, the medical Compton camera has almost equivalent sensitivity to the Ge-detector based Compton camera (GREI-II) thanks to high photo-detection efficiency of Ce:GAGG. In addition, although it is trade-off between the sensitivity and the resolution, by changing the detector distance the detection efficiency can be further improved up to approximately 4 times.

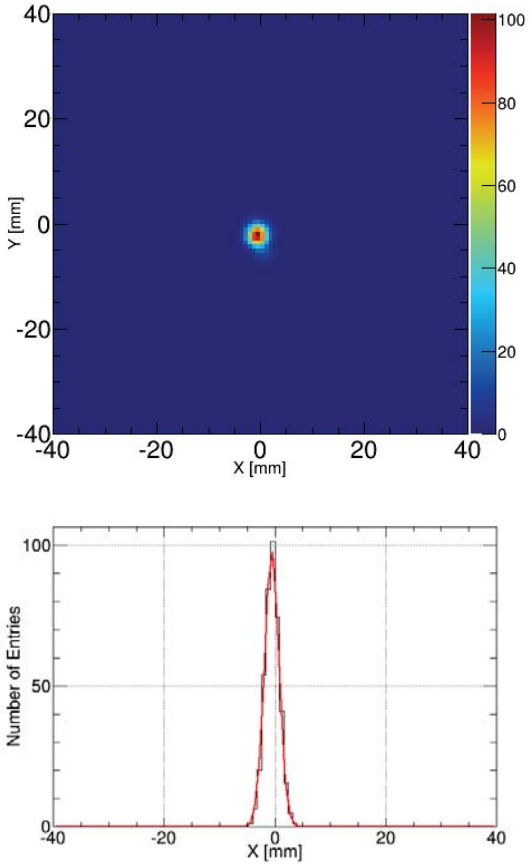

Figure 6.10: The evaluation of the spatial resolution at a distance of 40 mm using a ^{137}Cs point source. (*Left*) MLEM imaging result after 10 iteration, and (*right*) its profile in X direction.

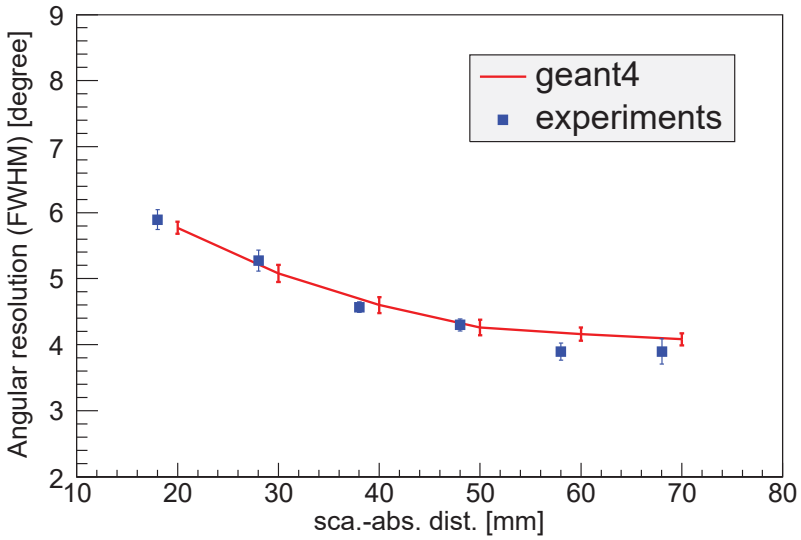

Figure 6.11: Angular resolution of the medical Compton camera for 662 keV gamma rays.

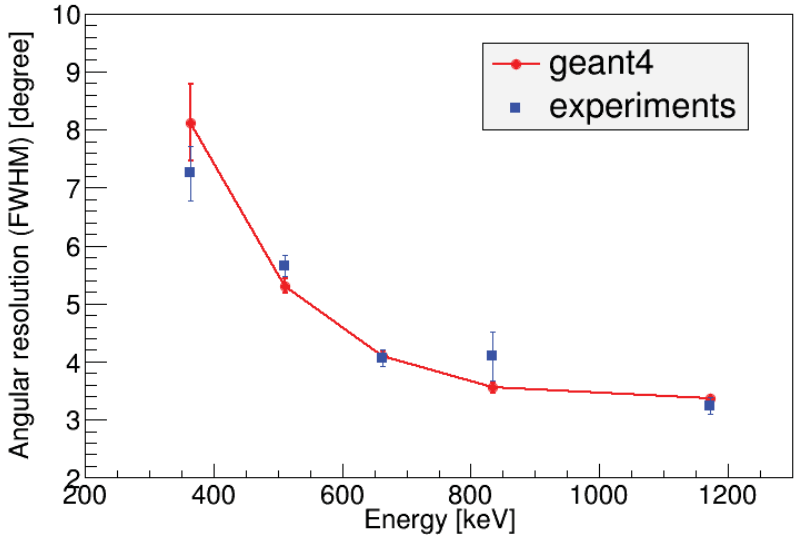

Figure 6.12: Angular resolution of the medical Compton camera at the distance between the scatterer and the absorber of 50 mm.

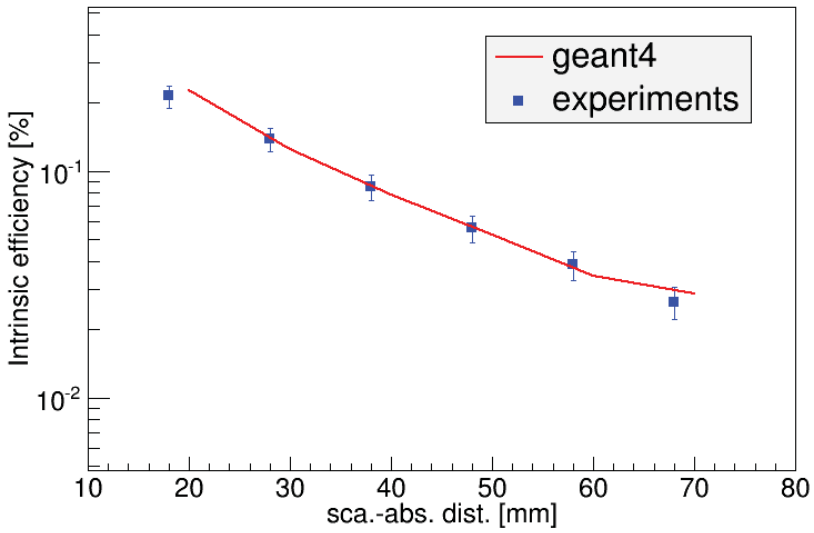

Figure 6.13: Detection efficiency of the medical Compton camera for 662 keV gamma rays.

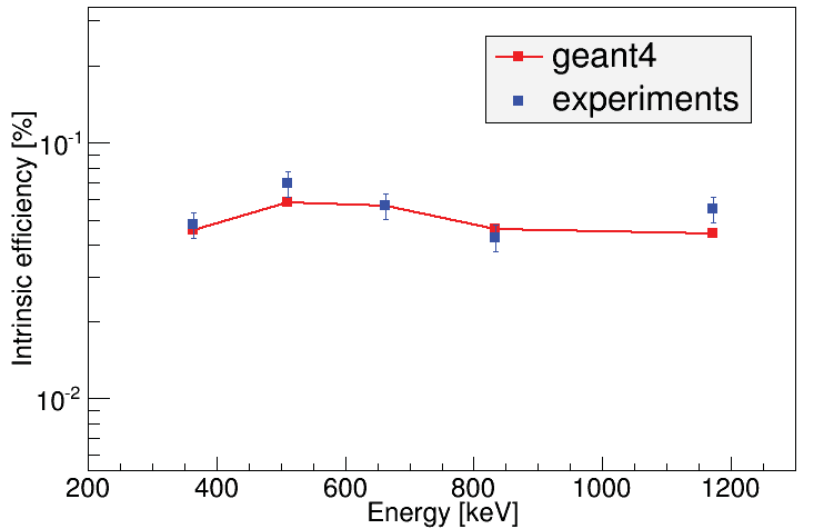

Figure 6.14: Detection efficiency of the medical Compton camera at the distance between the scatterer and the absorber of 50 mm.

6.4 Optimization of image reconstruction for the medical Compton camera

In chapter 5, we proposed the multi-angle data acquisition method for the 3-D image reconstruction. Here, we optimize the reconstruction method as suitable for the medical Compton camera developed above and evaluated the basic imaging performance.

6.4.1 Dependence on the number of data acquisition angle

In the section 5.2, we applied 4-angles data acquisition for multi-angle measurement as the first step. In this section, we evaluate the dependency of imaging quality on the number of data acquisition angle in general. As described in chapter 5, the multi-angle method is useful for reducing the uncertainty of the spatial resolution in the depth direction, thus assuming symmetric property on the imaging region the number of angle is needed to be more than three. In the simulation, we optimized the data acquisition configuration in the case of the medical Compton camera in terms of the spatial resolution, reproducibility of diffuse source, and comprehensive performance.

For this purpose, we firstly investigated the spatial resolution in the case of 4-angles (90° pitch), 8-angles (45° pitch), and 12-angles (30° pitch) data acquisition configuration. We image a ^{137}Cs point source at two representative positions of position-1 (X, Y, Z)=(0 mm, 0 mm, 0 mm), that is the center of the imaging region, and position-2 (20 mm, 0 mm, -20 mm) under each data acquisition configuration. Not to be affected by event statistics, we arrange the total amount of gamma-ray irradiation to be the same for each configuration. Fig. 6.15 shows the imaging results. The *top*, *middle*, and *bottom* rows represent the SBP, MLEM reconstruction results of position-1, and the MLEM results of position-2, respectively. The $left$, *center*, and $right$ columns represent 4-angles, 8-angles, and 12-angles data acquisition, respectively. The number of iteration of these MLEM images is all 20. We evaluated the spatial resolution by taking FWHM for these MLEM images in the X, Y, and Z directions. The evaluation results are shown in Fig. 6.16, where the horizontal axis indicates the number of data acquisition angle and the vertical axis indicates the spatial resolution. In the result of position-1, there is little practical difference between the spatial resolutions of each step number. However, in the result of position-2, the spatial resolutions of more than 8-steps was improved compared with those of 4-steps in all directions. In fact, as shown in Fig. 6.15, at the position-2 in 4-angles data acquisition the image has visible uncertainty in oblique direction due to the lack of intersecting data. Although it is obvious that as data acquisition angle increases the image becomes better, at least in the case of assumed situation, there is no significant difference in the configuration of over 8-angles. Furthermore, from Fig. 6.16 we can confirm that the spatial resolution in the Y direction is better than those in the X and Z directions in

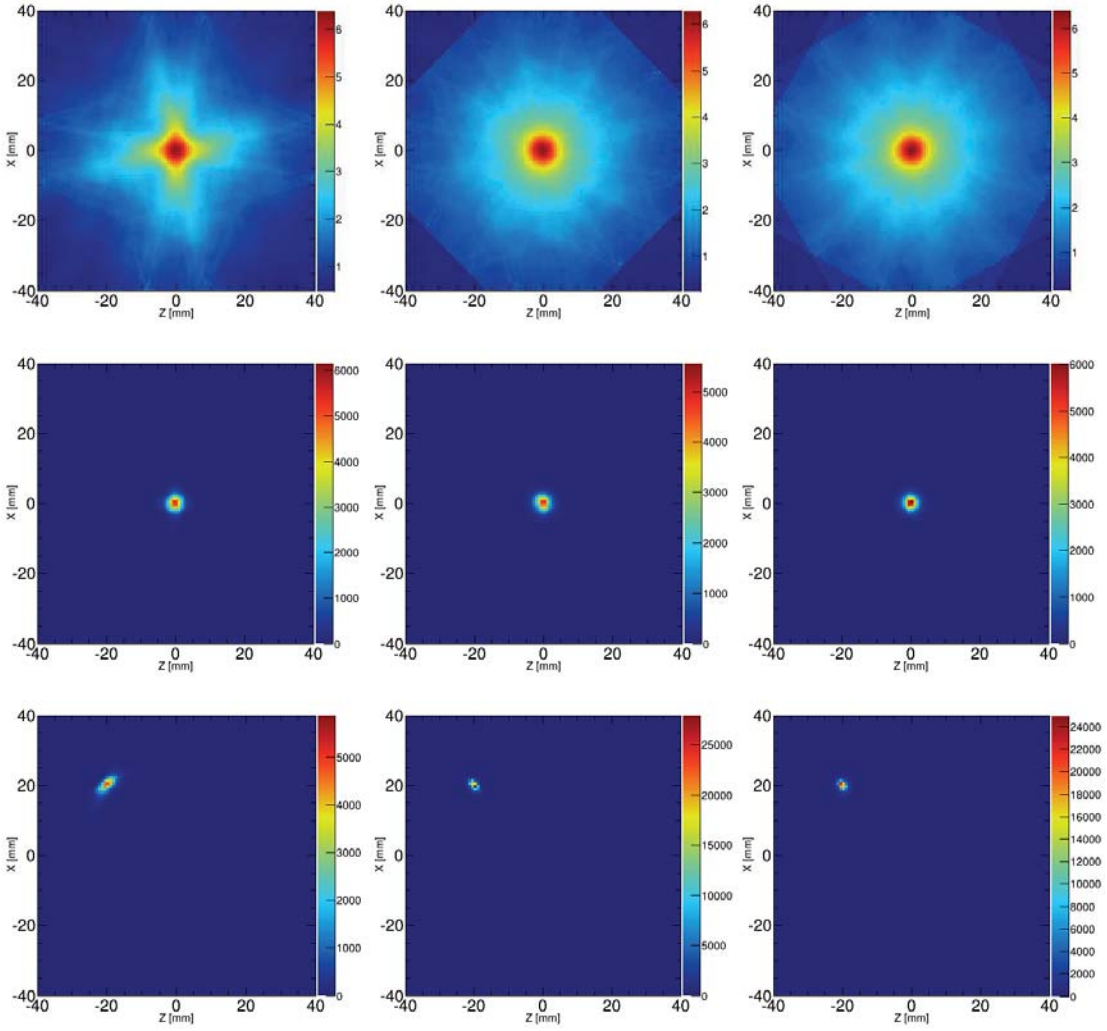

Figure 6.15: Comparison the imaging results of ^{137}Cs point source at the center of FOV under various number of data acquisition angle. The *top*, *middle*, and *bottom* rows show the SBP, MLEM results of position 1, and MLEM results of position 2, respectively. (*Left*) 4-angle, (*center*) 8-angle, and (*right*) 12-angle data acquisition.

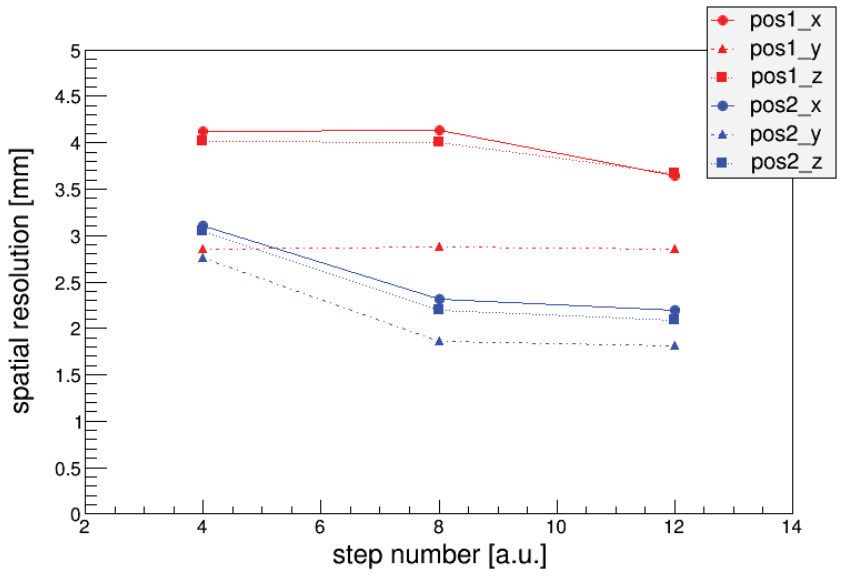

Figure 6.16: Spatial resolutions as a function of number of data acquisition angle

all step number. This is because the depth-direction uncertainty of a Compton camera mainly influences the spatial resolution in the X and Z directions.

As well as the evaluation of the spatial resolution for a point source, we also investigated the imaging performance for diffuse source. As an example of the simplest diffuse source, we simulated the uniform circle plane source with a radius of 10 mm. For the evaluation of imaging quality, we applied the normalized mean square error (NMSE) value, which represents the consistency between the original image and the reconstructed image. The NMSE value is expressed in the following formula:

$$NMSE = \frac{\sum_{x,y}(g(x,y) - f(x,y))^2}{\sum_{x,y} f(x,y)^2}, \tag{6.1}$$

where $g(x,y)$ and $f(x,y)$ denote the original image and the reconstructed image, respectively. Fig. 6.17 shows the original image in this evaluation and the MLEM imaging results after 10 iterations under the configuration of 4-angles, 8-angles, and 12-angles data acquisition. In the result of 4-angles, the circle shape of the source can not be reconstructed because of the lack of intersecting Compton cone data. In contrast, in the results of 8-angles and 12-angles data acquisition, it appears that the circle shape is reconstructed almost correctly. Indeed, Fig. 6.18 shows the results of NMSE value which are estimated from these reconstructed images as a function of the step number. The low NMSE value indicates good consistency between the original image and the object image, so that from Fig. 6.18 we can confirm that the reproducibility improves as increasing the number of

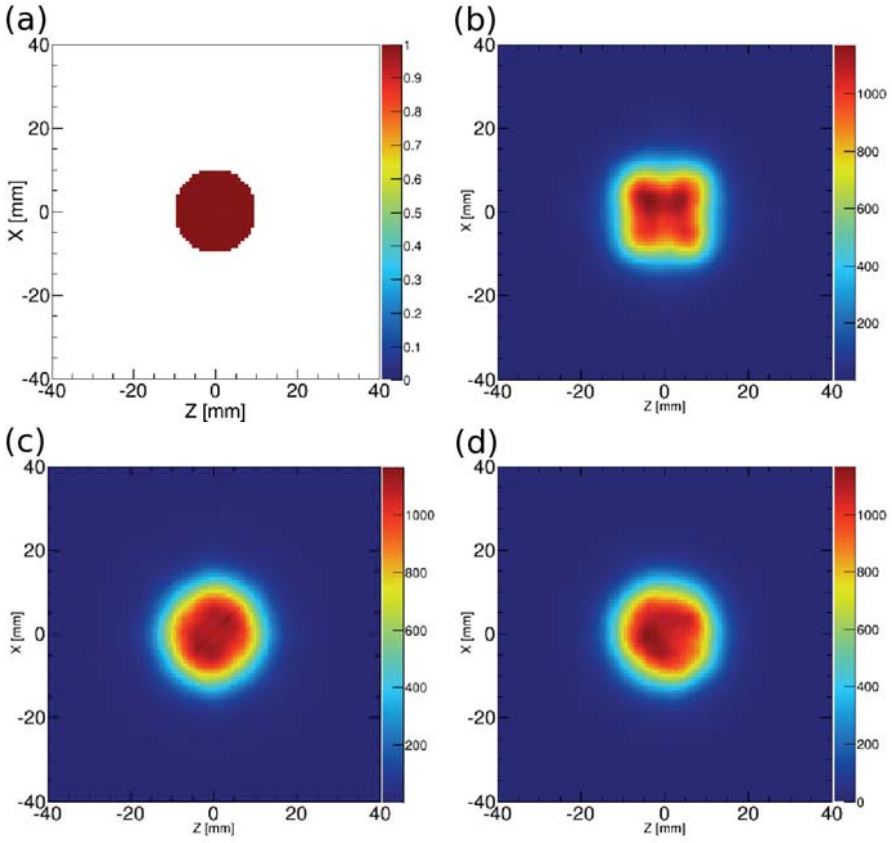

Figure 6.17: Imaging results of ^{137}Cs diffuse source. (*a*) The original image (r =10 mm), and the MLEM results in (*b*) 4-angles, (*c*) 8-angles, and (*d*) 12-angles data acquisition.

data acquisition. Hence, as well as the results of the spatial resolution evaluation the optimal number of the data acquisition in real situation should be determined by considering the trade-off between the required image quality and the measurement costs. In this study, we apply the 12-angles data acquisition for all 3-D image reconstruction.

6.4.2 Positional dependence of spatial resolution and intensity in 12-angles data acquisition

Based on the above study, we then evaluate the imaging performances under 12-angles data acquisition. First, Fig. 6.19 shows the relationship between the MLEM iteration number and the spatial resolution for a ^{137}Cs point source in the situation of position-1 described in the previous subsection. The *red* and *blue* plots denote the resolutions in the X and Y direction, respectively. Although the spatial resolutions become better as increasing the iteration number, each resolution converges on a certain value. The optimized iteration

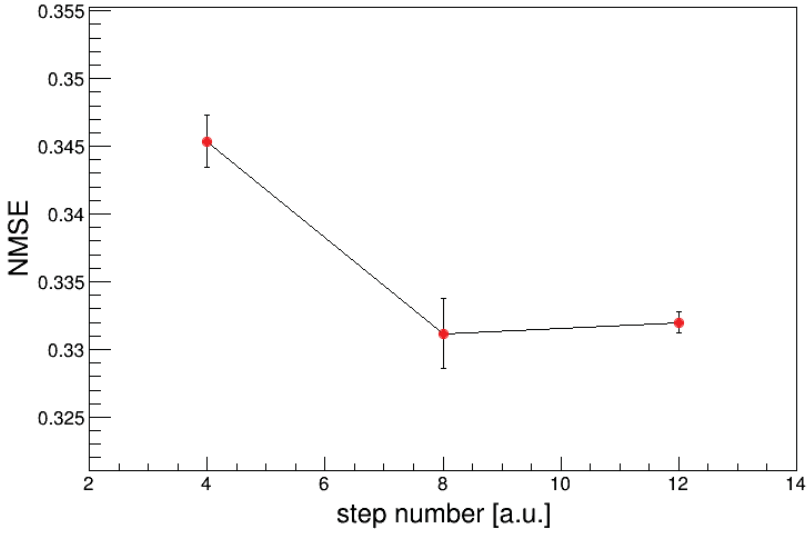

Figure 6.18: NMSE value as a function of number of data acquisition angle.

number where the spatial resolution adequately converges depends on the factors of the configuration of the imaging target and event statistics. For this example case, after 20 iterations, the spatial resolutions in the X and Y direction change only 23.6% and 18.3%, respectively.

In addition, we also evaluate the positional dependence of the image at 12-angles data acquisition. As shown in Fig. 6.20, we reconstruct the MLEM image of a ^{137}Cs point source under various positions both in the X and Y directions independently. The iteration number here is 20. Fig. 6.21 (*top*) shows the 1-D profiles of 3-D imaging result, and Fig. 6.21 (*middle*) and (*bottom*) show the results of the spatial resolution and the relative intensity at each position, respectively. Note that the reconstructed positions quantitatively agree well with the real positions. The averaged errors of reconstructed position are 0.12 mm and 0.41 mm in the X and Y directions, respectively. As is the case in section 5.3.1, the spatial resolution of the reconstructed image gradually improves as increasing the distance from the center of FOV in the X direction. Comparing the center and the edge of FOV in the Z-X plane, the spatial resolution improves by 1 mm at most. Furthermore, the intensity has a tendency to decrease with increasing the distance from the center both in the X and Y directions. Although it is preferable that the intensity has no positional dependence over the whole image region, this results show that the intensity may vary at the maximum of 25% in the defined 3-D image region of this study.

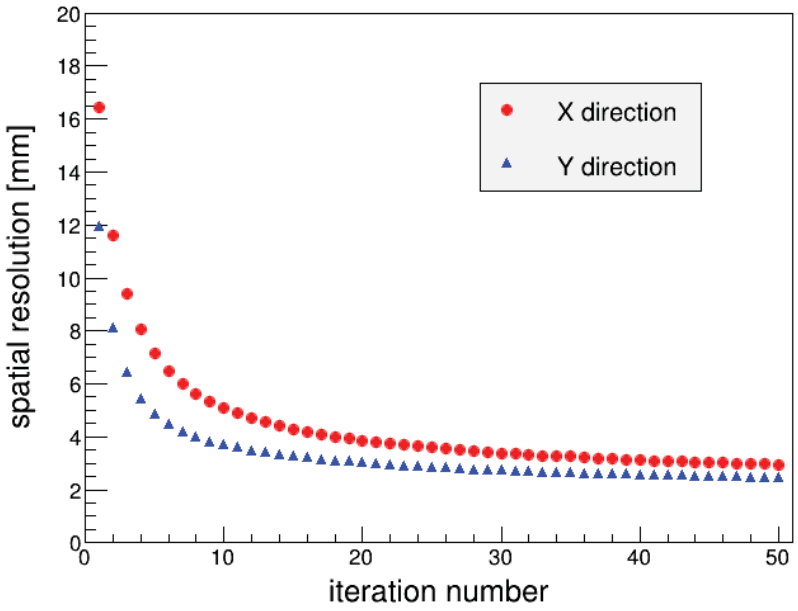

Figure 6.19: Spatial resolution of a ^{137}Cs point source at the center of FOV as a function of the number of iteration.

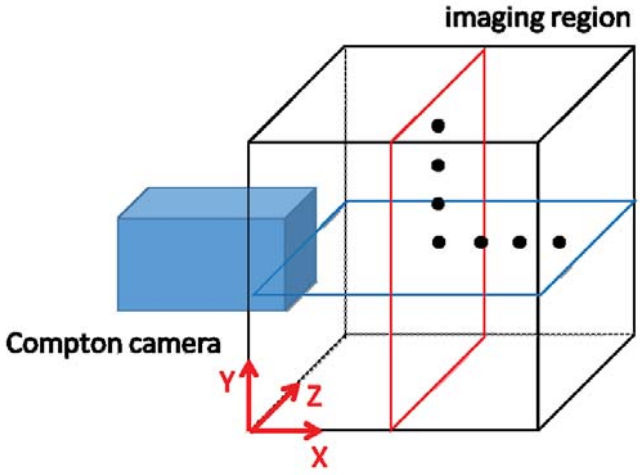

Figure 6.20: Schematic geometry to evaluate positional dependence.

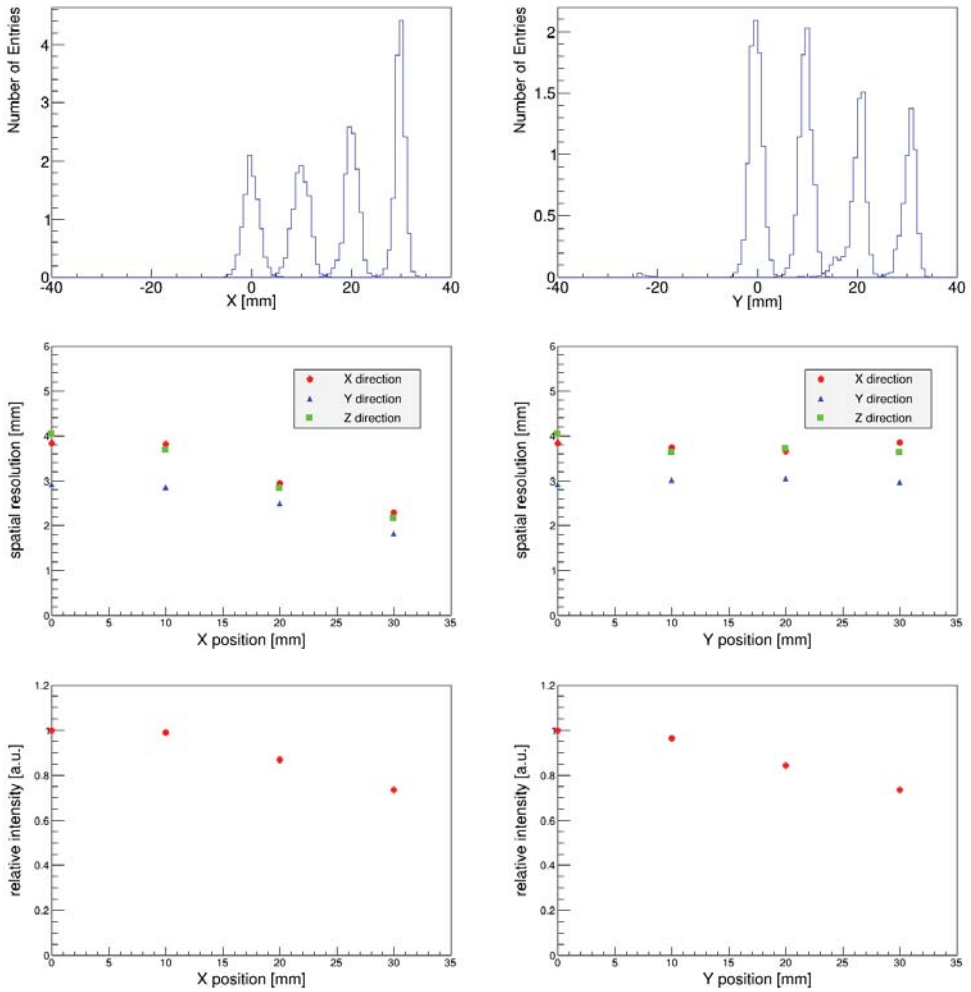

Figure 6.21: Spatial resolution and relative intensity of a ^{137}Cs point source as a function of the position on the image region. (*Top*) the 1-D profiles of 3-D imaging result, (*middle*) the spatial resolution in the X, Y, and Z directions, and (*bottom*) the relative intensity. *Left* and *right* columns denote the response for the source in the X and Y positions, respectively.

6.4.3 Uniformity for multi-energy imaging

For a Compton camera, quantitative capability of the reconstructed image is one of the key but challenging problem which has to be improved. Especially in medical imaging, the quantitative performance is one of the most important factors, hence we aimed to reconstruct the relative source intensity more precisely not only for single energy but for various gamma-ray energies. Obviously, detector response depends on gamma-ray energy, so that it is needed to compensate this difference of detector response especially in conducting multi-energy simultaneous imaging.

For this purpose, we add in the reaction probability factor to the MLEM reconstruction algorithm described in section 5.1. This factor takes account the difference of detector response to different energy. When conducting 3-D multi-color imaging in medical use, the system matrix t_{ij} is thus replaced as following equation:

$$t_{ij} = T_{ij} \times \exp\{-\sigma_t(E_1 + E_2) \cdot x\} \cdot \frac{d\sigma_C}{d\Omega} \cdot \exp\{-\sigma_t(E_2) \cdot x\} \cdot \sigma_{p,C}, \tag{6.2}$$

where T_{ij} denotes the system matrix described in equation (5.2), $\exp\{-\sigma_t(E_1 + E_2) \cdot x\}$ and $\exp\{-\sigma_t(E_2) \cdot x\}$ denotes the transportation probability that photon does not interact on the pass in the scintillator, $\frac{d\sigma_C}{d\Omega}$ denotes the Compton scattering probability of a photon which has the energy of E_1+E_2 in the scattering angle θ, and $\sigma_{p,C}$ denotes the interaction probability of a photon of energy E_2 either by photoelectric absorption or Compton scattering. Although the last term considers in general only photoelectric absorption probability, we also add Compton scattering probability here because in our Compton camera the impact of multiple-scattering event can not be ignored as described in section 4.9.3. Furthermore, in the calculation of transportation probability, although the length of the photon pass should be properly calculated by each event, in this study we alternatively apply a constant value that is an averaged length of the photon pass for whole used events in order to reduce the computation time. We calculate these probabilities event by event as functions of measured interaction position, energy deposit, and scattering angle. In following simulation and experimental studies, we use this algorithm.

6.5 Imaging performance

6.5.1 Double source imaging

Here, we experimentally evaluate the imaging capability of the medical Compton camera with various gamma-ray sources. Firstly, we imaged double ^{137}Cs point sources separated by a distance of 9 mm in order to confirm the separation capability of the medical Compton camera. In this measurement, we apply the single-angle data acquisition. The distance to

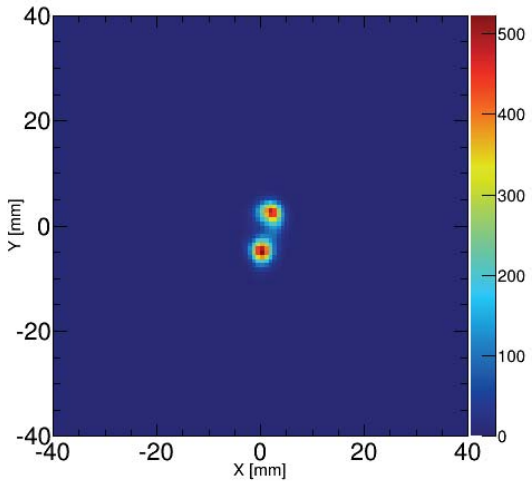

Figure 6.22: 2-D MLEM imaging result of the double ^{137}Cs sources measurement after 20 iterations.

the sources is 40 mm, and the measurement time is 300 sec. Fig. 6.22 shows the MLEM imaging results after 20 iterations. Note that, the two sources are clearly distinguished each other. Although the detection efficiency of the medical Compton camera was reduced compared with that of the DOI camera, it succeeded in imaging the precise configuration of double sources several millimeter apart in a few minutes.

6.5.2 Imaging of uniform line source

Next, we conducted an imaging of the uniform 1-D line source. In this experiment, we mimic the uniform line source by moving ^{137}Cs point sources at a constant speed. Fig. 6.23 shows the schematic geometry of the experiment. For the constant velocity motion of the sources, we utilized a programmed 1-D precision migration stage. The length of source motion is 8 cm, and the migration speed is 0.1 mm/sec, taking 1600 sec for a stroke. We measured the source at two distances of 20 cm and 10 cm in single-angle data acquisition, which correspond to viewing angles of the line source of $\pm 11.3°$ and $\pm 21.8°$, respectively. The integration time is 16 hours, which is equal to 36 strokes.

Fig. 6.24 shows MLEM imaging results and its 1-D slices in the X direction by each geometry: Fig. 6.24 (*left*) shows the result measured at a distance of 20 cm and Fig. 6.24 (*right*) shows at a distance of 10 cm, respectively. In this experiment, we evaluate the uniformity and the spatial resolution for quantitative estimation. First, for the uniformity evaluation of the reconstructed images, we calculate the dispersion in the region

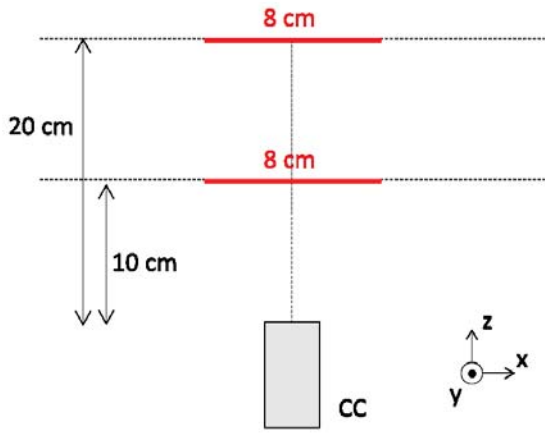

Figure 6.23: Schematic view of geometry of the line source measurement.

eliminating the edge of the line. We apply the error function as described in

$$erf(x) = \frac{2}{\sqrt{\pi}} \int_0^x e^{-t^2} dt \tag{6.3}$$

to the result of 1-D slice in the X direction, and the range in 2σ from the reconstructed line edge position is assumed as the edge. In Fig. 6.24, the red line shown in X profile represents the averaged level in the evaluated region. The results of dispersion in this region are 2.23% for the distance of 20 cm and 9.77% for 10 cm. These results indicate an example of imaging capability for diffuse line source with the uniformity of less than 10%.

Next, the spatial resolution is also evaluated by the FWHM of a profile in the Y direction at X=0 cm. The evaluation results for the distance of 20 cm and 10 cm are 16.4 ± 0.2 mm and 8.69 ± 0.08 mm, respectively. Fig. 6.25 shows the measured spatial resolution as a function of the distance to the source. The black line in Fig. 6.25 denotes the calculated spatial resolution assuming the angular resolution to 4.2° (FWHM). The experimental spatial resolutions are worse than the calculated one by approximately 1° over all distance. There are the following possible reasons. The first one is that the real source utilized in this experiment has a volume and is not complete point source. This is also consistent with tendency that the offset of the experimental results from the calculated results becomes constant. The other one is that the spatial resolution which is evaluated by line spread function (LSF) as this experiment is not strictly as same as that obtained by point spread function (PSF), because LSF is the integral of the consecutive PSFs. Hence, the spatial resolution based on LSF mathematically tends to be a little worse than that of PSF.

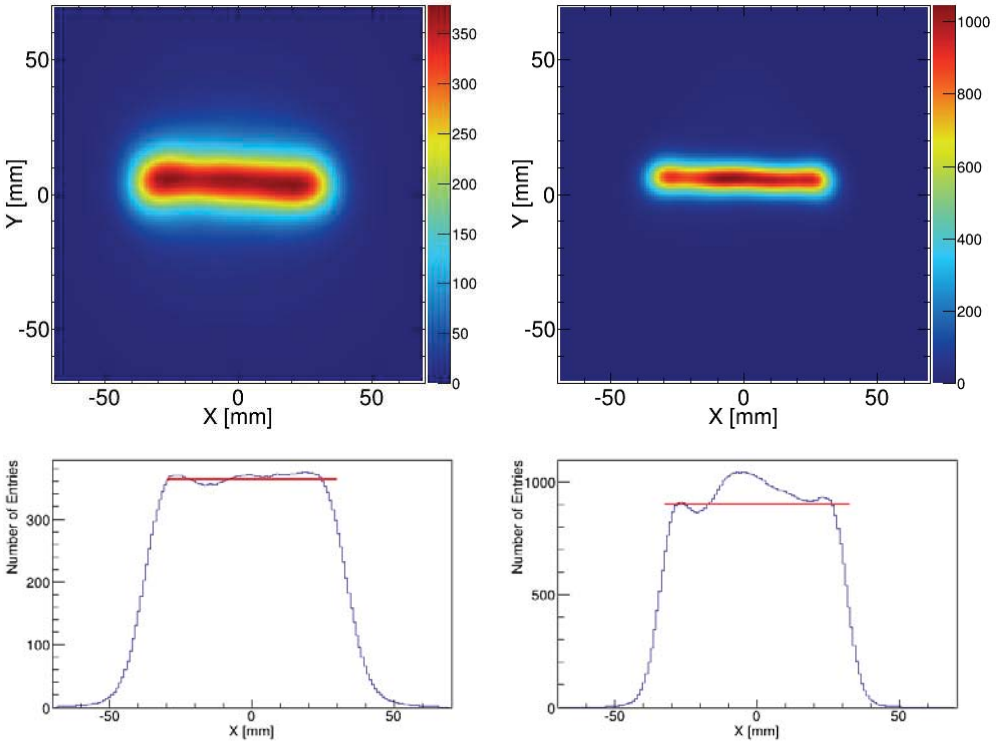

Figure 6.24: MLEM imaging results of the ^{137}Cs line source at a distance to the source of 20 cm (*left*) and 10 cm (*right*) with the 1-D profiles in the X direction.

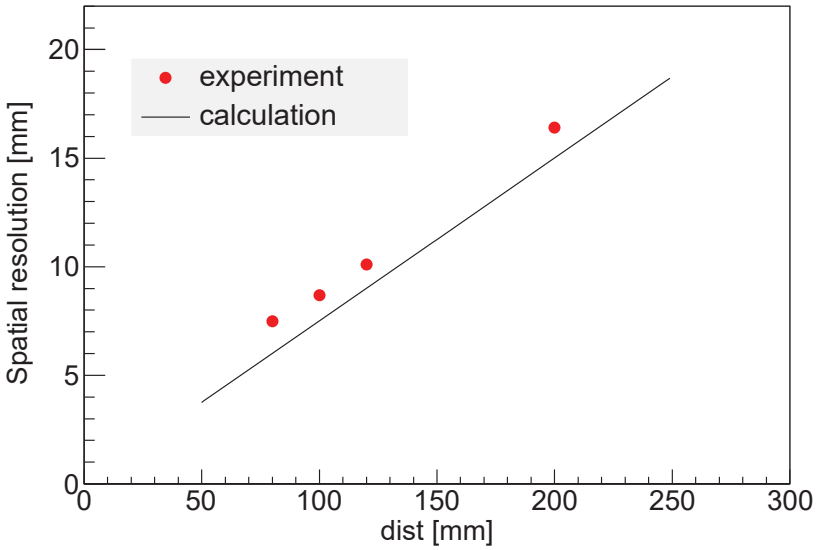

Figure 6.25: The spatial resolution of line source as a function of the distance.

6.5.3 Imaging of a uniform plane source

As well as uniform 1-D line source described above, we also conducted an imaging of an uniform 2-D plane source to evaluate the 3-D imaging capability of the plane source. This experiment was conducted at National Institutes for Quantum and Radiological Science and Technology at Takasaki. We utilize a plane source phantom of 30 mm × 30 mm × 3 mm which is filled with ^{137}Cs solution. The total intensity of the source is 2 MBq. In this measurement, we apply the multi-angle data acquisition and followed by 3-D image reconstruction. For the measurement situation, the plane source is measured under two different geometry patterns as shown in Fig. 6.26: pattern-1 is the case that the plane of rotation of the camera is in parallel with the source plane, and pattern-2 is that it is perpendicular to the source plane. In both geometry patterns, the data acquisition configuration is 12-angles, with each measurement time of 20 min, thus the total integration time is 4 hours. Note that, in the pattern-1 the 3-angles data could not be obtained because of the interference between the plastic case of the liquid source and the medical Compton camera. Hence, in the pattern-1 we compensate the lack of the data by utilizing other angle data as considering the symmetric property.

In the pattern-1, the total detected number of event used for reconstructing the image is 9.04×10^4 events. Fig. 6.27 shows 2-D slices of 3-D MLEM reconstructed image after 30 iterations acquired in pattern-1. Each figure shows 0.8 mm pitch slice in the Z-X plane. Fig. 6.28 (*left*) and (*right*) show the center slice of the 3-D image in the Z-X direction

and the X-Y direction, respectively. We also present their 1-D profile as bottom panels. For these imaging results, we firstly evaluate the spatial resolutions in all three directions from the accuracy of the edge delineation. When evaluating the edge in the X and Z directions, we define the spatial resolution by applying the error function as is the case with section 6.5.2, because the edge spread function (ESF) of a sufficiently-large uniform plane source is ideally given by the convolution of the consecutive LSFs. On the other hand, in the Y direction, the thickness of 3 mm is not sufficiently large compared with the expected resolution. In this case, the response $R(x)$ can be expressed by convolution described the following equation:

$$R(x) = \int LSF(x - x') * e(x')dx' \tag{6.4}$$

$$e(x) = \begin{cases} 1 \ (0 \leq x \leq 3) \\ 0 \ (\mathrm{x} \leq 0, x \geq 3). \end{cases} \tag{6.5}$$

Hence in order to evaluate the resolution in the Y direction, we calculated various response $R(x)$ as a function of σ of the LSF. The resolution in the Y direction is estimated based on the FWHM value of the $R(x)$. These resolution evaluations are applied to the center of 1-D slices of reconstructed image in each direction. As the typical value, the edge delineation in the X, Y, and Z directions are comparable to the spatial resolution of 5.11 mm (FWHM), 4.44 mm (FWHM), and 5.05 mm (FWHM), respectively. Then, in order to evaluate the uniformity of the image, we take the 2-D ROI in the center of Z-X slice (shown in Fig. 6.28 ($left$)) which is determined by eliminating 2σ region of the spatial resolution from the reconstructed edge position. The image uniformity inside the ROI is 8.69% by 1σ.

On the other hand, Fig. 6.29 and Fig. 6.30 show the MLEM image measured in geometry of the pattern-2. The total number of measured event in the pattern-2 is 1.12×10^5 events and the number on iteration of these images is 30. In the evaluation of edge delineation, the spatial resolutions in the X, Y, and Z directions are 5.90 mm (FWHM), 5.33 mm (FWHM), and 6.31 mm (FWHM), respectively. Furthermore, the uniformity of the center of the Z-Y slice becomes 11.5% by 1σ.

In both configurations of the pattern-1 and pattern-2, we can confirm the 3-D configuration of the square source. The above results show an example of imaging results in the case of after 30 iterations, in contrast Fig. 6.31 (*top*) and (*bottom*) show the uniformity and spatial resolution as a function of iteration number, respectively. These results suggest that the uniformity takes the best value of around 10% when the iteration number is around 20−30 both in the pattern-1 and pattern-2. On the other hand, the spatial resolution becomes better as increasing the iteration number in the range of under 40 in both patterns. This indicates that increasing the number of iteration would improve the

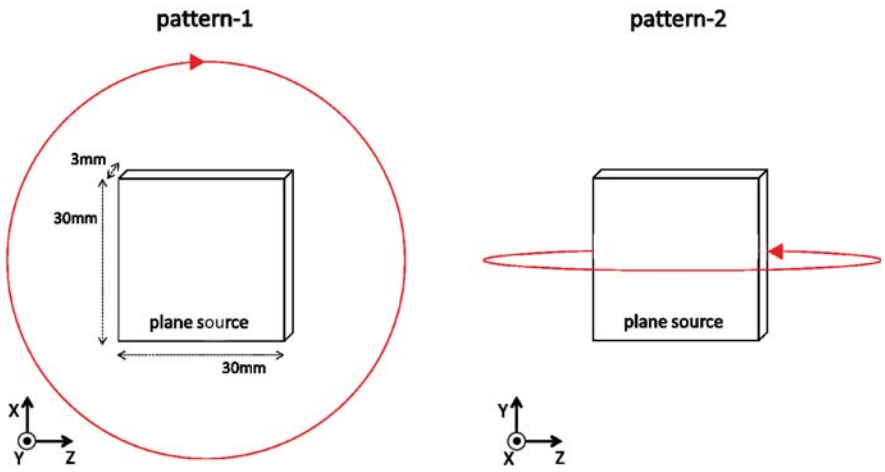

Figure 6.26: Diagram of geometry of plane source imaging. (*Left*) In the pattern-1 the plane of rotation of the camera is in parallel with the source and (*right*) in the pattern-2 it is in perpendicular to the source plane.

spatial resolution, which is close to the value obtained by the point source measurements, however, because the amount of statistics is insufficient the fluctuation of each voxel stands out and the performance of the uniformity degrades. It should also be noted that results of the spatial resolution among the patterns and the directions well reflect the relative tendency of the resolution described in section 6.4.2, which depends on the coordinate position in the imaging region and the evaluation direction (seen in Fig. 6.21). Furthermore, the consistency of the source intensity between the patterns should be kept because the same plane source was used for the imaging. We utilize the averaged voxel value inside the ROI after 30 iterations for comparing the two imaging results. The averaged voxel values in the pattern-1 and pattern-2 are 0.414 ± 0.036 and 0.331 ± 0.038, respectively, so that these values agree with each other within uncertainty of $\sim$20%.

6.5.4 Multi-color imaging

In order to investigate the imaging performance for various energy sources, we then conducted a multi-color 3-D imaging. We use three syringe phantoms, filled with three different RI tracers of ^{18}F (511 keV), ^{137}Cs (662 keV), and ^{65}Zn (1116 keV). The diameter of the syringe is 4.5 mm, and the height of the liquid in each syringe is about 5 mm. These syringes are arranged as shown in Fig. 6.32, where the distance between each syringe becomes 15 mm. The detail information of each tracer such as energy and intensity is listed in Table 6.3. We also apply 12-angles data acquisition method with each measurement time of 300 sec, making the total integration time is 60 min. Fig. 6.33 shows the

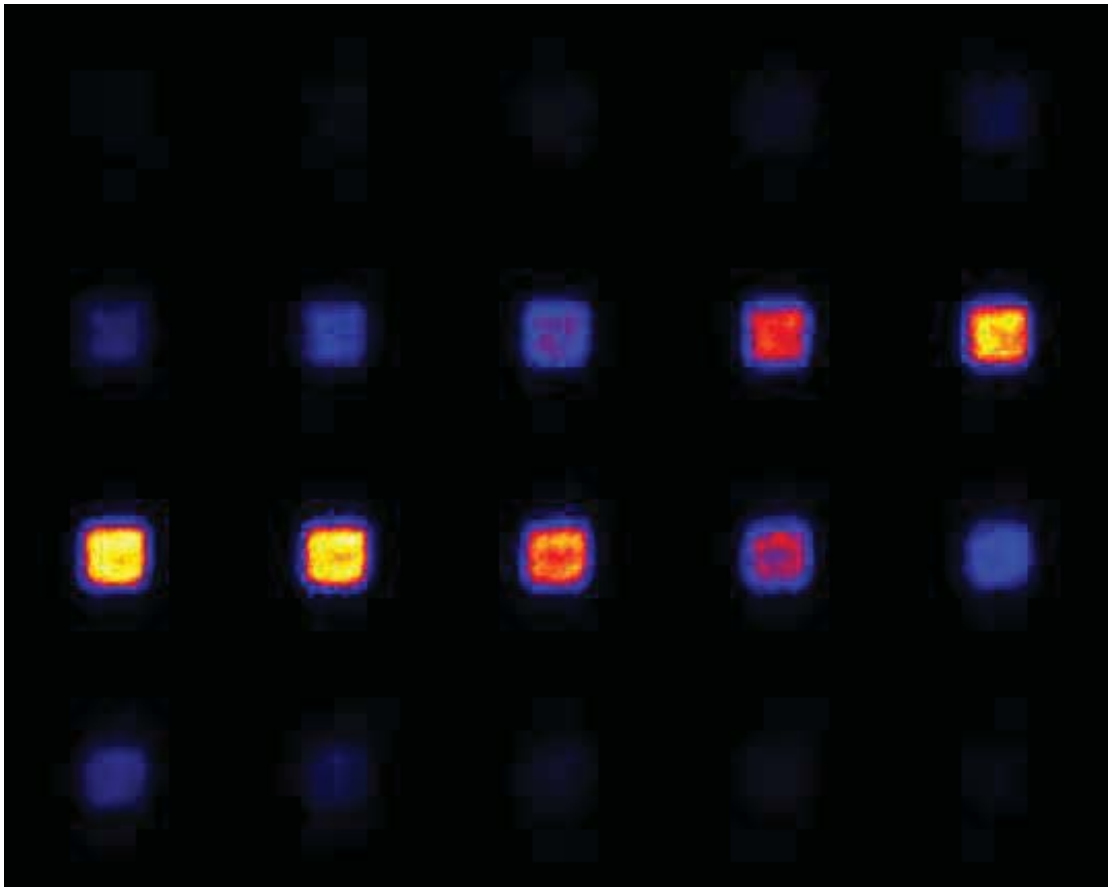

Figure 6.27: 2-D slices of the plane source image as measured in the pattern-1. Each figure shows 0.8 mm pitch slice in Z-X plane.

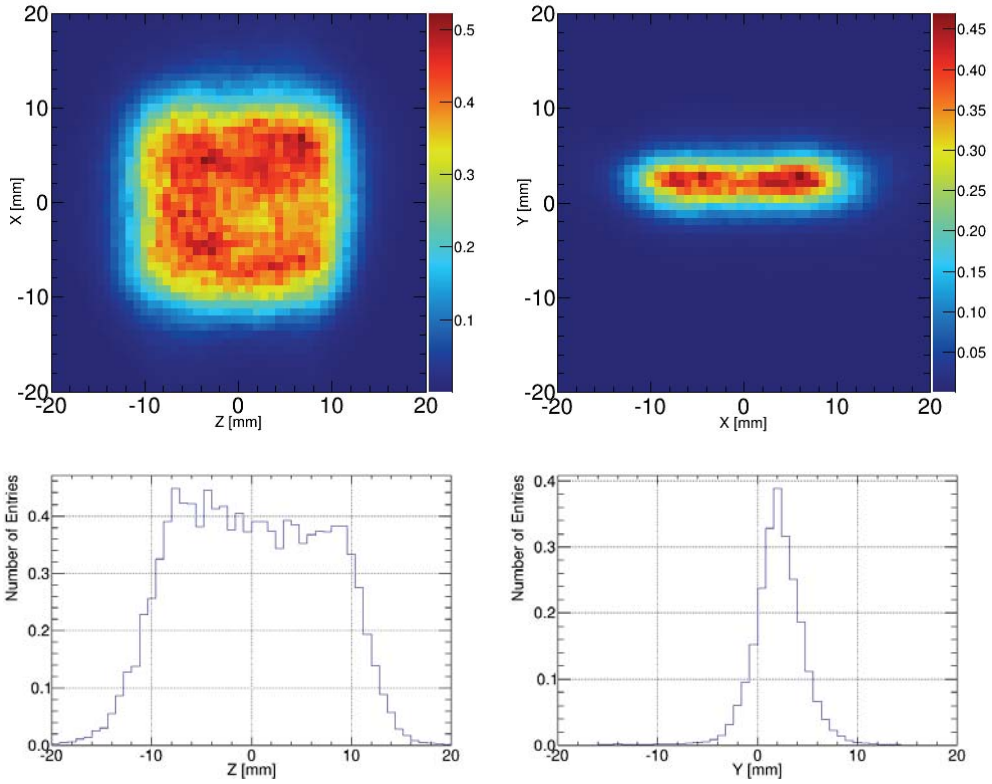

Figure 6.28: 2-D slices of the 3-D imaging result in the pattern-1 at the center. ($Left$) in the Z-X direction and ($right$) in the X-Y direction.

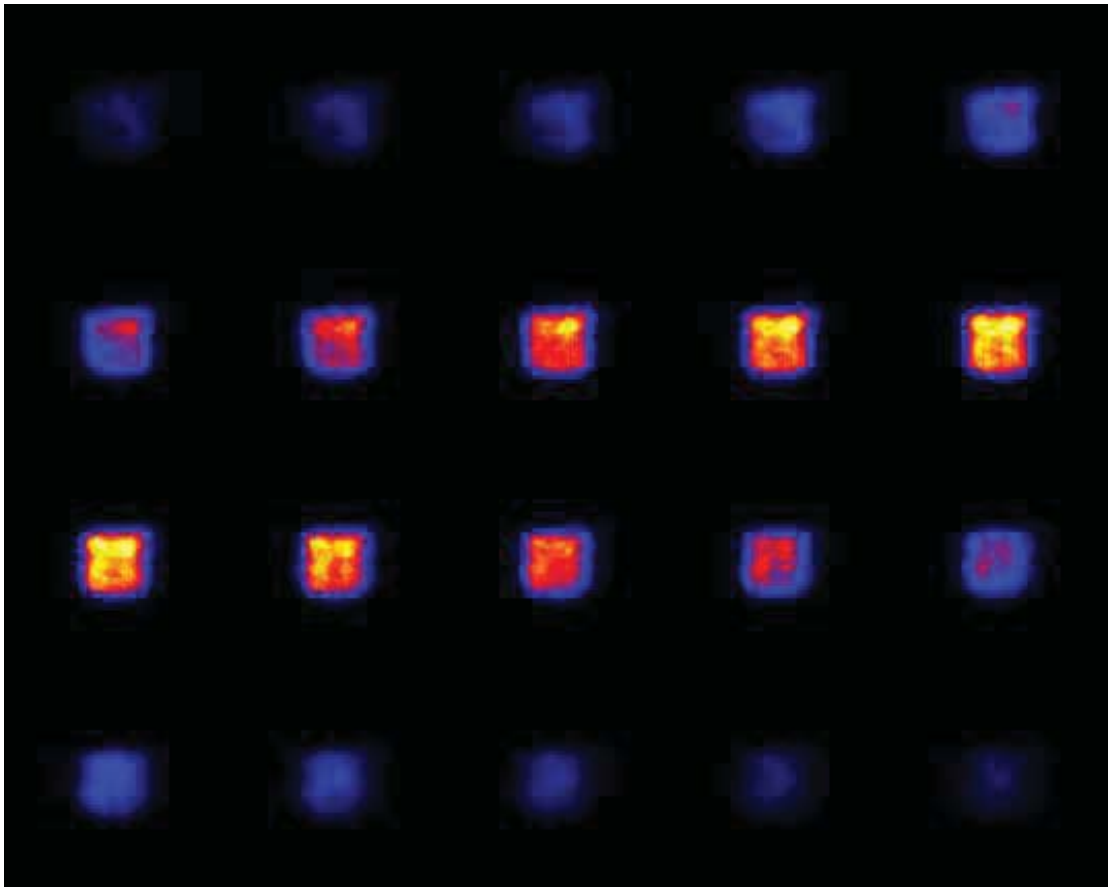

Figure 6.29: 2-D slices of the plane source image as measured in the pattern-2. Each figure shows 0.8 mm pitch slice in Z-Y plane.

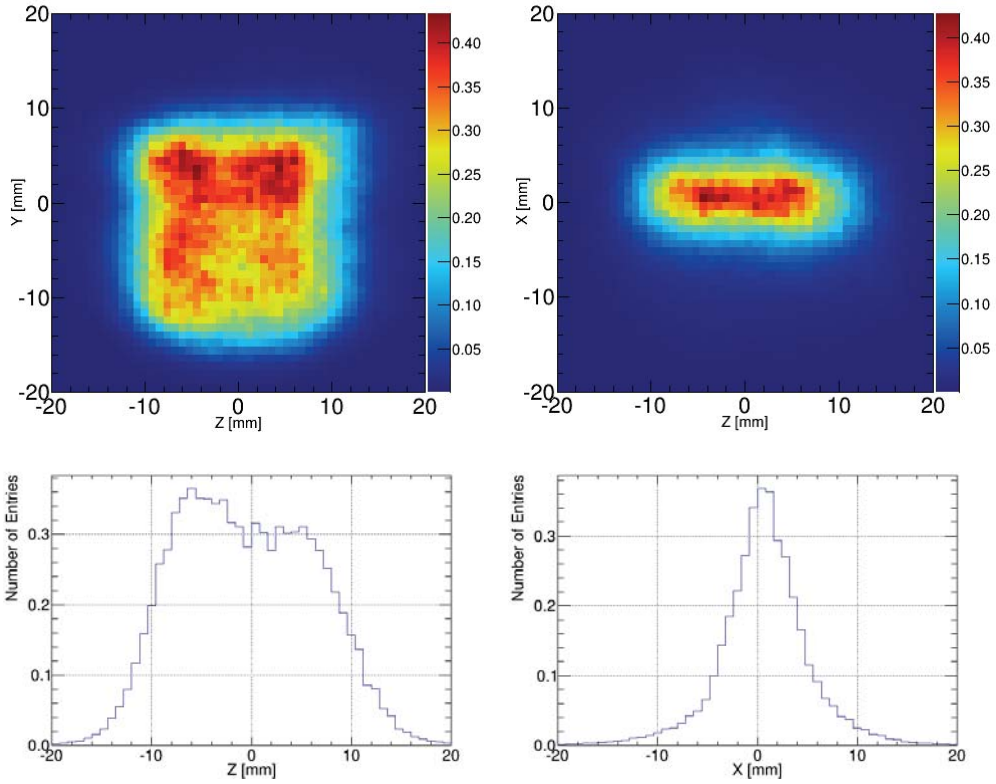

Figure 6.30: 2-D slices of the 3-D imaging result in the pattern-2 at the center. ($Left$) in the Z-Y direction and ($right$) in the Z-X direction.

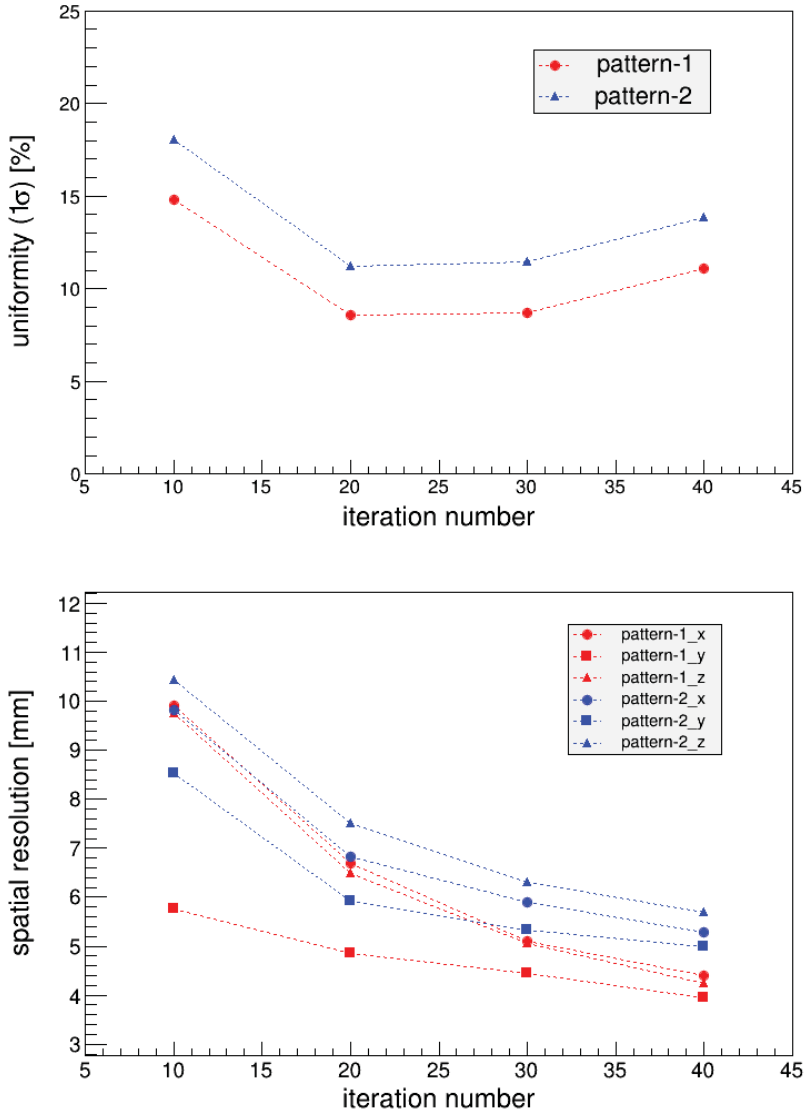

Figure 6.31: (*Top*) Uniformity and (*bottom*) spatial resolution as a function of the number of iteration.

Table 6.3: RI tracers used for multi-color imaging.

RI tracer	Energy [keV]	Decay time	Emitting ratio [%]	Intensity @ outset [MBq]
^{18}F	511	109.7 m	0.967×2	0.600
^{137}Cs	662	30.1 y	0.851	0.692
^{65}Zn	1116	244 d	0.506	0.561

result of energy spectrum. From this result, the three energy peaks of 511 keV, 662 keV, and 1116 keV are confirmed. The peak around 200 keV represents the concentration of the back-scattering events. Fig. 6.34 (*left*) shows 3-D MLEM imaging results after 15 iterations reconstructed by applying each energy cut range listed in Table 6.2. Fig. 6.34 (*right*) shows its representative 2-D slice in the Z-X direction. The blue, red, and green plot denote the results for 511 keV, 662 keV, and 1116 keV, respectively. The configuration of three syringes is also reconstructed correctly, that is, at original positions and in reflecting the syringe shape. Furthermore, Fig. 6.35 shows the 1-D profiles of Fig. 6.34 (*right*) in the X direction at the center of each syringe. The FWHMs of each profile are 5.5±1.1 mm, 5.0±0.9 mm, and 4.2±0.6 mm for 511 keV, 662 keV, and 1116 keV peak, respectively. The difference between the FWHM values reflects the energy dependence of the spatial resolution.

From the above studies, it is indicated that the imaging results based on the integration time of total 60 min produced the correct configuration of the syringes. Then, we evaluate the relationship between image quality and the amount of statistics in the case of this syringe measurement. A part of the data corresponding to the measurement time of 10 min, 20 min, and 30 min is extracted from the measured data, and MLEM reconstruction is conducted for each data set. Fig. 6.36 shows the representative 2-D slice of the reconstructed images. Although the images which are equivalent to 60 min (equal to Fig. 6.34 (*right*)) and 30 min measurement correctly represent the circle shape of the syringes, in the images derived from 20 min and 10 min measurement, the 1116 keV image (green) is not visualized in clear circle shape. Although the event statistics and measurement time required for image reconstruction obviously depend on the configuration of the object, these results provide an example that even for the sources as weak as 1 MBq we can correctly image the 3-D configuration of the sources with relatively short integration time of no less than 30 min in this situation.

6.5.5 Quantitative estimation for multi-color imaging

Here, we evaluated the quantitative capability for the case of multi-different-energy imaging. In general, the degradation of the quantitative performance can be explained by two

Figure 6.32: Photograph of syringe phantoms filled with ^{18}F, ^{137}Cs, and ^{65}Zn.

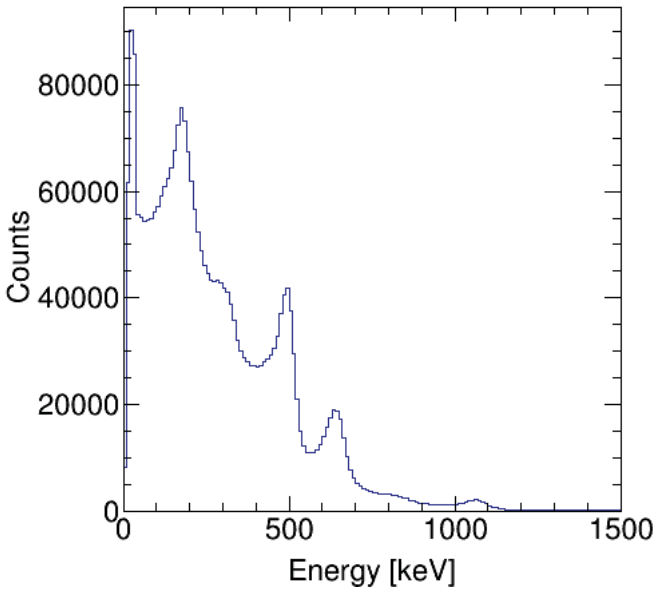

Figure 6.33: Energy spectrum of multi-color gamma-ray measurement as a sum of detector energy deposit.

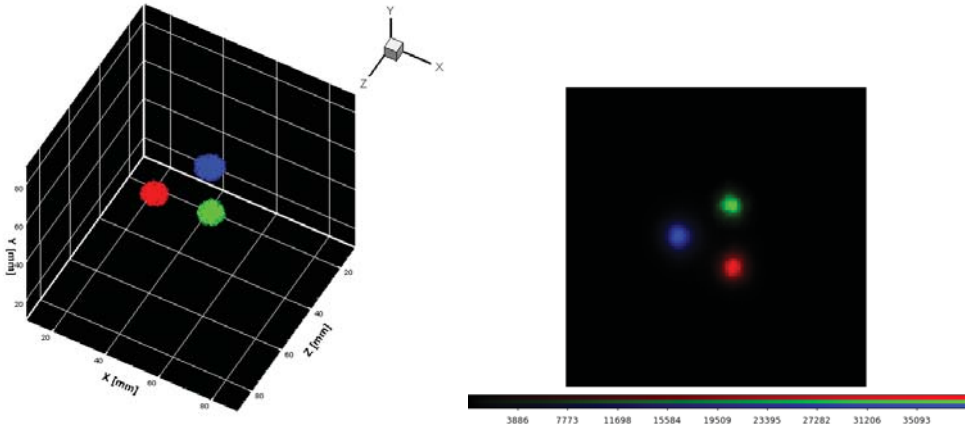

Figure 6.34: MLEM imaging result of multi-color measurement. (*Left*) 3-D MLEM reconstruction image and (*right*) its 2-D slice in X-Y plane. The blue, red, and green plot denote 511 keV, 662 keV, and 1116 keV image, respectively.

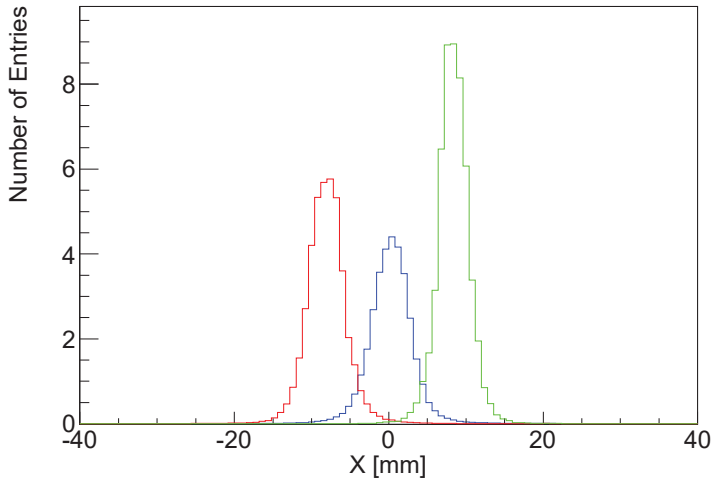

Figure 6.35: X profile of the multi-color phantom imaging result. The blue, red, and green line denote 511 keV, 662 keV, and 1116 keV image, respectively.

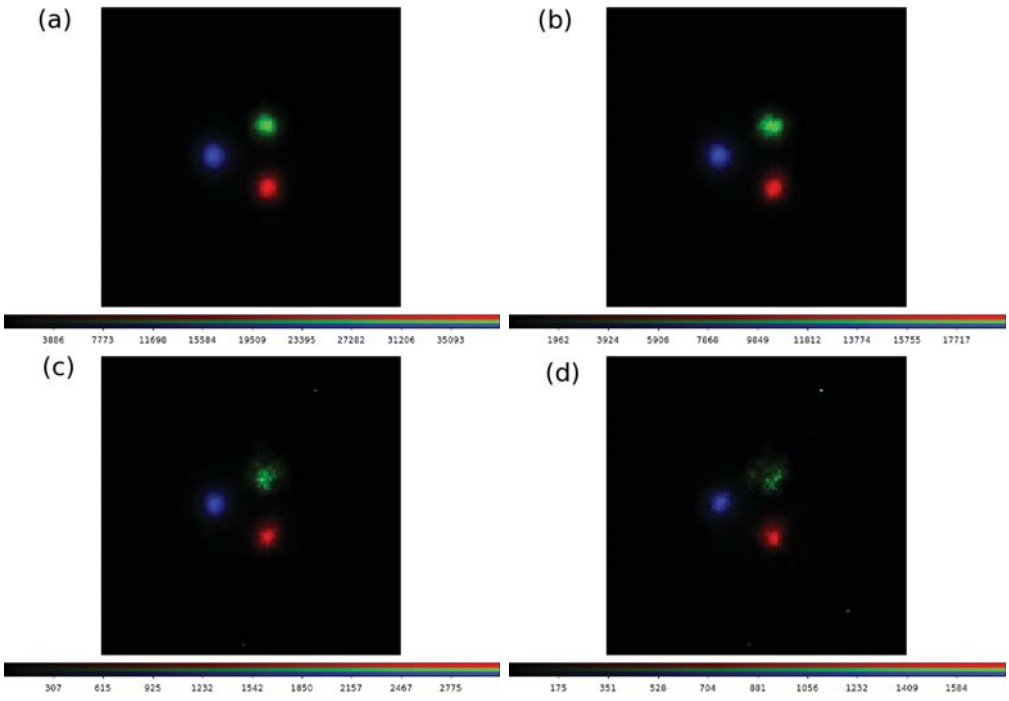

Figure 6.36: Comparison of MLEM images on various event statistics. (*a*) 60 min, (*b*) 30 min, (*c*) 20 min, and (*d*) 10 min measurement.

major reasons: the uncertainty of accuracy of the image reconstruction method and the escape events which is described in section 4.10.

In this section, we first reconstruct the multi-color syringe imaging described in the previous section on Geant4 simulation and investigate the each above effect. In the simulation, 1.2×10^9 events of gamma rays are irradiated isotropically from each source with the same intensity, and 12-angle data acquisition is applied. In order to investigate the intrinsic quantitative reconstruction performance and the effect of the escape event separately, we assume the following two situations:

- reconstructing each source individually without any other energy sources (*each*)
- reconstructing each source when all sources are arranged at the same time (*all*).

The *each* situation simply reflects the intrinsic imaging performance, whilst the *all* situation also includes the effect of the escape events. The practical multi-color imaging as described in section 6.5.4 is equal to the *all* situation. The intensity of the image is calculated by the integral value inside the 3-D ROI (r=10 mm). Note that, the positional dependence of the image response as described in 6.4.2 is ignored in this study, because the three syringes are located at equivalent position each other on the image region under 12-angles data acquisition.

Before evaluating the imaging results, Fig. 6.37 shows the number of event used for image reconstruction. The difference between the *all* and *each* situation is due to the effect of the escape events. This effect becomes significant at lower energy, in 511 keV energy range at the *all* situation the ratio of escape events becomes 40.0% out of used events. On the other hand, Fig. 6.38 shows the results of intensity obtained from the image. This result shows that the relative intensity among different energy sources is reconstructed with an error of 8.3% based on the average of the three sources even in the *all* situation. Note that, in spite of the result that the escape events are considerable in Fig. 6.37, the the impact of the escape events is largely reduced in the quantitativity of the image as shown in Fig. 6.38. For further understanding, we investigate the effect that the escape event may cause on the reconstructed image. Fig. 6.39 shows the SBP imaging results only by escape events, which are emitted from 662 keV source (Fig. 6.39 ($left$)) and 1116 keV source (Fig. 6.39 ($right$)) and are matched for the energy conditions of imaging 511 keV gamma rays. These figures suggest that the image of escape events concentrates around the position where each gamma rays are emitted. Hence, the reason that the escape events have little impact on the quantitative performance of the image is thought to be that these events provide only marginal contribution to other ROIs. This is because of the geometric configuration that the source positions are located far away from each other in this case. Thus in general, the escape events may have a possibility to degrade the quantitative performance. In our future work, techniques for eliminating the

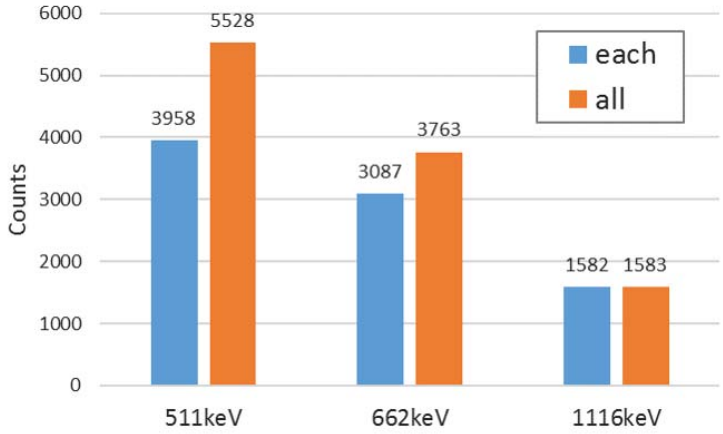

Figure 6.37: Comparing the event number used for image reconstruction in multi-color imaging.

escape event should be implemented to the Compton camera.

Based on these simulation studies, we evaluated the experimental quantitative capability of the multi-color syringe imaging in section 6.5.4. When we calculate the quantitativity of the reconstructed image, we correct the factors of (1)the difference of the actual RI tracer intensity, (2)gamma ray emitting ratio, and (3)decay time listed in Table 6.3 and normalize the intensity of the three sources. Fig. 6.40 shows the results of the number of detected events and the reconstructed intensity for each source. The diagonal and the filled bars denote the number of event used and the intensity of the image after the normalization, respectively. As a result, the maximum deviation of the intensity based on the averaged value is 16.0% at the 662 keV image. This experimental result suggests that we succeeded in obtaining a 3-D image of different energy sources simultaneously with under 20% accuracy of the quantitative performance.

6.6 Small-animal imaging

We finally conducted an imaging test with a living mouse by our Compton camera using multiple tracers. This experiment was carried out according to the Osaka University Animal Experimentation Regulations. We measure an 8-weeks-old male mouse (39.9 g) which was fed by low-iodine diet for two-weeks. For this mouse, the following three radioactive tracers are utilized: (1) ^{131}I-NaOH (4.0 MBq) is injected 2 days prior to the imaging experiment, (2) $^{85}SrCl_2$-HCL (1.12 MBq) is injected 1 day prior to the imaging experiment, and (3) $^{65}ZnCl_2$-saline (0.93 MBq) is injected 1 hour prior to the imaging experiment. The features of these tracers are listed in Table. 6.4. These tracers show

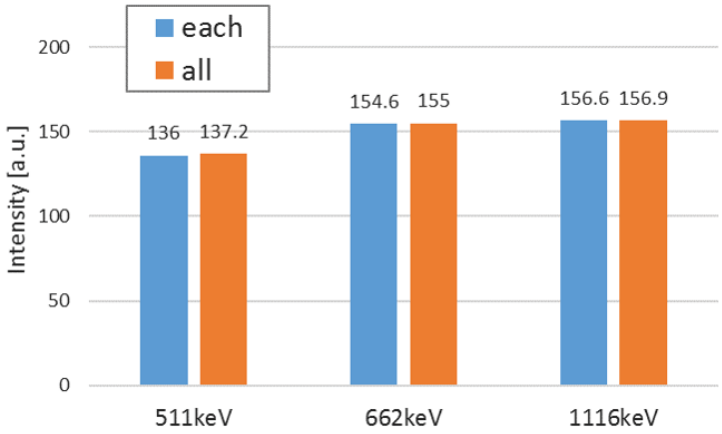

Figure 6.38: Comparing intensity of reconstructed image in multi-color imaging

Table 6.4: Features of radioactive tracers in mouse imaging.

RI tracer	Energy [keV]	Injected intensity [MBq]	Decay time	Accumulation
^{131}I	364	4.0	8 d	thyroid
^{85}Sr	511	1.12	65 d	bone
^{65}Zn	1116	0.93	244 d	liver

in vivo behavior of accumulating in specific positions: dissociated ^{131}I accumulates in the thyroid, ^{85}Sr shows the concentration in the bone, and ^{65}Zn accumulates in the liver [98]. The mouse is treated with inhalation anesthesia and fixed on the rotation stage in the upright position. The imaging region is defined as 80 mm × 80 mm × 80 mm and the medical Compton camera is rotated around the mouse in the plane perpendicular to the body axis of the mouse. The data is taken from 12-angles and the measurement time at each position is 10 min, thus the total integration time here is 2 hours.

Fig. 6.41 shows the result of energy spectrum obtained by 10 minutes measurement from single angle. The three peaks from each tracer of 364 keV, 511 keV, and 1116 keV can be clearly confirmed. Fig. 6.42 $(a)-(c)$ show the results of representative 2-D slices of 3-D image for each tracer and Fig. 6.42 (d) shows the fused image of all three tracers. Furthermore, Fig. 6.43 shows all 2-D slices, each representing 0.8 mm pitch slice in the Z-Y plane. Fig. 6.43 suggests not only 2-dimensional but also 3-dimensional imaging is possible with the medical Compton camera. From the images, it can be confirmed that the tracers are correctly accumulated on each target organ.

For these imaging results, we also evaluate the quantitative performance as is the case in section 6.5.5. In this evaluation, we compare the relative radioactive intensity between

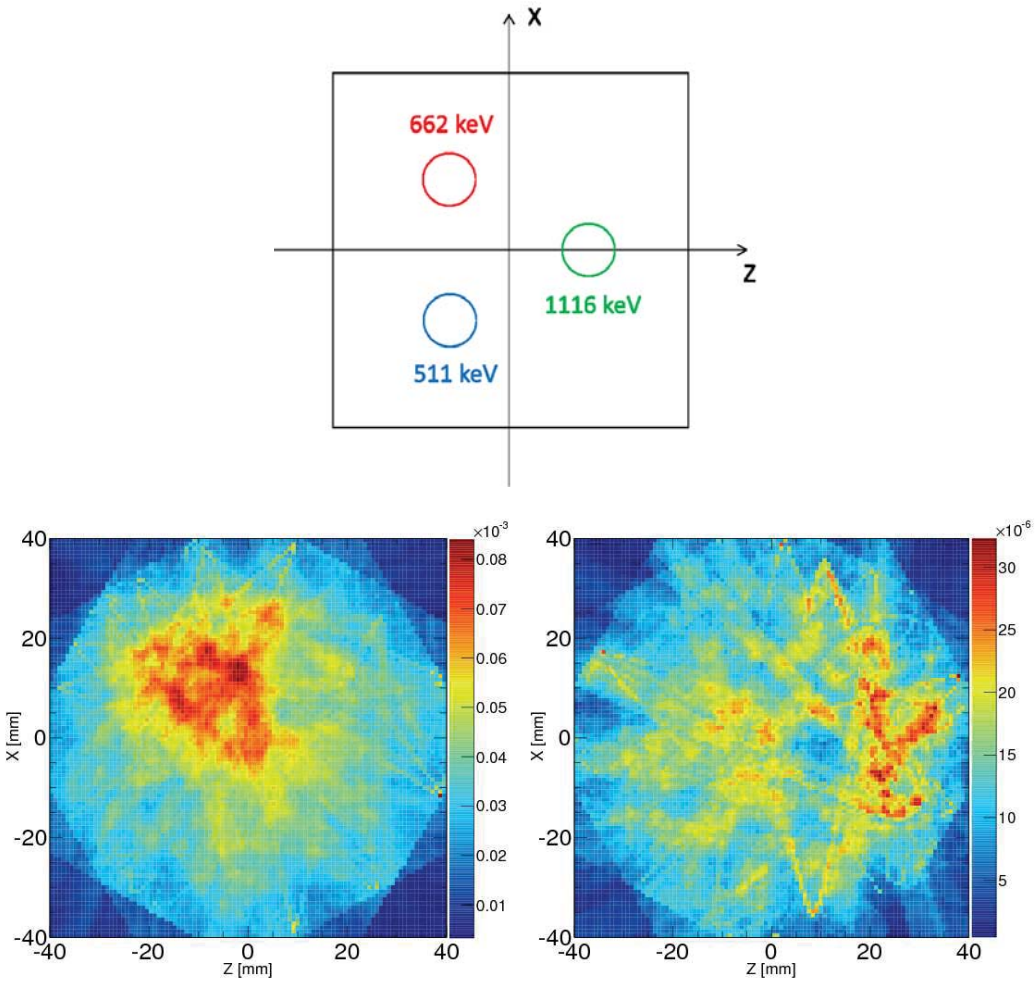

Figure 6.39: Images reconstructed by escape events. ($Left$) image of escape events from 662 keV gamma ray, ($right$) image of escape events from 1116 keV.

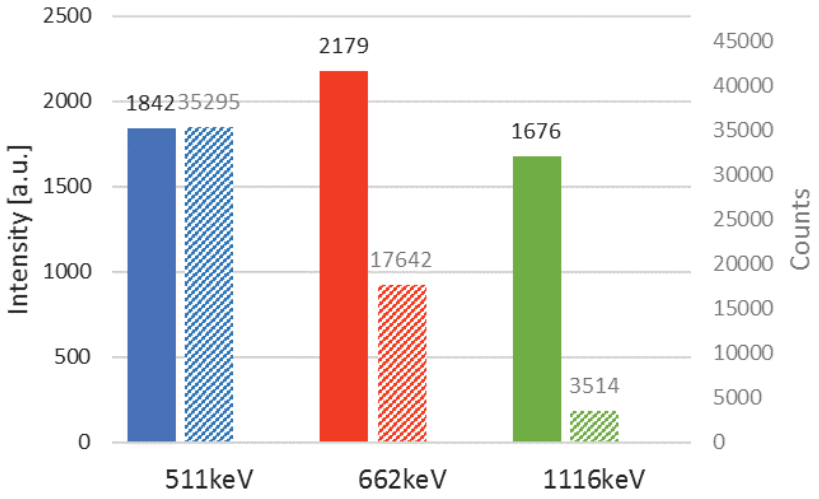

Figure 6.40: Experimental evaluation of the number of event and the intensity of the reconstructed image. The diagonal bars denote the number of event used for reconstruction, and the filled bars denote the intensity of reconstructed image after normalization.

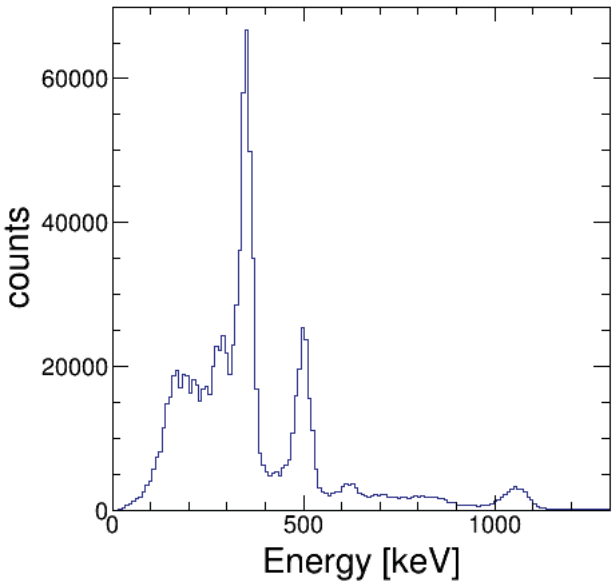

Figure 6.41: Energy spectrum for a mouse imaging.

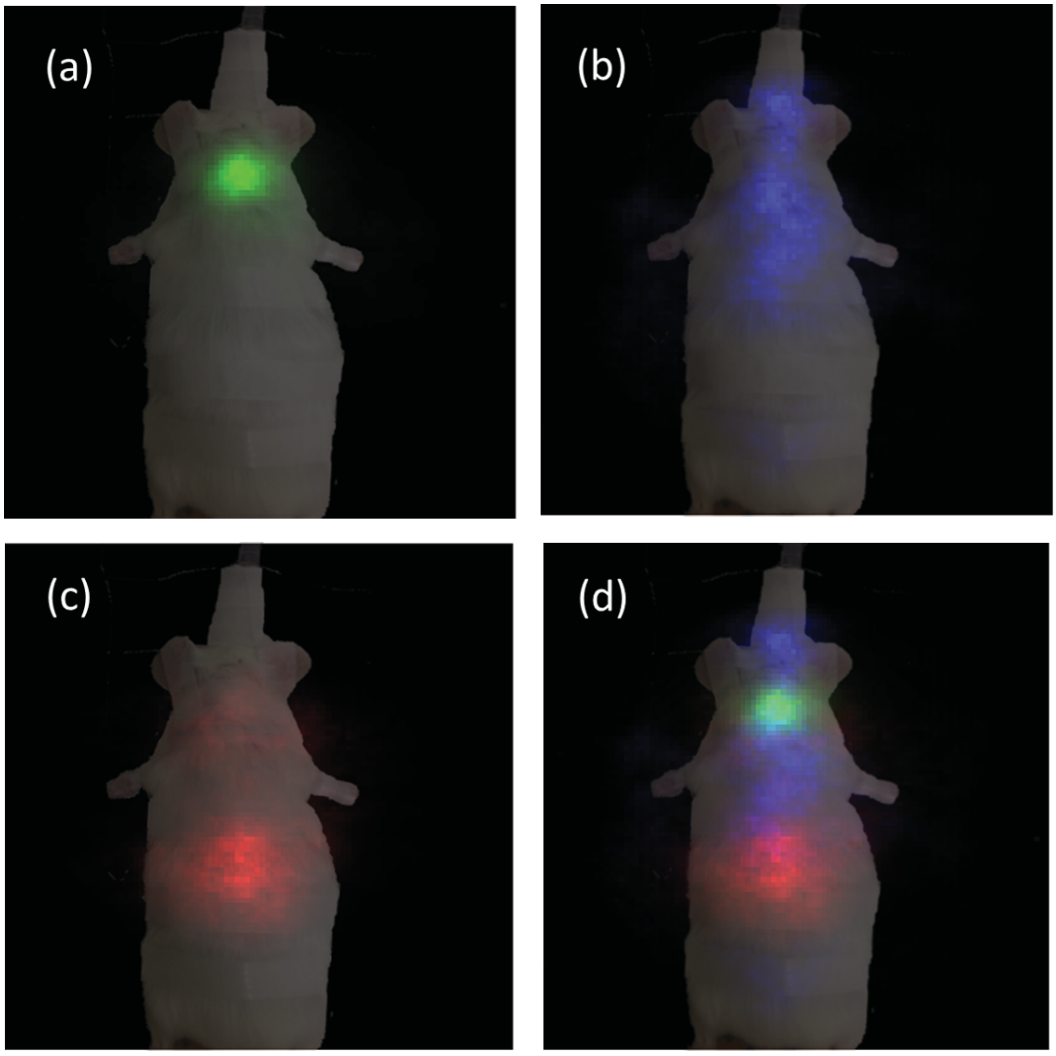

Figure 6.42: Results of 2D slice of mouse imaging. (*a*) image of ^{131}I, (*b*) image of ^{85}Sr, (*c*) image of ^{65}Zn, and (*d*) fused image of all three tracers.

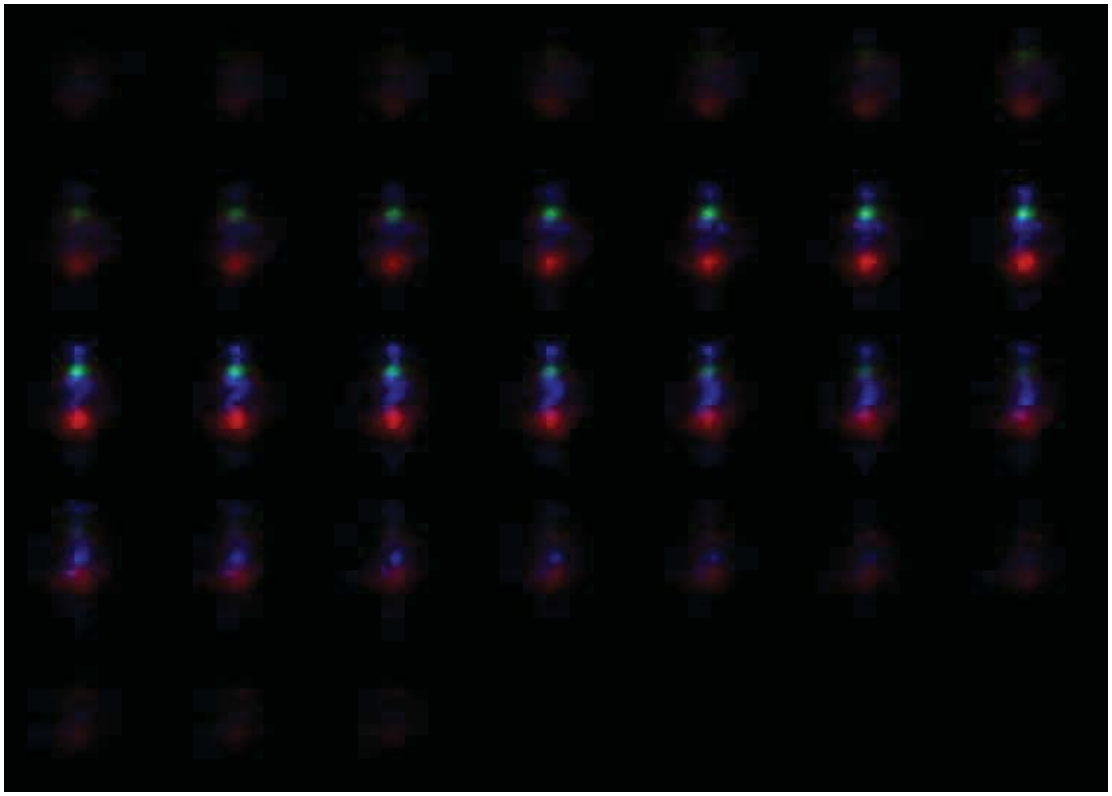

Figure 6.43: 2-D montage of the mouse image. Each figure shows 0.8 mm pitch slice in the Z-Y plane. The green, blue, and red represent image of ^{131}I, ^{85}Sr, and ^{65}Zn, respectively.

Table 6.5: Comparison of the intensity of the radioactive tracers.

RI tracer	Evaluated organ	Weights [g]	Measured intensity [MBq] (ratio [a.u.])	Reconstructed intensity ratio [a.u.]
^{131}I	thyroid	0.062	0.470 (1.000)	1.000
^{65}Zn	liver	1.84	0.141 (0.191)	0.162

the thyroid and the liver because these organs show clear accumulation in the mouse body and we can obtain the accurate RI intensity by harvesting the organs. The thyroid and the liver were harvested 8 hours after the imaging experiment and were investigated the intensity by using Ge detector. The radioactive intensity of the thyroid which is measured by 364 keV peak from ^{131}I is 0.470 MBq and that of the liver which is measured by 1116 keV peak from ^{65}Zn is 0.141 MBq. For the calculation of the reconstructed image intensity, the 3-D ROI (r =7 mm for the thyroid and r =20 mm for the liver) is applied. The intensity of each organ is defined as the integral value over the voxels inside the 3-D ROI, considering the effect of the decay probability and the decay time from the imaging experiment. Table 6.5 shows the measured and reconstructed radioactive intensities both in the case of the thyroid and the liver. The result of relative intensity of the reconstructed image correspond to the real activity with an accuracy of better than 20%. One of the main cause for the difference between the measured and the reconstructed intensity could be the effect of escape events. As described in section 6.5.5, a part of the escape event from ^{85}Sr and ^{65}Zn are included in the energy range for the reconstruction of ^{131}I. Due to this effect, apparent intensity of ^{131}I on the reconstructed image can be increased from the true value, hence the intensity of ^{65}Zn source becomes relatively low in the image. Nevertheless, these results provide the capability of simultaneous imaging of multiple tracers, confirming the feasibility of newly in vivo imaging using the Compton camera.

6.7 Discussion

We obtained promising results for simultaneous multi-color imaging by using the medical Compton camera for newly diagnosis imaging. Toward the practical applications in the field of nuclear medicine, here we discuss the required performance of spatial resolution, measurement time, and quantitativity in various applications.

In section 6.3.3, by optimizing detector design we succeeded in improving the spatial resolution of the medical Compton camera compared to the DOI camera for environmental measurement. However, the spatial resolution of around 3 mm provided by the medical Compton camera is still slightly worse than that of SPECT and PET for animal imaging. In order to obtain better spatial resolution, it is the most effective to improve the

energy resolution of the detector. Based on the simulation estimation, if the energy resolution improves by 2% for 662 keV, the spatial resolution become around 2 mm, which is approximately equal to the resolution of small animal PET.

On the other hand, in terms of the detection efficiency and measurement time, the medical Compton camera showed approximately equivalent performance with SPECT. Although in this study we used and rotated only one Compton camera for multi-angle data acquisition to reduce the detector costs, the detection efficiency can be considerably improved by arranging multiple Compton cameras as a ring shape.

Furthermore, in order to improve the image quality over the image region, this study proposed the multi-angle acquisition method. Note that the compactness of our medical Compton camera enables this multi-angle method and flexible measurements. Indeed, a few other simulation studies have attempted to measure the data from different two or more angles for the image region [99, 100, 101] and showed promising results for improving image quality. However, in the actual measurement situation, there tends to be a problem that large volume of detector and dead-space prevent the configuration especially in small animal imaging. As the future work, in order to conduct more quantitative measurement it is needed to discriminate the escape events.

Chapter 7

Conclusion

In this study, we have developed two types of Compton camera for the purpose of environmental measurement and nuclear medicine applications.

The DOI Compton camera for environmental gamma-ray measurement consists of Ce:GAGG scintillator and MPPC arrays both in the scatterer and the absorber and features high sensitivity even for high energy gamma ray such as 662 keV from ^{137}Cs. By utilizing newly developed DOI identification technique in the scintillator block, the angular resolution was significantly improved compared with that of the non-DOI Compton camera developed in 2013. The results of angular resolution and the intrinsic efficiency for 662 keV were around 8° (FWHM) and 0.43%, respectively. Through imaging tests using point sources, the DOI Compton camera provided the imaging capability of various-energy sources such as ^{22}Na (511 keV), ^{137}Cs (662 keV), and ^{54}Mn (834 keV). Based on these results, we have conducted field tests in Namie, Fukushima with the DOI Compton camera. As a result, we have confirmed that the camera can provide an image of ^{137}Cs hotspots around 10μSv/h within a few minutes data acquisition time, even under high-background contamination of $\sim$5 μSv/h. These images provide important suggestion of gamma-ray distribution, so that the Compton camera facilitates efficient decontamination in the various environments such as resident area and even in the forest. As a future work, by taking advantage of light-weight of the camera we aim to conduct various application such as wide-range aerial imaging by using a drone.

On the other hand, for application of molecular imaging in nuclear medicine, we have also developed the medical Compton camera which features improving the angular and spatial resolutions. One of the key feature of the medical Compton camera was its compactness of $5 \times 6 \times 11\,\mathrm{cm}^3$, which enables flexible measurement in various situations. The typical angular resolution and intrinsic efficiency of the medical Compton camera for 662 keV were 4.2° (FWHM) and 0.06%, respectively. This angular resolution is equal to the spatial resolution of around 3 mm (FWHM) at the center of the defined imaging re-

gion. For the purpose of obtaining 3-D multi-color images, the 3-D image reconstruction method based on MLEM algorithm was also developed. We showed that by applying multi-angle data acquisition method, 3-D isotropic performance over the imaging region can be significantly improved. By using the medical Compton camera, various 3-D imaging tests were conducted. In the imaging of the uniform plane source of ^{137}Cs under the data-acquisition condition of 12-angles, the configuration of the square source was reconstructed 3-dimensionally and the uniformity of the reconstructed image became around 10%. Moreover, for not only single energy source but also multiple energy sources the capability of 3-D visualizing was confirmed through the experiments with unsealed radioactive sources. Finally, as pre-clinical evaluation the first imaging test with a living mouse by the medical Compton camera using multiple tracers was conducted. The three different tracers of ^{131}I (364 keV), ^{85}Sr (514 keV), and ^{65}Zn (1116 keV) were injected into an 8-weeks-old mouse and the data was taken from 12-angles. With the total integration time of 2 hours, we succeeded in imaging that each tracer correctly accumulated on the target organs of thyroid, bone, and liver 3-dimensionally. The result indicates the achievement of 3-D multi-color imaging and the feasibility of newly in vivo imaging by Compton camera.

This study provides the possibility for next-generation radiology imaging, that is, from 2-D black-and-white imaging to 3-D multi-color imaging both in the field of environmental measurement and medical application.

Appendix A

Energy and temperature calibration

In our Compton cameras, energy and temperature dependence of output signals is calibrated by two processes.

The first one is temperature compensating function of MPPCs. Each MPPC array has a temperature sensor, and HVPS adjust the bias voltage depending on the temperature data regularly. By reference the compensation table which is measured in advance by each MPPC array, the temperature dependence of both MPPC gain and amount of light output in scintillator can be calibrated and the output signals become constant regardless of temperature. The temperature dependence is compensated based on linear function as shown in Fig. A.1. Based on the base temperature (T_b) and operation voltage (V_b), the temperature coefficient can be set both in lower (G_1) and higher (G_2) temperature sides. We set the base temperature to 25 °C, and in order to obtain the coefficients the temperature data was measured in 10 °C for lower side and 35 °C for higher side.

In addition to above temperature compensating function, the energy calibration table is also applied to measured raw data. Before starting imaging measurements by our Compton cameras, we firstly created the calibration table which corrects both energy and temperature dependence of the output. Szawlowski et al. [102] shows the non-linearity relationship between the number of exited pixels (N_{fired}) and the number of photons (N_{photon}) as follows:

$$N_{\mathrm{fired}} = N_{\mathrm{total}} \cdot \left[1 - \exp\left(\frac{-\varepsilon N_{\mathrm{photon}}}{N_{\mathrm{total}}}\right)\right] \tag{A.1}$$

where, N_{total} denotes the number of total pixels, and ε denotes the photon detection efficiency. Since the signal output is proportional to the number of fired pixels, the linearity of scintillation photon output also follow this relation. Thus the energy calibration formula

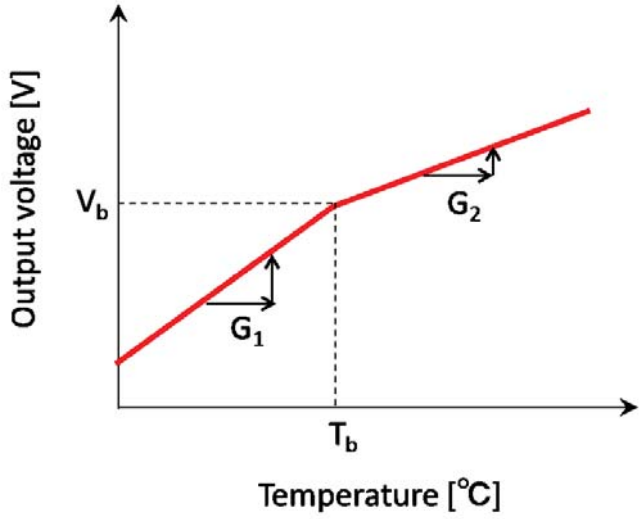

Figure A.1: Temperature coefficient of MPPC arrays. T_b and V_b denote the base temperature and voltage, respectively. The coefficient is obtained both in lower (G_1) and higher (G_2) sides.

is represented by

$$S_{\text{out}} = A_{\text{T}} \cdot \left[1 - \exp\left(-\frac{B_{\text{T}}}{A_{\text{T}}} \cdot E\right)\right], \tag{A.2}$$

where S_{out} and E denote the signal output and energy deposit, respectively. A_{T} and B_{T} are constant parameters, which also takes account a temperature dependence of scintillator light output. We measured output response for several energy gamma-ray sources under representative temperature, and obtained parameters A_{T} and B_{T} by interpolating the data according to equation (A.2) for each temperature.

For the energy calibration of the scatterer, we used ^{241}Am (60 keV), ^{133}Ba (364 keV) and ^{137}Cs (662 keV) because the dominating energy deposit in the scatterer becomes relatively low such as under $\simeq$200 keV. On the other hand, the energy deposit in the absorber tends to become larger than that in the scatterer, so that the energy calibration of the absorber was conducted using ^{22}Na (511 keV) and ^{137}Cs (662 keV). After creating the segmentation map (described in Appendix B), the peak channel values of each scintillator pixel for above energy were measured under three representative temperature of 10 °C, 25 °C, and 35 °C.

Appendix B

Position calibration

In order to obtain the position information where the incident gamma rays scatter or absorb in the scintillator array, the position map should be obtained in advance and the hit pixel is determined by referring to the map.

The position map is made based on the response for uniform irradiation of 662 keV gamma rays. For example, Fig. B.1 shows the representative 2-D position response of 11×11 scintillator which is obtained by applying the centroid method described in equation (4.2)−(4.3). At first, the peak position of each scintillator pixel is identified as shown in the red plots in Fig. B.1. Then the positional segmentation of each scintillator is defined as the white line which connects the midpoints of neighboring peaks.

As is the case with these 2-D scintillator array, for the 3-D scintillator array, the 2-D segmentation map is firstly defined for the 2-D projections of the responses in all layers. The segmentation in the depth direction is then conducted by each 2-D pixel (by each 11×11 element in the case of Fig. B.1) in order to minimize the effect of gain variations of the MPPC pixels.

Because the position map does not depend on the parameters of energy deposit and temperature, we utilize the map which is made based on the data of ^{137}Cs source to all experimental measurements.

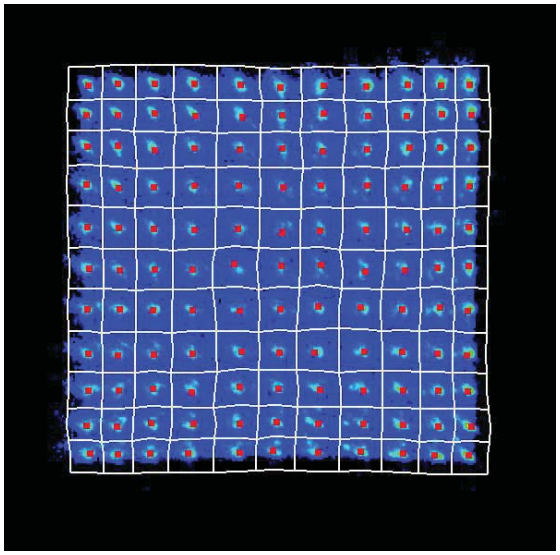

Figure B.1: Representative 2-D position map. The red plots and the white lines denote the peak position of each scintillator pixel and defined position map, respectively.

Bibliography

[1] V. Schönfelder, et al., *IEEE Trans. Nucl. Sci.*, vol. NS-31, pp. 766-770, 1984.

[2] V. Schönfelder, et al., *ApJS*, vol. 86, p.657-692, 1993.

[3] V. Schönfelder, et al., *Astron. Astrophys. Suppl. Ser.*, vol. 120, pp. 13-21, 1996.

[4] V. Schönfelder, *New Astronomy Reviews*, vol. 48, pp. 193-198, 2004.

[5] A. F. Iyudin, et al., *Astron. Astrophys.*, vol. 284, L1-L4, 1994.

[6] M. S. Bandstra, et al., *Astrophys. J.*, vol. 738, pp. 8-16, 2011.

[7] Nuclear and Industrial Safety Agency, 6.6.2011.
(http://www.meti.go.jp/earthquake/nuclear/pdf/20110606-1nisa.pdf)

[8] M. Miyazaki and R. Hayano, *physics.med-ph*, arXiv:1608.05185v1, 2016.

[9] F. Beekman, F. Have, *Eur. J. Med. Mol. Imaging*, vol. 34, pp. 151-161, 2007.

[10] S. Yamamoto, et al., *Nucl. Inst. and Meth. A*, vol. 743, pp. 124-129, 2014.

[11] M. C. Goorden, F. Beekman, *Phys. Med. Biol.*, vol. 55, pp. 1265-1277, 2010.

[12] S. V. Guru, et al., *Nucl. Inst. and Meth. A*, vol. 353, pp. 328-333, 1994.

[13] S. Yamamoto, et al., *Nucl. Inst. and Meth. A*, vol. 622, pp. 261-269, 2010.

[14] O. Gal, et al., *Nucl. Inst. and Meth. A*, vol. 460, pp. 138-145, 2001.

[15] K. Okada, et al., *Progress in Nuclear Science and Technology*, Vol. 4, pp. 14-17, 2014.

[16] Y. Ueno, et al., *Nucl. Inst. and Meth. A*, vol. 822, pp. 48-56, 2016.

[17] W. Kaya, et al., *IEEE NSS/MIC Conference Record*, pp. 3821-3824, 2010.

[18] C. Wahl, et al., *IEEE NSS/MIC Conference Record*, pp. 1-4, 2014.

[19] C. Wahl, et al., *Nucl. Inst. and Meth. A*, vol. 784, pp. 377-381, 2015.

[20] Z. He, *Nucl. Inst. and Meth. A*, vol. 463, pp. 250-267, 2001.

[21] K. Vetter, *Nucl. Inst. and Meth. A*, vol. 805, pp. 127-134, 2016.

[22] PHDS Gamma-ray Imaging Detectors.
(http://www.phdsco.com/products/gegi/specs)

[23] T. Takahashi, et al., *New Century of X-ray Astronomy, ASP*, vol. 251, pp. 210-213, 2002.

[24] T. Takahashi, et al., *IEEE NSS/MIC Conference Record*, pp. 4199-4204, 2012.

[25] S. Takeda, et al., *Physics Procedia*, vol. 37, pp. 859-866, 2012.

[26] S. Watanabe, et al., *Nucl. Inst. and Meth. A*, vol. 765, pp. 192-201, 2014.

[27] S. Takeda, et al., *Nucl. Inst. and Meth. A*, vol. 787, pp. 207-211, 2015.

[28] J. Jiang, et al., *J. Nucl. Sci. Technol.*, vol. 53, 7, pp. 1067-1075, 2016.

[29] M. Kagaya, et al., *Nucl. Inst. and Meth. A*, vol. 804, pp. 25-32, 2015.

[30] D. E. Kuhl and R. Q. Edwards, *Radiologh*, vol. 80, pp. 653-662, 1963.

[31] M. A. Flower, et al., *Phys. Med. Biol*, vol. 26, pp. 671-691, 1981.

[32] R. Chesser and H. Gemmell, *Phys. Med. Biol.*, vol. 27, pp. 437-441, 1982.

[33] E. Tanaka, et al., *Phys. Med. Biol.*, vol. 29, pp. 1489-1500, 1984.

[34] A. Rahmim and H. Zaidi, *Nuclear Medicine Communications*, vol. 29, pp. 193-207, 2008.

[35] Brownell G. L. and W. H. Sweet, *Nucleonics*, 11, pp. 40-45, 1953.

[36] T. F. Budinger, *J. Nucl. Med.*, vol. 24, pp. 73-78, 1983.

[37] M. M. Khalil, et al., *IJMI*, vol. 2011, 796025, 2011.

[38] S. Motomur, et al., *J. Anal. At. Spectrom.*, vol. 28, pp. 934-939, 2013.

[39] R. W. Todd, et al., *Nature*, vol. 251, pp. 132-134, 1974.

[40] M. Singh, *Medical Physics*, vol. 10, 4, pp. 421-427, 1983.

[41] M. Singh and D. Doria, *Medical Physics*, vol. 10, 4, pp. 428-435, 1983.

[42] H. Seo, et al., *IEEE TNS*, vol. 57, 3, pp. 1420-1425, 2010.

[43] W. Lee and T. Lee, *Nucl. Inst. and Meth. A*, vol. 624, 1, pp. 118-124, 2010.

[44] M. A. Alnaaimi, et al., *Phys. Med. Biol.*, vol. 56, pp. 3473-3486, 2011.

[45] N. Dedek, et al., *IEEE TNS*, vol. 55, pp. 2689-2697, 2008.

[46] S. Motomura, et al., *IEEE TNS*, vol. 54, pp.710-717, 2007.

[47] S. Motomura, et al., *J. Anal. At. Spectrom.*, vol. 23, pp. 1089-1092, 2008.

[48] M. Munekane, et al., *Biochemistry and Biophysics Reports*, vol. 5, pp. 211-215, 2016.

[49] S. Takeda, et al., *IEEE TNS*, vol. 56, 3, pp. 783-790, 2009.

[50] S. Takeda, et al., *IEEE TNS*, vol. 59, 1, pp. 70-76, 2012.

[51] T. Tanimori, et al., *New Astron. Rev.*, vol. 48, pp. 263-268, 2004.

[52] S. Kabuki, et al., *Nucl. Inst. and Meth. A*, vol. 580, pp. 1031-1035, 2007.

[53] A. Takeda, et al., *Nucl. Inst. and Meth. A*, vol. 546, pp. 258-262, 2005.

[54] R. Orito, et al., *Nucl. Inst. and Meth. A*, vol. 513, pp. 408-412, 2003.

[55] S. Kurosawa, Ph. D. Thesis, Kyoto Univ., 2011.

[56] S. Kabuki, et al., *IEEE NSS/MIC Conference Record*, pp. 2971-2975, 2009.

[57] S. Kabuki, et al., *Nucl. Inst. and Meth. A*, vol. 623, pp. 606-607, 2010.

[58] R. D. Evans, "The Atomic Nucleus," 1955.

[59] A. Zoglauer, G. Kanbach, *Proceedings of the SPIE*, vol. 4851, pp. 1302-1309, 2003.

[60] R. Ribberfors, *Phys. Rev.* B 12, pp. 2067-2074, 1975.

[61] D. Bursa et al., *Nucl. Inst. and Meth. A*, vol. 379, pp. 167-175, 1996.

[62] B. Smith, *J. Opt. Soc. Am. A*, vol. 22, pp. 445-459, 2005.

[63] S. Wilderman et al., *IEEE Nucl. Sci. Sympo.*, vol. 3, pp.1716-1720, 1998.

[64] A. Zoglauer, Ph.D Thesis, "First Light for the Next Generation of Compton and Pair Telescopes," Technische Universität München, 2005.

[65] K. Kamada, et al., *Cryst. Growth Des.*, vol. 11, pp. 4484-4490, 2011.

[66] K. Kamada, et al., *J. Cryst. Growth*, vol. 352, pp. 88-90, 2012.

[67] A. Yoshikawa, et al., *J. Cryst. Growth*, vol. 35, pp. 1882-1886, 2013.

[68] P. Prusa, et al., *Radiation Measurements*, vol. 56, pp. 62-65, 2013.

[69] M. Yokoyama, et al., *arXiv:physics*/0605241, 2006.

[70] S. Gomi, et al., *Nucl. Inst. and Meth. A*, vol. 581, pp. 427-432, 2007.

[71] S. Yamamoto, et al., *IEEE NSS/MIC Conference Record*, pp. 1094-1097, 2006.

[72] J. Kataoka, et al., *Nucl. Inst. and Meth. A*, vol. 732, pp. 403-407, 2013.

[73] H. Suzuki, et al., *IEEE NSS/MIC Conference Record*, 6829610, 2013.

[74] T. Nishiyama, et al., *IEEE NSS/MIC Conference Record*, 6829417, 2013.

[75] J. S. Karp, M. E. Daube-Witherspoon, *Nucl. Inst. and Meth. A*, vol. 260, pp. 509-517, 1987.

[76] J. H. Jung, et al., *Nucl. Inst. and Meth. A*, vol. 571, pp. 669-675, 2007.

[77] S. Yamamoto, et al., *Nucl. Inst. and Meth. A*, vol. 587, pp. 319-323, 2008.

[78] K. Shimizu, et al., *IEEE Trans. Nucl. Sci.*, vol. 35, pp. 717-720, 1988.

[79] W. W. Moses, et al., *IEEE Trans. Nucl. Sci*, vol. 42, pp. 1085-1089, 1995.

[80] Y. Shao, et al., *IEEE Trans. Nucl. Sci*, vol. 47, pp. 1051-1057, 2000.

[81] F. Taghibakhsh, et al., *Nucl. Inst. and Meth. A*, vol. 633, pp. S250-S254, 2011.

[82] T. Tsuda, et al., *IEEE Trans. Nucl. Sci*, vol. 51, pp. 2537, 2004.

[83] N. Inadama, et al., *IEEE Trans. Nucl. Sci.*, vol. 53, pp. 2523, 2006.

[84] Y. Yazaki, et al., *IEEE NSS/MIC Conference Record*, pp. 3822-3826, 2009.

[85] T. Yamaya, et al., *Phys. Med. Biol.*, vol. 56, pp. 6793-6807, 2011.

[86] Y. Yazaki, et al., *IEEE Trans. Nucl. Sci*, vol. 59, pp. 462, 2012.

[87] A. Kishimoto, et al., *IEEE Trans. Nucl. Sci*, vol. 60, pp. 38-43, 2013.

[88] K. Takeuchi, et al., *Nucl. Inst. and Meth. A*, vol. 765, pp. 187-191, 2014.

[89] S. Agostinelli, et al., *Nucl. Inst. and Meth. A*, vol. 506, pp. 250-303, 2003.

[90] A. Kishimoto, et al., *JINST*, vol. 9, P11025, 2014.

[91] T. Hebert, et al., *J. Opt. Soc. Am. A*, vol. 7, pp. 1305-1313, 1990.

[92] X. Lojacono, et al., *IEEE Trans. Nucl. Sci.*, vol. 60, pp. 3355-3363, 2013.

[93] S. R. Tornga, et al., *IEEE Trans. Nucl. Sci.*, vol. 56, pp. 1372-1376, 2009.

[94] S. M. Kim, et al., *Phys. Med. Biol.*, vol. 55, pp. 5007-5027, 2010.

[95] M. W. Rawool-Sullivan, et al., *Appl. Radiat. Isot.*, vol. 66, pp. 1986-1991, 2008.

[96] B. Seitz, et al, *IEEE Trans. Nucl. Sci.*, vol. 63, pp. 503-508, 2016.

[97] T. Yanagida, et al., *Jpn. J. Appl. Phys.*, vol. 52, 2013.

[98] S. Enomote, *Biomed. Res. Trace Elem.*, vol. 16, pp. 233-240, 2005.

[99] M. Yamaguchi, et al., *IEEE NSS/MIC Conference Record*, pp. 4000-4002, 2008.

[100] S. Takeda, et al., *IEEE Sensors Applications Symposium*, 11207672, 2010.

[101] Y. Calderon, et al., *JINST*, vol. 9, C06003, 2014.

[102] M. Sxawlowski, et al., *IEEE NSS/MIC Conference Record*, pp. 4591-4596, 2007.

Acknowledgements

I deeply appreciate to Professor Jun Kataoka for all his guidance and encouragements throughout my graduate school life. This thesis would not have been completed without his continuous support.

I would like to thank very much S. Ohsuka, S. Nakamura, M. Hirayanagi, and S. Adachi from Hamamatsu Photonics K. K. for contribution of Compton camera fabrication. They helped me many times when the electronics of the Compton camera had troubles. For the small animal imaging experiments, I really appreciate the great effort by Dr. K. Matsunaga, Dr. H. Ikeda, Dr. E. Shimosegawa, and Dr. J. Hatazawa from Osaka University. My gratitude is also for Dr. N. Kawachi, Dr. M. Yamaguchi, Y. Nagao, and Dr. K. Kurita from National Institutes for Quantum and Radiological Science and Technology, who kindly supported the imaging experiments of the plane source and gave me a lot of technical advice. I also thank N. Suzui, Y. G. Yin, and S. Ishii for the preparation of the plane source imaging experiments. I appreciate to Prof. H. Okochi and Dr. H. Ogata for giving me the opportunity to conduct the field tests in Namie, Fukushima. I would like to also thank all the laboratory members in Waseda University, especially T. Nishiyama, T. Taya, and Y. Iwamoto, for their support and fruitful discussions. I am also grateful to Prof. T. Nishio from Tokyo Women's medical University, Dr. S. Kabuki from Tokai University School of Medicine, and Prof. K. Yorita for their many helpful advises to accomplish this study. This work was supported by Japan Society for the Promotion Science (JSPS).

Finally, I express special thanks to my family for their understanding, encouragements, and continuous supports for my meaningful academic life.

研究業績

種 類 別	題名、　発表・発行掲載誌名、　発表・発行年月、　連名者（申請者含む）
学術雑誌 （査読あり）	【主著】 ○[1] A. Kishimoto, J. Kataoka, A. Koide, K. Sueoka, Y. Iwamoto, T. Taya, S. Ohsuka, "Development of a compact scintillator-based high-resolution Compton camera for molecular imaging," *NIM-A*, in press, 2016. ○[2] A. Kishimoto, J. Kataoka, T. Nishiyama, T. Taya, S. Kabuki, "Demonstration of three-dimensional imaging based on handheld Compton camera," *JINST*, 10, P11001, 2015. ○[3] A. Kishimoto, J. Kataoka, T. Nishiyama, T. Fujita, K. Takeuchi, H. Okochi, H. Ogata, H. Kuroshima, S. Ohsuka, S. Nakamura, M. Hirayanagi, S. Adachi, T. Uchiyama, H. Suzuki, "Performance and field tests of a handheld Compton camera using 3-D position-sensitive scintillators coupled to multi-pixel photon counter arrays," *JINST*, 9, P11025, 2014. ○[4] A. Kishimoto, J. Kataoka, T. Kato, T. Miura, T. Nakamori, K. Kamada, S. Nakamura, K. Sato, Y. Ishikawa, K. Yamamura, N. Kawabata, S. Yamamoto, "Development of Dual-Sided Readout DOI-PET Module Using Large-Area Monolithic MPPC-Arrays", *IEEE-TNS*, vol.60, pp.38-43, 2013. 【共著】 [5] T. Taya, J. Kataoka, A. Kishimoto, Y. Iwamoto, A. Koide, T. Nishio, S. Kabuki, T. Inaniwa, "First demonstration of real-time gamma imaging by using a handheld Compton camera for particle therapy," *NIM-A*, in press, 2016. [6] Y. Iwamoto, J. Kataoka, A. Kishimoto, T. Nishiyama, T. Taya, H. Okochi, H. Ogata, S. Yamamoto, "Novel methods for estimating 3D distributions of radioactive isotopes in materials," *NIM-A*, in press, 2016. [7] M. Takabe, A. Kishimoto, J. Kataoka, S. Sakuragi, Y. Yamazaki, "Performance evaluation of newly developed SrI_2(Eu) scintillator," *NIM-A*, in press, 2016. [8] J. Kataoka, A. Kishimoto, T. Fujita, T. Nishiyama, Y. Kurei, T. Tsujikawa, T. Oshima, T. Taya, Y. Iwamoto, H. Ogata, H. Okochi, S. Ohsuka, H. Ikeda, S. Yamamoto, "Recent progress of MPPC-based scintillation detectors in high precision X-ray and gamma-ray imaging," *NIM-A*, vol.784, pp.248-254, 2015. [9] K. Takeuchi, J. Kataoka, T. Nishiyama, T. Fujita, A. Kishimoto, S. Ohsuka, S. Nakamura, S. Adachi, M. Hirayanagi, T. Uchiyama, Y. Ishikawa, T. Kato, "Stereo Compton cameras for the 3-D localization of radioisotopes," *NIM-A*, vol.765, pp.187-191, 2014.

研究業績

種 類 別	題名、　発表・発行掲載誌名、　発表・発行年月、　連名者（申請者含む）
講演 （国際会議）	[10] T. Nishiyama, J. Kataoka, A. Kishimoto, T. Fujita, Y. Iwamoto, T. Taya, S. Ohsuka, S. Nakamura, M. Hirayanagi, N. Sakurai, “A novel Compton camera design featuring a rear-panel shield for substantial noise reduction in gamma-ray images,” *JINST*, 9, C12031, 2014. [11] T. Fujita, J. Kataoka, A. Kishimoto, Y. Kurei, T. Nishiyama, T. Oshima, T. Taya, “Development of prototype PET scanner using dual-sided readout DOI-PET modules,” *JINST*, 9, P12015, 2014. [12] J. Kataoka, A. Kishimoto, T. Nishiyama, T. Fujita, K. Takeuchi, K. Kato, T. Nakamori, S. Ohsuka, S. Nakamura, M. Hirayanagi, S. Adachi, T. Uchiyama, K. Yamamoto, “Handy Compton camera using 3D position-sensitive scintillators coupled with large-area monolithic MPPC arrays,” *NIM-A*, vol.732, pp.403-407, 2013. 【筆頭のみ】 [1] A. Kishimoto, J. Kataoka, L. Tagawa, S. Mochizuki, T. Taya, Y. Iwamoto, S. Ohsuka, K. Matsunaga, H. Ikeda, E. Shimosegawa, J. Hatazawa, N. Kawachi, Y. Nagao, M. Yamaguchi, K. Kurita, “Demonstration of Multi-Color 3D imaging of Gamma Rays Based on Ultra-Compact Compton Camera,” IEEE Nuclear Science Symposium and Medical Imaging Conference, Strasburg, 2016. [2] A. Kishimoto, J. Kataoka, K. Sueoka, A. Koide, T. Taya, S. Ohsuka, “Development of a compact scintillator-based high-resolution Compton camera for molecular imaging,” Vienna Conference on Instrumentation 2016, Austria, 2016. [3] A. Kishimoto, J. Kataoka, T. Nishiyama, T. Taya, S. Kabuki, “Study of Three-Dimensional Imaging with Scintillator-Based Handheld Compton Camera for Molecular Imaging,” 17th International Workshop on Radiation Imaging Detectors, Germany, 2015. [4] A. Kishimoto, J. Kataoka, T. Nishiyama, T. Fujita, K. Takeuchi, H. Okochi, H. Ogata, H. Kuroshima, S. Ohsuka, S. Nakamura, M. Hirayanagi, S. Adachi, T. Uchiyama, H. Suzuki, “Performanve and field tests of handy Compton camera using 3D position-sensitive scintillators coupled with MPPC-arrays,” SORMA XV, Michigan University, USA, 2014. [5] A. Kishimoto, J. Kataoka, T. Kato, T. Miura, T. Nakamori, K. Kamada, S. Nakamura, K. Sato, Y. Ishikawa, K. Yamamura, S. Yamamoto, “Development of a MPPC-based DOI-PET module with submillimeter 3-D resolution”, IEEE Nuclear Science Symposium and Medical Imaging Conference, California, USA, 2012.

研究業績

種 類 別	題名、　発表・発行掲載誌名、　発表・発行年月、　連名者（申請者含む）
講演 （国内学会）	【筆頭のみ】 [1] 岸本彩, 片岡淳, 末岡晃紀, 小出絢子, 岩本康弘, 大須賀慎二,「分子イメージング応用に向けた高解像度型コンプトンカメラの開発」, 応用物理学会, 東京工業大学, 2016. [2] 岸本彩, 片岡淳, 西山徹, 藤田卓也, 多屋隆紀, 株木重人, 西尾禎治,「携帯型コンプトンカメラによる 3 次元ガンマイメージ再構成」, 応用物理学会, 東海大学, 2015. [3] 岸本彩, 片岡淳, 高部美帆, 櫻木史郎, 山嵜康司,「PMT, APD, MPPC を用いた SrI_2(Eu)シンチレータの限界性能評価」, 応用物理学会, 東海大学, 2015. [4] 岸本彩, 片岡淳, 西山徹, 藤田卓也, 岩本康弘, 多屋隆紀, 大河内博, 緒方裕子, 大須賀慎二, 中村重幸, 足立俊介, 内山徹也, 「3 次元シンチレータを用いた高感度コンプトンカメラの開発(Ⅲ)」, 応用物理学会, 北海道大学, 2014. [5] 岸本彩, 片岡淳, 加藤卓也, 中森健之, 西山徹, 武内健士郎, 藤田卓也, 鎌田圭, 中村重幸, 里健一, 石川嘉隆, 山村和久, 山本誠一, 「大面積・薄型モノリシック MPPC アレイを用いた 3 次元高解像度ガンマ線位置検出手法の開発」, 応用物理学会, 愛媛大学, 2012. [6] 岸本彩, 片岡淳, 三浦大陽, 中森健之, 鎌田圭, 中村重幸, 里健一, 石川嘉隆, 山村和久, 山本誠一, 「大面積モノリシック MPPC アレイを用いた新規 DOI 測定手法の開発」, 応用物理学会, 早稲田大学, 2012. [7] 岸本彩, 錦戸文彦, 稲玉直子, 吉田英治, 盛武敬, 片岡淳, 村山秀雄, 山谷泰賀, 「IVR 用被曝線量分布モニタリングシステムの基礎研究」, 日本医学物理学会, Web 開催, 2011.
受賞歴	[1] 第 59 回応用物理学会講演奨励賞, 2012. [2] 第 26 回先端技術大賞 特別賞, 2012.